Baryon Spectroscopy With FLIC Fermions

James Zanotti

Supervisors: Derek Leinweber and Anthony Williams

Special Research Centre for the Subatomic Structure of Matter
and
Department of Physics and Mathematical Physics,
Adelaide University,
Australia

October 2002

Abstract

Hadron masses are calculated in quenched lattice QCD in order to probe the scaling behavior of a novel fat-link clover fermion action in which only the irrelevant operators of the fermion action are constructed using APE-smeared links. The scaling analysis indicates FLIC fermions provide a new form of nonperturbative $\mathcal{O}(a)$ improvement where near-continuum results are obtained at finite lattice spacing. Light quark masses corresponding to an m_π/m_ρ ratio of 0.35 are considered to assess the exceptional configuration problem of clover-fermion actions. Simulations at such light quark masses reveal evidence of chiral nonanalytic behaviour in the Δ mass.

Masses of positive and negative parity excited nucleons and hyperons are calculated in quenched lattice QCD, where the nature of the Roper resonance and $\Lambda(1405)$ is of particular interest. The results are in agreement with earlier N^* simulations with improved actions, and exhibit a clear mass splitting between the nucleon and its parity partner, as well as a small mass splitting between the two low-lying $J^P = \frac{1}{2}^-$ N^* states. Study of different Λ interpolating fields suggests a similar splitting between the lowest two $\frac{1}{2}^-$ Λ^* states, although the empirical mass suppression of the $\Lambda^*(1405)$ is not seen.

Results for masses of spin-$\frac{3}{2}$ baryons using the FLIC fermion action are presented. Spin-3/2 interpolating fields providing overlap with both spin-$\frac{3}{2}$ and spin-$\frac{1}{2}$ states are considered. In the isospin-$\frac{1}{2}$ sector, we observe, after appropriate spin and parity projection, a strong signal for the $J^P = \frac{3}{2}^-$ state together with a weak but discernible signal for the $\frac{3}{2}^+$ state with a mass splitting near that observed experimentally. We also find good agreement between the $\frac{1}{2}^\pm$ masses and earlier nucleon mass simulations with the standard spin-$\frac{1}{2}$ interpolating field. For the isospin-$\frac{3}{2}$ Δ states, clear mass splittings are observed between the various $\frac{1}{2}^\pm$ and $\frac{3}{2}^\pm$ channels, with the calculated level orderings in good agreement with those observed empirically.

This thesis also contains a systematic investigation of Symanzik improvement in the gauge field action for the static quark potential in quenched QCD. We consider Symanzik improved gauge field configurations on a $16^3 \times 32$ lattice with a relatively coarse lattice spacing of 0.165(2) fm. A matched set of Standard Wilson gauge configurations is prepared at $\beta = 5.74$ with the same physical volume and lattice spacing and is studied for comparison. We find that, despite the coarse lattice spacing, the unimproved and less-expensive Wilson action does as well as the Symanzik action in allowing us to extract the static quark potential at large $q\bar{q}$ separations. We have considered novel methods for stepping off-axis

in the static quark potential which provides new insights into the extent to which the ground state potential dominates the Wilson loop correlation function.

A continuation of the work done with the static quark potential on improved gauge fields has lead to a comprehensive analysis of the behaviour of the lattice spacing as a function of β. The results are extremelly well described by the standard two-loop scaling function of $SU(3)$ gauge theory. This study now provides a useful tool for predicting the value of β to be used in a simulation in order to achieve the required lattice spacing.

Statement of Originality

This work contains no material which has been accepted for the award of any other degree or diploma in any university or other tertiary institution and, to the best of my knowledge and belief, contains no material previously published or written by another person, except where due reference has been made in the text.

I give consent to this copy of my thesis, when deposited in the University Library, being available for loan and photocopying.

27/3/2003

Acknowledgement

Last Drinks. The long pub crawl, also known as my education, has come to an end. Twenty-one years – 130 pages. I have been lucky to have had the opportunity to do such interesting work and now I'd like to return my thanks to those who have helped me get here.

Firstly my supervisors, Derek and Tony, who have mentored and guided me from a fledgling student into a fledgling postdoc. I acknowledge your patience, support and direction in this three and half year journey.

I also thank Tony Thomas and the CSSM for providing excellent research facilities. I am also extremelly grateful to the Australian National Computing Facility for Lattice Gauge Theory for the use of the Orion supercomputer on which the bulk of the calculations in this thesis were performed.

I have many collaborators to acknowledge. Wally Melnitchouk for his contribution to the study of excited baryons and for his superhuman speed in creating those lovely plots; Ross Young for providing chiral extrapolations of my data; Sundance Bilson-Thompson, Frederic Bonnet, Patrick Bowman, John Hedditch, Frank Lee and Jianbo Zhang for code-sharing; Ben Lasscock for helping with the calculation of lattice spacings; Crazy Frenchman and Stewart Wright for giving me grief around the office; and Will Detmold for assistance with everything imaginable - dork!.

Sharon and Sara also get a mention for their ability of keeping a group of 30 physicists organised. Also thanks to Ramona for keeping the computers in shape.

That about sums up the Uni side of things. However, I do have a life outside Uni and it is these people who have kept me sane (not to mention fed) over the past few years. In particular, I give a special thanks to my family, Mum, Dad, Big Stick and Little Sister Jo.

I am also lucky to have great bunch of friends. In particular, though I am grateful to my special friends Becc and Jason - for not only keeping me company while drinking beer, but for sharing the pain of thesis writing - we made it.

Finally we come to Cara - what a gal! Thank you for everything.

Contents

1

Introduction

Quantum Chromodynamics (QCD) has long been considered as the fundamental theory of the strong interaction which binds protons and neutrons together. The theory of QCD is formulated in terms of *quarks* and *gluons* and describes their interactions. Due to the self-interacting nature of gluons, it is impossible to calculate analytically the nonperturbative (or low-energy) properties of QCD such as hadron masses from first principles. The only way to perform such an *ab initio* calculation is via a numerical simulation on a discretised lattice with finite lattice spacing, a.

Lattice gauge theory is now the universally accepted method for rigorously testing the nonperturbative properties of QCD. A large amount of computing resources are being invested world-wide for this task. For example, the QCDOC supercomputer at Brookhaven National Laboratory is being designed specifically for lattice QCD calculations and is expected to reach speeds of up to 10 TFLOPS (10^{12} floating point operations per second). The impressive progress that has been made in computer hardware over the last few years has been complimented by the development of more efficient QCD algorithms, bringing realistic simulations of hadronic observables with sufficiently large volumes, small (near physical) quark masses and fine enough lattices within reach.

In order to formulate Lattice QCD, one needs to construct a discretised version of the continuum QCD action in terms of the lattice spacing, a. These discretisations, by their nature, will have errors of the order of the lattice spacing. The majority of the work contained in this thesis is performed using a novel improvement scheme which removes $\mathcal{O}(a)$ errors from the fermion part of the QCD action. This action simultaneously allows efficient access to the light quark mass regime where many previous improvement schemes have failed.

An introduction to the Standard Model and QCD is detailed in Chapter 2. Here we gain an idea about what the Standard Model can tell us about the nature of the subatomic world. As most of the work presented in this thesis is aimed towards calculating baryon masses on the lattice, the simple quark model of hadron structure is also introduced in Chapter 2. Despite its simplicity, the naive quark model provides a useful tool for understanding the ordering in the observed baryon mass spectrum.

Chapter 3 is devoted to introducing Lattice Gauge Theory. In particular, we look at the construction of a discretised version of the QCD action and the manner in which a calculation of observable quantities, such as a hadron mass, proceeds.

A study of Symanzik improvement in the static quark potential is performed in Chapter 4. By considering novel paths for the calculation of the off-axis potential, we are able to gain information on the extent to which the ground state potential dominates the Wilson loop correlation function. An extension of this work in Chapter 5 provides the first comprehensive analysis of the behaviour of the lattice spacing as a function of β for Symanzik improved glue.

In Chapter 6, we discuss a novel improvement to the lattice fermion action known as the Fat-Link Irrelevant Clover (FLIC) fermion action. We show how this technique removes $\mathcal{O}(a)$ errors from previous discretisations of the fermion action providing a new form of non-perturbative improvement. We assess the problem of exceptional configurations with FLIC fermions and show that simulations in the quenched approximation can be successfully performed at quark masses corresponding to $m_\pi/m_\rho = 0.35$. Simulations at such light quark masses reveal non-analytic behavior of quenched chiral perturbation theory in decuplet baryon masses.

Chapter 7 contains results establishing the excited baryon spectrum using FLIC fermions. Good agreement is obtained between FLIC and other improved actions for the nucleon and its chiral partner. We also confirm earlier observations of a mass splitting between the two nearby $J^P = \frac{1}{2}^-$ states, however we find no evidence of overlap with the $\frac{1}{2}^+$ Roper resonance. Results for the excited hyperons are presented here.

The final set of calculations using FLIC fermions explores the spectrum of spin-$\frac{3}{2}$ baryons. These calculations are presented in Chapter 8. After spin and parity projection, we find good agreement for the spin-projected $\frac{1}{2}^+$ and $\frac{1}{2}^-$ states with earlier nucleon mass calculations using the standard spin-$\frac{1}{2}$ nucleon interpolating field. Furthermore, we find a good signal for the $N\frac{3}{2}^\pm$ states, with a mass difference of $\sim$ 300 MeV between the spin-$\frac{3}{2}$ parity partners. For the isospin-$\frac{3}{2}$ Δ states, clear mass splittings are observed between the various $\frac{1}{2}^\pm$ and $\frac{3}{2}^\pm$ channels, with the calculated level orderings in good agreement with those observed empirically.

Finally, in Chapter 9 we draw our conclusions and discuss some future extensions of this work.

2

QCD And The Standard Model

2.1 The Standard Model

The Standard Model of particle interactions encompases the four forces of nature - electromagnetism (EM), weak interactions (WI), strong interactions (SI) and gravity. The first three interactions are described by gauge field theories. EM and WI are low-energy manifestations of a single unified "electroweak" interaction. The SI originates in a hidden "colour" charge. The basic constituents of matter are the six quarks and six leptons which are summarised in Table 2.1. Each quark comes in one of six flavours and carries one of three colour charges. The quarks and leptons are ordered into three generations of families and they interact via vector bosons. The strong force is mediated by gluons; the electromagnetic force by the photon; and the weak force via the $W^{\pm}$, Z^0 bosons which aquire a mass via the Higgs mechanism. The standard model predicts the existence of a neutral Higgs particle.

In order to formulate a theoretical formulation of particle interactions, it is useful to note that physical laws are invariant under Poincare transformations (Lorentz transformations and space-time translations). Particles are then defined as a state of a quantum field that transforms under elements of the Poincare group according to a definite irreducible representation. This means

Quarks $J^P = \frac{1}{2}^+$			Leptons $S = \frac{1}{2}$		
flavour	*charge*	*mass*	*flavour*	*charge*	*mass*
up (u)	$\frac{2}{3}$	1–5 MeV	electron (e)	-1	0.511 MeV
down (d)	$-\frac{1}{3}$	3–9 MeV	e-neutrino (ν_e)	0	< 3 eV
strange (s)	$-\frac{1}{3}$	75–170 MeV	muon (μ)	-1	105.66 MeV
charm (c)	$\frac{2}{3}$	1.15–1.35 GeV	μ-neutrino (ν_μ)	0	< 0.19 MeV
bottom (b)	$-\frac{1}{3}$	4.0–4.4 GeV	tau (τ)	-1	1.777 GeV
top (t)	$\frac{2}{3}$	174.4±5.1 GeV	τ-neutrino (ν_τ)	0	< 18.2 MeV

Table 2.1: *Properties of Quarks and Leptons. Data from Particle Data Group, 2000. The quark masses are obtained in the $\overline{MS}$ scheme and are normalised at a renormalisation scale of $\mu = 2$ GeV.*

that particles will have definite mass and spin and have an associated antiparticle with the same mass and spin [1]. Observed particles can be grouped into two types - hadrons and leptons. Hadrons are bosons and fermions experiencing strong interactions whereas leptons are fermions without strong interactions.

Hadrons fall into two catagories - mesons and baryons. Mesons are bosons with baryon number equal to zero, whereas baryons are fermions with non-zero baryon number. The structure of hadrons can be understood by the multiplet structures identifiable with irreducible representations of an internal symmetry group $SU(3)$. This provides a need for hadronic constituents to form a fundamental representation of $SU(3)$. This leads to the idea of quarks.

2.2 Gauge Theories Of Interaction

The gauge principle formulated by Yang and Mills [2] applies to a multicomponent matter field. The group of transformations mix the different components of the matter field. This means that there will be more than one gauge field (c.f. EM which has only one, the photon). These are the Yang-Mills fields and the number of these gauge fields is equal to the number of generators of the gauge group. The relevant group for the weak, electromagnetic and strong interactions is $SU(2) \times U(1) \times SU(3)$.

It is well known that the weak interactions violate parity conservation. This is to do with the fact that only left-handed components of the leptons are coupled in the charge-changing sector. Similarly, hadronic weak interactions can be accounted for by assuming that quarks have the same kind of weak couplings. Thus, as far as weak interactions go, the elementary entities are states of definite chirality [1] which have zero mass.

Glashow [3] combined the gauge theories for electromagnetism and the weak interaction into a unified gauge theory of electroweak interactions based on a gauge group $SU(2) \times U(1)$ which mixes different massless chiral states. Physical particles, however, have finite mass which violates this symmetry. Weinberg [4] and Salam [5] accounted for this problem by introducing the concept of "spontaneous symmetry breaking". In the Weinberg-Salam model, "Higgs fields" are introduced to implement this idea.

Quarks and leptons of definite chirality come in at least six "flavours" which are in turn grouped into three generations of families. In addition, each quark flavour comes in three colours, while leptons have no colour. Quarks and leptons have the following internal symmetries

---

[1] chirality is defined as the eigenvalue of γ_5, with 1 corresponding to right-handedness and -1 to left-handedness

- **Colour** $SU(3)$: With respect to the colour index, the three quarks of each flavour form a triplet representation of a "colour group" $SU(3)$. Leptons are colour singlets.
- **Weak Isospin** $SU(2)$: In each family, the left-handed components of the upper and lower particles (eg., ν_L and e_L) form a doublet representation of a "weak isospin group" $SU(2)$. All right-handed particles are $SU(2)$ singlets.
- **Weak Hypercharge** $U(1)$: There is a $U(1)$ symmetry, called "weak hypercharge", associated with simultaneous phase changes of each particle. The relative phases are fixed by definite "weak hypercharge" assignments.

The gauge group is then $SU(2) \times U(1) \times SU(3)$, a direct product of the three mutually commuting groups defined above. There is now a need for 12 vector gauge fields, one for each group generator. Due to the non-abelian nature of the $SU(3)$ group, the gluon fields carry colour charge and as a result, are self-interacting.

As mentioned previously, the problem with this theory is that particles are massless. Including a mass term explicitly in the Lagrangian violates $SU(2) \times U(1)$ symmetry and leads to non-renormalisable theories. However, if we allow for "spontaneous symmetry breaking" of $SU(2) \times U(1)$ by a coupling to scalar "Higgs fields", then particles can now have mass.

The structure of colour $SU(3)$ means that quark-gluon coupling vanishes at large momenta (or small distances). This is called "asymptotic freedom". This means that it should be possible to detect quasi-free quarks inside a hadron using probes that impact at large momentum transfer. A second result of colour $SU(3)$ is that the quark-gluon coupling grows as the momenta is reduced to zero (distance scale goes to infinity). As a result, the potential energy between two charges ($Q\bar{Q}$) grows with an increase in separation (see also Chapter 4). This leads to the idea of a "string" joining the two charges. The string between the $Q\bar{Q}$ breaks when the energy in the string is large enough to create an additional $q\bar{q}$ out of the vacuum and create two mesons. This gives rise to the concept of quark "confinement" and provides for the result that quarks and gluons do not exist as isolated physical states, only as components of bound (hadron) states, which are colour singlets.

2.3 Quark Model

Hadrons fall into multiplets or families which reflect underlying internal symmetries. In order to explain this, it is necessary for hadrons to be composed of more elementary constituents with certain basic symmetries. Hence the need for quarks. Each multiplet is looked upon as the realisation of an irreducible representation of some internal symmetry group. Elements of each multiplet have nearly degenerate mass. If the masses in a multiplet are not exactly the same, the associated symmetry is only an approximate one.

In 1961, Murray Gell-Mann and Yuval Ne'eman [6] introduced the *Eightfold Way* which arranged the baryons and mesons into geometrical patterns, according to their charge and strangeness. Strange ($S \neq 0$) and non-strange ($S = 0$) hadrons together form families: meson octets and singlets (Fig. 2.1) and baryon octets (Fig.2.2) and decuplets (Fig. 2.3). The structure of these families can be understood in terms of the $SU(3)_{\text{flavour}}$ symmetry group. The $SU(3)_{\text{flavour}}$ symmetry is broken because the s quark is much heavier than the u and d quarks. As a consequence, there are large mass splittings among hadrons within each $SU(3)_{\text{flavour}}$ multiplet.

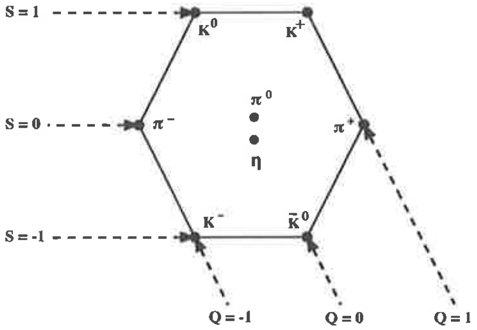

Figure 2.1: *The Meson Octet*

In an attempt to classify hadrons in terms of quarks, non-relativistic quark models assume that baryons are made of three quarks, qqq, and mesons of a quark-antiquark pair, $q\bar{q}$. These models have been fairly successful in the analysis of low-energy quantities such as the baryon spectrum.

A problem with early quark models was the pion-nucleon resonance Δ^{++} which has spin 3/2. The quantum numbers of Δ^{++} ($Q = +2$, $I_z = \frac{3}{2}$ and $S = 0$) suggest that it consists of three u quarks. If we combine $J_z = 3/2$ with the fact that the lowest energy for a three quark state has zero orbital angular momentum, we find that all three u quarks must have spin up. This senario is, of course, forbidden by the Pauli exclusion principle. We are therefore forced to conclude that the quarks carry an additional degree of freedom, a "colour charge", and we need the quarks to carry (at least) three different colours.

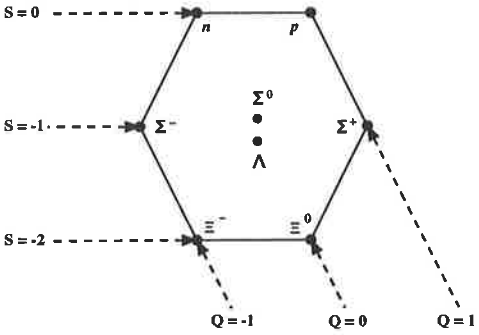

Figure 2.2: *The Baryon Octet*

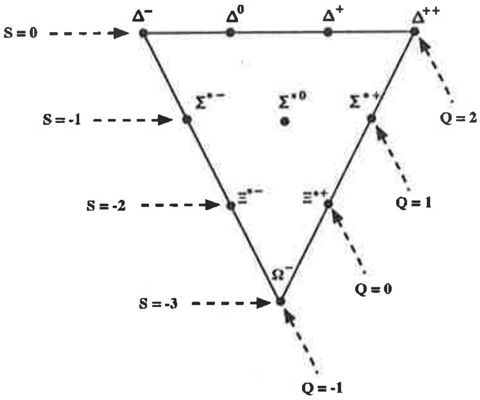

Figure 2.3: *The Baryon Decuplet*

Since the colour degrees of freedom are not observed experimentally, we say that hadronic observables are singlets of the colour symmetry $SU(3)$. If we assign a single quark to the fundamental representation **3**, then the direct product of three quarks decomposes into the irreducible representations

$$\mathbf{3}\otimes\mathbf{3}\otimes\mathbf{3}=\mathbf{1}\oplus\mathbf{8}\oplus\mathbf{8}\oplus\mathbf{10} \tag{2.1}$$

Similarly for mesons, since antiquarks belong to the conjugate representation $\bar{\mathbf{3}}$, quark-antiquark pairs correspond to one of the irreducible representations

$$\mathbf{3}\otimes\bar{\mathbf{3}}=\mathbf{1}\oplus\mathbf{8} \tag{2.2}$$

Since no meson carrying a colour quantum number has been observed experimentally, we must conclude that a quark and an antiquark which have the same colour, can form a colour singlet meson state.

2.4 Baryon Spectroscopy

If we consider a quark model with three flavours of quark, we can construct the group product of the fundamental triplet $SU(3)_{\text{flavour}}$ with a doublet of $SU(2)_{\text{spin}}$ to an $SU(6)$ representation. Baryons then fall into multiplets

$$\mathbf{6} \otimes \mathbf{6} \otimes \mathbf{6} = \mathbf{56} \oplus \mathbf{70} \oplus \mathbf{70} \oplus \mathbf{20}. \tag{2.3}$$

These $SU(6)$ multiplets can then be decomposed into the following $SU(3)$ flavour multiplets

$$\begin{aligned} \mathbf{56} &= {}^{4}\mathbf{10} \oplus {}^{2}\mathbf{8} \\ \mathbf{70} &= {}^{2}\mathbf{10} \oplus {}^{4}\mathbf{8} \oplus {}^{2}\mathbf{8} \oplus {}^{2}\mathbf{1} \\ \mathbf{20} &= {}^{2}\mathbf{8} \oplus {}^{4}\mathbf{1} \end{aligned} \tag{2.4}$$

where the superscript $(2S+1)$ gives the net spin of the quarks within each baryon. The $J^P = 1/2^+$ octet containing the nucleon and the $J^P = 3/2^+$ decuplet containing the $\Delta(1232)$ together make up the "ground-state" 56-plet in which the orbital angular momenta between the quark pairs are zero. The **70** and **20** multiplets require some excitation of the spatial part of the baryon wave function. States with orbital angular momenta are classified in $SU(6) \otimes O(3)$ supermultiplets. The orbital quantum numbers take values $N = 0,\ 1,\ 2,\ \ldots$ with the ground state having $N = 0$. We call this an *independent quark model*, in which quarks occupy single-particle orbitals, which are described by spatial wave functions and have definite energies. Masses of hadrons can then be calculated in terms of the energies of occupied orbitals and quark masses.

The classification of baryons is usually done by using the notation (D, L_N^P), where D refers to the dimensionality of the $SU(6)$ representation, the index N labels the oscillator quanta, P is the total parity, and L is the total quark orbital angular momentum. The $N = 0$ band contains the nucleon and $\Delta(1232)$ and consists only of the $(56,\ 0_0^+)$ supermultiplet. The $N = 1$ band consists only of the $(70,\ 1_1^-)$ multiplet which contains negative parity baryons including octets and decuplets with total spins $\frac{1}{2}$, $\frac{3}{2}$ and $\frac{5}{2}$. The $N = 2$ band contains five supermultiplets: $(56,\ 0_2^+)$, $(70,\ 0_2^+)$, $(56,\ 2_2^+)$, $(70,\ 2_2^+)$, and $(20,\ 1_2^+)$.

Many of the observed baryons can be sorted into one of the above multiplets. Table 2.2 shows the quark model assignments for many of the established baryons [7].

2.5 Baryon Mass Splittings

As seen in the previous section, we can form an $SU(6)$ spin-flavour representation for three quarks coupling to total spin S. If we place the quarks in a potential (eg. harmonic oscillator), then they will aquire orbital angular momentum L and the full symmetry group becomes $SU(6) \otimes O(3)$ with $L \oplus S = J$ generating the total angular momentum of the system. If we enforce the restriction that only symmetric $SU(6) \otimes O(3)$ representations exist (the so-called "symmetric quark model") then the 56-plet has the lowest energy. This is seen by considering three quarks in $1s$ states of a harmonic oscillator potential. The $O(3)$ state is then represented by

$$(1s)(1s)(1s) \equiv (1s)^3 \rightarrow L^P = 0^+$$

which is symmetric. It follows that for $SU(6) \otimes O(3)$ to be symmetric, then $SU(6)$ is symmetric, which is the 56-plet. This means that the lowest mass states in the spectrum are

$$\mathbf{10}: \; J^P = \frac{3}{2}^+ \; , \; \mathbf{8}: \; J^P = \frac{1}{2}^+$$

The first excited state is obtained by exciting one quark to $1p$ and the $O(3)$ state becomes

$$(1s)^2(1p) \rightarrow L^P = 1^-$$

It can be shown that only mixed symmetric $O(3)$ states exist (see for example [8]). Now to ensure that $SU(6) \otimes O(3)$ is symmetric we need a mixed symmetric $SU(6)$ which is the 70-plet. Hence the first excited band is predicted to contain the following negative parity states

$$\begin{aligned}
{}^2\mathbf{10}(S = \frac{1}{2}) &\oplus (L = 1) \rightarrow J^P = \frac{1}{2}^-, \frac{3}{2}^- \\
{}^2\mathbf{8}(S = \frac{1}{2}) &\oplus (L = 1) \rightarrow J^P = \frac{1}{2}^-, \frac{3}{2}^- \\
{}^4\mathbf{8}(S = \frac{3}{2}) &\oplus (L = 1) \rightarrow J^P = \frac{1}{2}^-, \frac{3}{2}^-, \frac{5}{2}^- \\
{}^2\mathbf{1}(S = \frac{1}{2}) &\oplus (L = 1) \rightarrow J^P = \frac{1}{2}^-, \frac{3}{2}^-
\end{aligned} \tag{2.5}$$

In a harmonic oscillator potential, the $L = 2$, $(1s)^2(1d)$ or $(1s)(1p)^2$ excitations are expected to be degenerate with the first radial excitation $(1s)^2(2s)$ for a three-quark system. However, in the observed baryon spectrum, the masses of the radial excitations overall are small. As an example, the $(56, 2_0^+)$ "Roper" $N(1440)$ state should be close to the $L = 2$, $(1s)$ level around 1700 MeV instead of the $L = 1$, $(1p)$ state around 1500 MeV.

The spin-spin force between quark (quark-antiquark) pairs in baryons (mesons) will separate the $s = \frac{1}{2}(0)$ and $s = \frac{3}{2}(1)$ baryon (meson) masses. For systems with $L > 0$, there is a possibility of a spin-orbit force between the quarks

$$\sum_{ij} \mathbf{L}_i \cdot \mathbf{S}_j$$

which leads to different masses for states with the same L and S but different J. Baryons have an additional $SU(3)$-dependent force

$$\mathbf{F}_i \cdot \mathbf{F}_j$$

where F_i are the $SU(3)_{\text{flavour}}$ generators, which splits the **1**, **8** and **10** multiplets.

In the quark model, the $N - \Delta$ mass splitting of about 300 MeV is thought to be a result of a quantum chromodynamic hyperfine splitting. If we replace one of the quarks in the Δ by a differnt flavour (eg. an s quark) then we obtain $\Sigma_s^*(sqq)$. The nucleon has the quarks pairwise in either $I = 1$ or 0 and upon replacing the third q by s gives $\Sigma_s(sqq)$ or $\Lambda_s(sqq)$ respectively. The masses of these baryons are given in Table 2.2 and from this we see that the act of substituting a strange quark for a u or d quark increases the mass of the 3-quark system by around 150-200 MeV. It also decreases the $\frac{3}{2}^+ - \frac{1}{2}^+$ mass splittings and splits the $\Lambda(I = 0)$ and $\Sigma(I = 1)$ states c.f. the negligible mass splitting between the $I = 0$ neutron and $I = 1$ proton. If we replace a second quark in Δ and N with another s quark, then the baryon system becomes $\Xi_s^*(ssq)$ and $\Xi_s(ssq)$.

In a quark model, it can be shown that the hyperfine splittings between octet and decuplet baryons is simply equal to the product of the magnetic moments of the singly and doubly represented quarks [8]. This means in the absence of strange quarks we have

$$\Delta - N = \mu_q^2. \tag{2.6}$$

In the strange quark sector, we have

$$\Xi_s^* - \Xi_s = \mu_s \mu_q = \Sigma_s^* - \Sigma_s. \tag{2.7}$$

This leads us to a formula with which we can compare mass splittings

$$\frac{\Sigma_s^* - \Sigma_s}{\Delta - N} = \frac{\mu_s}{\mu_q} = \frac{\Xi_s^* - \Xi_s}{\Delta - N} \tag{2.8}$$

Quark model calculations [9] with constituent quarks have shown that

$$\frac{\mu_s}{\mu_q} = \frac{\frac{1}{2}(m_u + m_d)}{m_s} \approx 0.639. \tag{2.9}$$

We can compare this to the experimental values displayed in Table 2.2

$$\begin{aligned} \Delta - N &= 293\,\mathrm{MeV} \\ \Sigma_s^* - \Sigma_s &= 192\,\mathrm{MeV} \\ \Xi_s^* - \Xi_s &= 212\,\mathrm{MeV}, \end{aligned}$$

which corresponds to ratios

$$\frac{\Sigma_s^* - \Sigma_s}{\Delta - N} = 0.655\ , \ \frac{\Xi_s^* - \Xi_s}{\Delta - N} = 0.724\ , \tag{2.10}$$

and we see that the simple quark model provides a reasonable estimate of the hyperfine splittings between octet and decuplet baryons.

2.6 The QCD Lagrangian

Quantum Chromodynamics (QCD) is a non-abelian gauge field theory describing the strong interactions. It is formulated in terms of coloured quarks and gluons and forms one of the components of the $SU(3) \times SU(2) \times U(1)$ Standard Model. As described in the previous sections, quarks have one of three colours, gluons come in eight colours and hadrons are colour-singlet combinations of quarks, anti-quarks and gluons. The Lagrangian describing the interaction of quarks and gluons is

$$\begin{aligned} \mathcal{L}_{QCD} &= -\frac{1}{4}F^{(a)}_{\mu\nu}F^{(a)\mu\nu} + i\sum_q \bar{\psi}^i_q \gamma^\mu (D_\mu)_{ij}\psi^j_q - \sum_q m_q \bar{\psi}^i_q \psi_{qi} \qquad (2.11) \\ F^{(a)}_{\mu\nu} &= \partial_\mu A^a_\nu - \partial_\nu A^a_\mu + g_s f_{abc} A^b_\mu A^c_\nu \qquad (2.12) \\ (D_\mu)_{ij} &= \delta_{ij}\partial_\mu - i g_s \sum_a \frac{\lambda^a_{ij}}{2} A^a_\mu \qquad (2.13) \end{aligned}$$

where g_s is the QCD (strong) coupling constant and is the only arbitrary parameter due to gauge invariance, f_{abc} are the structure constants of the $SU(3)_c$ algebra, $\psi^i_q(x)$ are four-component Dirac spinors associated with each quark field of colour i and flavour q, and A^a_μ are the Yang-Mills (gluon) fields. The Gell-Mann matrices, λ_a ($a = 1, 8$), are the generators of $SU(3)_c$ transformations and are 3×3 matrices that obey the following commutation relation

$$[\lambda_a, \lambda_b] \equiv \lambda_a \lambda_b - \lambda_b \lambda_a = 2i f_{abc} \lambda_c. \tag{2.14}$$

The Lagrangian in Eq. (2.11) is invariant under non-abelian local gauge transformations

$$\begin{aligned} \psi'_i(x) &= U_{ij}(x)\psi_j(x)\ , \qquad U(x) = \exp -iT^a\theta^a(x) \\ T^a A'^a(x)_\mu &= U(x)(T^a A^a_\mu(x) - \frac{i}{g}U^{-1}(x)\partial_\mu U(x))U^{-1}(x), \qquad (2.15) \end{aligned}$$

where θ^a are parameters which depend on x. In particular, $\mathcal{L}$ is invariant under space and time reversal and under Lorentz transformations.

In QCD, an isolated colour charge (quark) will surround itself with a virtual cloud of coloured quark-antiquark pairs in a similar way to how an isolated electric charge in QED polarises the vacuum and surrounds itself with electron-positron pairs. This virtual cloud of $q\bar{q}$ pairs has the effect of increasing α_s at short distances. However, unlike photons in QED which have zero electric charge, the gluons carry colour charge and hence they can interact with each other. This means that the isolated quark can also surround itself with gluons which causes α_s to decrease at short distances, tending asymptotically to zero. Infact, it can be shown (see for example Ref [10]) that asymptotic freedom occurs if $(33 - 2n_f) > 0$, where n_f is the number of quark flavours. Hence QCD enjoys the property of asymptotic freedom so long as the number of active quark flavours is less than 16.

As a result of asymptotic freedom, experiments probing a proton at short distances (large momentum transfer) will see the quarks inside the proton as quasi-free particles. At moderately short distances, α_s will be small and the quark interactions inside a hadron will be dominated via a single gluon exchange, similar to the single photon exchange seen in QED, and leads analagously to hyperfine splittings between singlet and triplet spin states of $q\bar{q}$ (as discussed in Section 2.5).

The Lagrangian in Eq. (2.11) includes self-interactions among the gauge fields, A^a_μ, through the term $gf^{abc}A^b_\mu A^c_\nu$ in $F^a_{\mu\nu}$ and is the main source of asymptotic freedom. This important feature of QCD where the renormalised QCD coupling is weak at high energies (short distances) allows quarks to behave as free particles. This enables high precision tests to be performed at high energies using perturbation theory.

At large separations, however, α_s increases as a result of there being eight gluons which are self-interacting and gives rise to confinement. This is the reason why individual quarks have not been seen experimentally.

				$S=-1$			
(D, L_N^P)	$SU(3)_f$	J^P	$S=0$	$I=0$	$I=1$	$S=-2$	$S=-3$
$(56, 0_0^+)$	$^2 8$	$\frac{1}{2}^+$	$N(939)$	$\Lambda(1116)$	$\Sigma(1193)$	$\Xi(1318)$	
	$^4 10$	$\frac{3}{2}^+$	$\Delta(1232)$		$\Sigma(1385)$	$\Xi(1530)$	$\Omega(1672)$
$(70, 1_1^-)$	$^2 8$	$\frac{3}{2}^-$	$N(1520)$	$\Lambda(1690)$	$\Sigma(1580)^{**}$	$\Xi(1820)$	
		$\frac{1}{2}^-$	$N(1535)$	$\Lambda(1670)$	$\Sigma(1620)^{**}$		
	$^4 8$	$\frac{1}{2}^-$	$N(1650)$	$\Lambda(1800)$	$\Sigma(1750)$		
		$\frac{5}{2}^-$	$N(1675)$	$\Lambda(1830)$	$\Sigma(1775)$		
		$\frac{3}{2}^-$	$N(1700)$		$\Sigma(1670)$		
	$^2 10$	$\frac{1}{2}^-$	$\Delta(1620)$				
		$\frac{3}{2}^-$	$\Delta(1700)$				
	$^2 1$	$\frac{1}{2}^-$		$\Lambda(1405)$			
		$\frac{3}{2}^-$		$\Lambda(1520)$			
$(56, 2_0^+)$	$^2 8$	$\frac{1}{2}^+$	$N(1440)$	$\Lambda(1600)$	$\Sigma(1660)$		
	$^4 10$	$\frac{3}{2}^+$	$\Delta(1600)^{**}$		$\Sigma(1690)^{**}?$		
$(56, 2_2^+)$	$^2 8$	$\frac{3}{2}^+$	$N(1720)$	$\Lambda(1890)$	?		
		$\frac{5}{2}^+$	$N(1680)$	$\Lambda(1820)$	$\Sigma(1915)$		
	$^4 10$	$\frac{1}{2}^+$	$\Delta(1910)$				
		$\frac{3}{2}^+$	$\Delta(1920)$		$\Sigma(2080)^{**}$		
		$\frac{5}{2}^+$	$\Delta(1905)$				
		$\frac{7}{2}^+$	$\Delta(1950)$		$\Sigma(2030)$		
$(56, 2_4^+)$	$^2 8$	$\frac{7}{2}^+$					
		$\frac{9}{2}^+$	$N(2220)$				
	$^4 10$	$\frac{5}{2}^+$					
		$\frac{7}{2}^+$					
		$\frac{9}{2}^+$	$\Delta(2300)^{**}$				
		$\frac{11}{2}^+$	$\Delta(2420)$				
$(70, 2_0^+)$	$^2 8$	$\frac{1}{2}^+$	$N(1710)$	$\Lambda(1810)$	$\Sigma(1880)^{**}$		
	$^4 8$	$\frac{3}{2}^+$					
	$^2 10$	$\frac{1}{2}^+$	$\Delta(1750)^{*}?$				
	$^2 1$	$\frac{1}{2}^+$	$N(2100)^{*}$				
$(70, 2_2^+)$	$^2 8$	$\frac{5}{2}^+$	$N(2000)^{**}?$	$\Lambda(2110)$	$\Sigma(2070)^{*}?$		
	$^4 8$	$\frac{7}{2}^+$	$N(1990)^{**}$				
$(56, 3_1^-)?$	$^2 8$	$\frac{1}{2}^-$	$N(2090)^{*}$		$\Sigma(2000)^{*}?$		
		$\frac{3}{2}^-$	$N(2080)^{**}$	$\Lambda(2325)^{*}?$			
	$^4 10$	$\frac{1}{2}^-$	$\Delta(1900)^{**}$				
		$\frac{3}{2}^-$	$\Delta(1940)^{*}$		$\Sigma(1940)$		
		$\frac{5}{2}^-$	$\Delta(1930)$				

Table 2.2: *Baryons and their resonances with $(u,\ d,\ s)$ valence quarks. Data from Particle Data Group, 2000. Data with a $*$ or $**$ are unconfirmed*

3

The Lattice

3.1 Lattice QCD

Lattice gauge theory, proposed by Ken Wilson in 1974 [11], is a nonperturbative method which uses the Feynman path integral approach and is the only way to perform a calculation of the nonperturbative properties of QCD from first principles. Lattice QCD is formulated in Euclidean space, which is accomplished by a Wick rotation from Minkowski space,

$$t \longrightarrow -it_E, \tag{3.1}$$

from now on we write t_E as t. In Lattice QCD, space-time is discretised into a four-dimensional grid or "lattice". In the "perfect field" approach, the quark fields $\psi(x)$ reside on the sites x of the lattice. These quark fields carry colour, flavour and Dirac indices as in the continuum theory. Gauge fields are represented by SU(3) colour matrices $U_\mu(x)$, where $\mu = 1, \ldots, 4$ are the space-time directions, and "link" a particular lattice site, x, with the adjacent site $x + \hat{\mu}$, where $\hat{\mu}$ denotes a vector in the μ direction with length of the lattice spacing, a. We refer to $\mu = 4$ as the time direction. The gluon fields, $A_\mu(x)$, of the QCD action are introduced by defining our gauge ("link") variables

$$U_\mu(x) = \mathcal{P} \exp ig \int_0^a A_\mu(x + \lambda\hat{\mu}) \mathrm{d}\lambda, \tag{3.2}$$

where the operator $\mathcal{P}$ path-orders the A_μ's along the integration path, a is the lattice spacing, and g is the coupling constant

Under a gauge transformation, $\Lambda(x)$, the fields transform as

$$\psi(x) \longrightarrow \Lambda(x)\psi(x), \qquad U_\mu(x) \longrightarrow \Lambda(x)U_\mu(x)\Lambda(x+\hat{\mu})^{-1}. \tag{3.3}$$

It is easy to see that the trace of a product of links along a closed loop will be gauge invariant. Other gauge invariant quantities of $SU(N)$ gauge theory are N gauge transporters whose colour indices are contracted at common start and end points using a completely antisymmetric tensor. The situation for $N = 3$ is shown in Fig. 3.1.

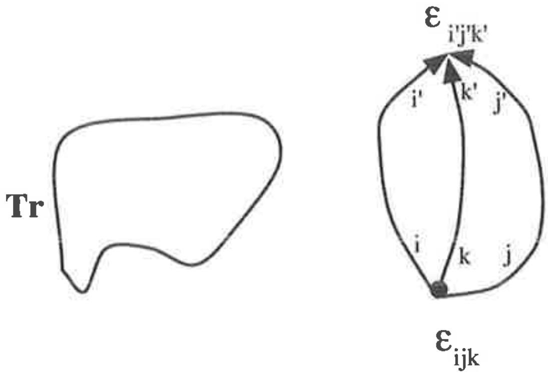

Figure 3.1: Examples of gauge invariant objects.

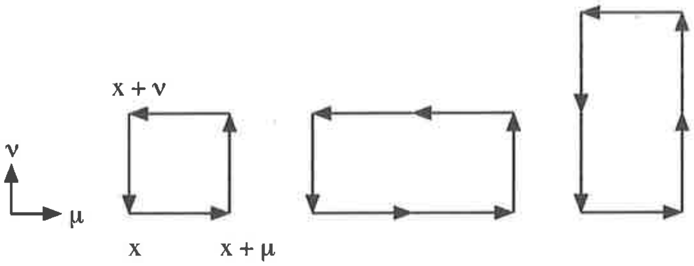

Figure 3.2: The plaquette, $P_{\mu\nu}(x)$, and 1×2 rectangles,$R_{\mu\nu}(x)$

The simplest non-trivial gauge-invariant object is the plaquette which is constructed via the product of of four links enclosing an elementary square,

$$\begin{aligned} P_{\mu\nu}(x) &= \frac{1}{3}\mathcal{R}e\mathrm{Tr}U_{\mathrm{sq}} \\ &= \frac{1}{3}\mathcal{R}e\mathrm{Tr}\left(U_\mu(x)U_\nu(x+\hat{\mu})U_\mu^\dagger(x+\hat{\nu})U_\nu^\dagger(x)\right), \end{aligned} \tag{3.4}$$

which is depicted in Fig. 3.2. We can rewrite Eq. (3.4) as

$$\begin{aligned} P_{\mu\nu}(x) &= \frac{1}{3}\mathcal{R}e\,\mathrm{Tr}\,\mathcal{P}e^{ig\oint_\square A\cdot\mathrm{d}x} \\ &= \frac{1}{3}\mathcal{R}e\,\mathrm{Tr}\,\mathcal{P}\left[1+ig\oint_\square A\cdot\mathrm{d}x-\frac{1}{2}\Big(g\oint_\square A\cdot\mathrm{d}x\Big)^2+\mathcal{O}(A^3)\right], \end{aligned} \tag{3.5}$$

where the path-ordering is essential in a non-abelian theory to ensure the action has errors which are $\mathcal{O}(a^2g^2)$. As we wish to remove classical $\mathcal{O}(a^2)$ errors from the action, it is sufficient to work with the abelian theory.

Stoke's Theorem for an abelian theory gives,

$$\begin{aligned}\oint_{\Box} A\cdot \mathrm{d}x &= \int_{-a/2}^{a/2} \mathrm{d}x_\mu \mathrm{d}x_\nu [\partial_\mu A_\nu(x_0+x) - \partial_\nu A_\mu(x_0+x)] \\ &= \int_{-a/2}^{a/2} \mathrm{d}x_\mu \mathrm{d}x_\nu \, F_{\mu\nu}(x_0+x) \\ &= a^2 F_{\mu\nu}(x_0) + \frac{a^4}{24}(\partial_\mu^2+\partial_\nu^2)F_{\mu\nu}(x_0) + \mathcal{O}(a^6,\, A^2). \end{aligned} \tag{3.6}$$

where x_0 is the centre of the loop, $F_{\mu\nu} = \partial_\mu A_\nu - \partial_\nu A_\mu$ is the abelian field strength tensor and the final equation is obtained via a Taylor expansion of $F_{\mu\nu}(x_0+x)$

We can now substitute Eq. (3.6) into Eq. (3.5) and considering only the real part, we obtain

$$P_{\mu\nu} = 1 - \frac{1}{6}g^2a^4 \mathrm{Tr}\, F_{\mu\nu}^2 - \frac{1}{72}g^2a^6 \mathrm{Tr}\, F_{\mu\nu}(\partial_\mu^2+\partial_\nu^2)F_{\mu\nu} + \mathcal{O}(a^8) + \mathcal{O}(g^4a^6). \tag{3.7}$$

Using this expansion for our plaquette operator, we arrive at the traditional "Wilson action" for gluons on the lattice,

$$S_{\mathrm{Wil}} = \beta \sum_{x,\mu>\nu} (1 - P_{\mu\nu}(x)), \tag{3.8}$$

where $\beta = 6/g^2$. This action differs from the continuum gluon action (first term in Eq. (2.11)) by terms which are $\mathcal{O}(a^2)$ and $\mathcal{O}(g^2a^2)$. The a^2 errors can be removed by adding other products of links that form closed loops (known as Wilson loops). An obvious first choice would be 1 × 2 rectangular loops as illustrated in Fig. 3.2. Such loops have the expansion

$$\begin{aligned} R_{\mu\nu}^{1\times2} &= 1 - \frac{4}{6}g^2a^4\mathrm{Tr}\, F_{\mu\nu}^2 - \frac{4}{72}g^2a^6\mathrm{Tr}\, \left(F_{\mu\nu}(4\partial_\mu^2+\partial_\nu^2)F_{\mu\nu}\right) - \ldots \\ R_{\mu\nu}^{2\times1} &= 1 - \frac{4}{6}g^2a^4\mathrm{Tr}\, F_{\mu\nu}^2 - \frac{4}{72}g^2a^6\mathrm{Tr}\, \left(F_{\mu\nu}(\partial_\mu^2+4\partial_\nu^2)F_{\mu\nu}\right) - \ldots . \end{aligned} \tag{3.9}$$

Since $R_{\mu\nu}$ and $P_{\mu\nu}$ have different $\mathcal{O}(a^2)$ errors, they may be added to obtain an improved lattice action that is accurate up to $\mathcal{O}(a^4)$ and $\mathcal{O}(g^2a^2)$ [12, 13]

$$S_{\mathrm{Imp}} = \beta \sum_{x,\mu>\nu} \left\{ \frac{5}{3}(1-P_{\mu\nu}) - \frac{1}{12}(1-R_{\mu\nu}^{1\times2}) + \frac{1}{12}(1-R_{\nu\mu}^{2\times1}) \right\} \tag{3.10}$$

$$= a^4 \sum_{x,\mu>\nu} \left[\frac{1}{2}\mathrm{Tr}\, F_{\mu\nu}^2 + \mathcal{O}(a^4) + \mathcal{O}(a^2g^2) \right], \tag{3.11}$$

which reproduces the continuum action to $\mathcal{O}(a^4)$ and $\mathcal{O}(a^2g^2)$.

3.2 Mean-Field Improvement

Gauge fields are represented by the link operator (Eq. 3.2) which can be Taylor expanded to give

$$U_\mu(x) \approx 1 + iagA_\mu(x) - \frac{a^2g^2}{2}A_\mu^2(x) + \ldots \tag{3.12}$$

All but the first two terms are lattice artifacts in the QCD action and give rise to quark-gluon vertices with two or more gluons. Contracting the two gluons in $a^2g^2A_\mu^2(x)/2$ produces tadpole diagrams. These extra vertices are suppressed by powers of a and hence are irrelevant for classical fields. Lepage and Mackenzie [14] pointed out that for quantum fields, however, pairs of A_μ's contracted with each other generate ultraviolet divergent factors of $1/a^2$ that precisely cancel the extra a's. Consequently, the contributions generated by these tadpole loops are, infact, only suppressed by powers of g^2 and result in large renormalisations that spoil naive perturbative lattice expansions. However, tadpole contributions are process independent so it is possible to measure their contribution in one quantity and then correct for them in all other quantities. The simplest way of removing these artifacts is by mean-field improvement (also known as tadpole improvement).

If we assume that the lattice fields can be split into UV and IR parts, then mean-field improvement is performed by simply integrating out the UV part, *i.e.*

$$e^{iagA_\mu(x)} = e^{iag(A_\mu^{\rm IR}(x)+A_\mu^{\rm UV}(x))} \sim u_0 e^{iagA_\mu^{\rm IR}(x)} \equiv u_0\tilde{U}_\mu(x). \tag{3.13}$$

Rescaling of the links by an overall constant $u_0 \leq 1$ leaves the theory gauge-invariant. Under this scaling, in every lattice operator we replace $U \to \tilde{U}$. The u_0's have the effect of cancelling tadpole contributions which enable lattice operators and perturbation theory to be far more continuum-like in their behaviour. Since we only ever consider the real part of correlation functions, we can choose u_0 to be real.

There are two common choices for computing the mean-field improvement parameter (or "mean link"), u_0: (i) the fourth root of the plaquette (Eq. (3.14)), and (ii) the expectation value of the link in Landau gauge. These two definitions give almost identical results, however since gauge fixing is unnecessay in the first definition, the most common choice is the first approximation and it is this definition that is used for all calculations presented in this thesis.

$$u_0 = \left(\frac{1}{3}\mathcal{R}e\,\mathrm{tr}\langle U_{\rm sq}\rangle\right)^{1/4}. \tag{3.14}$$

We return now to our expression for the improved gluon action given in Eq. (3.10). We can tadpole improve this action by dividing each link operator U_μ by the mean link u_0

$$S = \beta \sum_{x,\mu>\nu} \left\{ \frac{5}{3}(1 - \frac{P_{\mu\nu}}{u_0^4}) - \frac{1}{12}(1 - \frac{R_{\mu\nu}^{1\times 2}}{u_0^6}) + \frac{1}{12}(1 - \frac{R_{\mu\nu}^{2\times 1}}{u_0^6}) \right\} \tag{3.15}$$

The u_0's cancel tadpole contributions that would otherwise spoil weak-coupling perturbation theory in the lattice theory and undermine our procedure for improving the lattice discretization. Without tadpole improvement, only about half of the a^2 errors are cancelled. Moreover, perturbative corrections to this action are estimated to be of the order of two to three percent [15].

The mean link u_0 must be determined self-consistently as the relative coefficients in the action themselves depend on u_0. To do this, u_0 is computed numerically by initialising u_0 to 1, measuring the mean link in a simulation, and then readjusting the value used in the action accordingly. The u_0's depend only on the lattice spacing and become equal to one as the lattice spacing vanishes, providing an $\mathcal{O}(a^2)$ improved transistion to the continuum.

3.3 The Lattice Quark Action

3.3.1 The Naive Fermion Action

In Euclidean space-time, the Dirac action obtained from Eq. (2.11) is written as

$$\bar{\psi}(\not{D} + m)\psi \tag{3.16}$$

Wilson [11] discretised the continuum Dirac action (Eq. (3.16)), by replacing the derivative with a symmetrised finite difference and including appropriate gauge links to not only encode the gluon field, A_μ, but to also maintain gauge invariance

$$\bar{\psi}\not{D}\psi = \frac{1}{2a}\bar{\psi}(x)\sum_\mu \gamma_\mu \Big[U_\mu(x)\psi(x+\hat{\mu}) - U_\mu^\dagger(x-\hat{\mu})\psi(x-\hat{\mu}) \Big]. \tag{3.17}$$

The continuum Dirac action is recovered in the limit $a \to 0$ by Taylor expanding the U_μ and $\psi(a+\hat{\mu})$ in powers of the lattice spacing a. Keeping only the leading term in a, Eq. (3.17) becomes

$$\begin{aligned} \frac{1}{2a}\bar{\psi}(x)\gamma_\mu[\quad & (\quad 1 + iagA_\mu(x+\frac{\hat{\mu}}{2}) + \ldots)(\psi(x) + a\psi'(x) + \ldots) - \\ & (\quad 1 - iagA_\mu(x-\frac{\hat{\mu}}{2}) + \ldots)(\psi(x) - a\psi'(x) + \ldots)] \\ = \bar{\psi}(x)\gamma_\mu(\partial_\mu \quad + & \quad \mathcal{O}(a^2))\psi(x) + ig\bar{\psi}(x)\gamma_\mu[A_\mu + \mathcal{O}(a^2)]\psi(x), \end{aligned} \tag{3.18}$$

which is the kinetic part of the standard continuum Dirac action in Euclidean space-time (Eq. (2.11)) to $\mathcal{O}(a^2)$. Hence we arrive at the simplest ("naive") lattice fermion action,

$$\begin{aligned} S_N &= m_q \sum_x \bar{\psi}(x)\psi(x) \\ &+ \frac{1}{2a}\sum_{x,\mu} \bar{\psi}(x)\gamma_\mu \Big[U_\mu(x)\psi(x+\hat{\mu}) - U_\mu^\dagger(x-\hat{\mu})\psi(x-\hat{\mu})\Big] \\ &\equiv \sum_x \bar{\psi}(x) M_{xy}^N[U]\psi(y), \end{aligned} \tag{3.19}$$

where the interaction matrix M^N is

$$M_{i,j}^N[U] = m_q\delta_{ij} + \frac{1}{2a}\sum_\mu [\gamma_\mu U_{i,\mu}\delta_{i,j-\mu} - \gamma_\mu U_{i-\mu,\mu}^\dagger \delta_{i,j+\mu}]. \tag{3.20}$$

The Euclidean γ matrices are hermitian, $\gamma_\mu = \gamma_\mu^\dagger$, and satisfy $\{\gamma_\mu, \gamma_\nu\} = 2\delta_{\mu\nu}$. For the fermion action, the Sakurai representation (given in Appendix A) is used

The Taylor expansion in Eq. (3.18) shows that the naive fermion action of Eq. (3.19) has $\mathcal{O}(a^2)$ errors. It also preserves chiral symmetry, however in the continuum limit, it gives rise to $2^d = 16$ flavours of quark rather than one. This is the famous doubling problem and is easily demonstrated by considering the inverse of the free field propagator (obtained by taking the fourier transform of the action with all $U_\mu = 1$)

$$S^{-1}(p) = m_q + \frac{i}{a}\sum_\mu \gamma_\mu \sin p_\mu a \tag{3.21}$$

which has 16 zeros within the Brillouin cell in the limit $m_q \to 0$. eg, $p_\mu = (0,0,0,0)$, $(\pi/a,0,0,0)$, $(\pi/a,\pi/a,0,0)$, etc. Consequently, this action is phenomenologically not acceptable.

There are two approaches commonly used to remove these doublers. The first involves adding operators to the quark action which scale with the lattice spacing and thus vanish in the continuum limit. These operators are chosen to drive the doublers to high energies and hence are suppressed. This technique for improving fermion actions proceeds via the improvement scheme proposed by Symanzik [16] and is discussed in more detail in the following sections. The second method for removing doublers involves "staggering" the quark degrees of freedom on the lattice. This procedure exploits the fact that the naive fermion action has a much larger symmetry group, $U_V(4)\otimes U_A(4)$, to reduce the doubling problem from $2^d = 16 \to 16/4$ while maintaining a remnant chiral symmetry. This approach is not used in this thesis so the details of the action will not be discussed here. Details of the derivation of staggered fermions can be found in most texts (eg. [17, 18]).

3.3.2 Wilson Fermions

In order to avoid the doubling problem, Wilson [11] originally introduced an irrelevant (energy) dimension-five operator (the "Wilson term") to the standard naive lattice fermion action (Eq. (3.19)), which explicitly breaks chiral symmetry at $\mathcal{O}(a)$

$$S_{\mathrm{W}} = \bar{\psi}(x)\left[\sum_{\mu}\left(\gamma_\mu \nabla_\mu - \frac{1}{2} r a \Delta_\mu\right) + m\right]\psi(x)\ , \tag{3.22}$$

where

$$\nabla_\mu \psi(x) = \frac{1}{2a}[U_\mu(x)\psi(x+\hat{\mu}) - U^\dagger_\mu(x-\hat{\mu})\psi(x-\hat{\mu})] \tag{3.23}$$

and

$$\Delta_\mu \psi(x) = \frac{1}{a^2}[U_\mu(x)\psi(x+\hat{\mu}) + U^\dagger_\mu(x-\hat{\mu})\psi(x-\hat{\mu}) - 2\psi(x)]. \tag{3.24}$$

The Wilson term removes the doublers by giving the extra fifteen species at $p_\mu = \pi$ a mass proportional to r/a. In terms of link variables, $U_\mu(x)$, the Wilson action can be written

$$\begin{aligned} S_W &= \left(m_q + \frac{4r}{a}\right)\sum_x \bar{\psi}(x)\psi(x) + \frac{1}{2a}\sum_{x,\mu}\bar{\psi}(x)\Big[(\gamma_\mu - r)U_\mu(x)\psi(x+\hat{\mu}) \\ &\qquad -(\gamma_\mu + r)U^\dagger_\mu(x-\hat{\mu})\psi(x-\hat{\mu})\Big] \qquad (3.25) \\ &\equiv \sum_{x,y}\bar{\psi}^L_x M^W_{xy}\psi^L_y \qquad (3.26) \end{aligned}$$

where the interaction matrix for the Wilson action, M^W, is usually written

$$M^W_{xy}[U]a = \delta_{xy} - \kappa\sum_\mu\Big[(r-\gamma_\mu)U_{x,\mu}\delta_{x,y-\mu} + (r+\gamma_\mu)U^\dagger_{x-\mu,\mu}\delta_{x,y+\mu}\Big] \tag{3.27}$$

with a field renormalisation

$$\begin{aligned} \kappa &= 1/(2m_q a + 8r) \\ \psi^L &= \psi/\sqrt{2\kappa}. \end{aligned} \tag{3.28}$$

We take the standard value $r = 1$ and the quark mass is given by

$$m_q a = \frac{1}{2}\left(\frac{1}{\kappa} - \frac{1}{\kappa_c}.\right) \tag{3.29}$$

In the free theory the critical value of kappa, κ_c, where the quark mass vanishes, is $1/8r$. In the interacting theory, κ_c moves away from $1/8r$ and the quark mass has both multiplicative and additive renormalisations due to the explicit chiral symmetry breaking by the Wilson term.

In the continuum limit, we find

$$S_W = \int d^4x \bar{\psi}(x)(\not{D} + m - \frac{ar\not{D}^2}{2})\psi(x) + \mathcal{O}(a^2), \tag{3.30}$$

so we see that by lifting the mass of the unwanted doublers with a second derivative, we have introduced $\mathcal{O}(a)$ discretisation errors to the fermion matrix. In contrast, the Wilson gauge action (Eq. (3.8)) has only $\mathcal{O}(a^2)$ errors so there has been an enormous amount of interest in applying Symanzik's improvement program [16] to the fermion action by adding higher dimension terms.

3.3.3 Improving The Fermion Action

The addition of the Wilson term to the fermion action introduces large $\mathcal{O}(a)$ errors which mean that in order to extrapolate reliably to the continuum limit, simulations must be performed on fine lattices, which are therefore very computationally expensive. The scaling properties of the Wilson action at finite a can be improved by introducing any number of irrelevant operators of increasing dimension which vanish in the continuum limit.

The first attempt at removing these $\mathcal{O}(a)$ errors was by Hamber and Wu [19] who added a two link term to the Wilson action

$$\begin{aligned} S_{HW} = S_W \quad &+ \quad \kappa \sum_{x,\mu} \Big[\bar{\psi}^L(x)(-\frac{1}{4}r + \frac{1}{8}\gamma_\mu)U_\mu(x)U_\mu(x+\hat{\mu})\psi^L(x+2\hat{\mu}) \\ &+ \quad \bar{\psi}^L(x+2\hat{\mu})(-\frac{1}{4}r - \frac{1}{8}\gamma_\mu)U^\dagger_\mu(x+\hat{\mu})U^\dagger_\mu(x)\psi^L(x)\Big]. \end{aligned} \tag{3.31}$$

The removal of the $\mathcal{O}(a)$ terms is easily observed through a Taylor expansion. While this action also removes $\mathcal{O}(a^2)$ errors at tree-level, it has only received a small amount of interest due to computational expense in evaluating the double hopping term. Calculations that have been done with this action show that it works well at coarse lattice spacings and has the added bonus that it has an improved dispersion relation [20].

A more popular alternative is to consider all possible gauge invariant, local dimension-five operators that can be added to the fermion action

$$\begin{aligned}
\mathcal{O}_1 &= -\frac{iaC_{SW}r}{4}\bar{\psi}i\sigma_{\mu\nu}F_{\mu\nu}\psi, \\
\mathcal{O}_2 &= c_1 a\left\{\bar{\psi}D_\mu D_\mu\psi + \bar{\psi}\overleftarrow{D}_\mu\overleftarrow{D}_\mu\psi\right\}, \\
\mathcal{O}_3 &= \frac{b_g am}{2g^2}\mathrm{tr}\{F_{\mu\nu}F_{\mu\nu}\}, \\
\mathcal{O}_4 &= c_2 m\left\{\bar{\psi}\gamma_\mu D_\mu\psi - \bar{\psi}\overleftarrow{D}_\mu\gamma_\mu\psi\right\}, \\
\mathcal{O}_5 &= -b_m am^2\bar{\psi}\psi.
\end{aligned} \tag{3.32}$$

At tree-level, it is possible to remove the second and fourth operators by the following transformation of the fermion fields

$$\begin{aligned}
\psi &\rightarrow \psi' = (1+b_q am)(1-c_q a\not{D})\psi \\
\bar{\psi} &\rightarrow \bar{\psi}' = (1+b_q am)\bar{\psi}(1+c_q a\overleftarrow{\not{D}}).
\end{aligned} \tag{3.33}$$

At tree-level, $b_q = c_q = 1/4$. The third and fifth operators in Eq. (3.32) are incorporated by renormalising $g^2 \rightarrow g^2(1+b_g ma)$ and $m \rightarrow m(1+b_m ma)$. This is equivalent to a rescaling of the bare coupling and the quark mass. When working in the quenched approximation, it is common to set $b_g = 0$. The remaining dimension-five operator, the magnetic moment, or "clover" term, when added to the Wilson action gives us the popular Sheikholeslami-Wohlert fermion [21] action

$$S_{SW} = S_W - \frac{iaC_{SW}r}{4}\,\bar{\psi}(x)\sigma_{\mu\nu}F_{\mu\nu}\psi(x)\ , \tag{3.34}$$

where C_{SW} is the clover coefficient which can be tuned to remove $\mathcal{O}(a)$ artifacts,

$$C_{SW} = \begin{cases} 1 & \text{at tree-level}\ , \\ 1/u_0^3 & \text{mean-field improved}\ , \end{cases} \tag{3.35}$$

with u_0 the tadpole improvement factor correcting for the quantum renormalisation of the operators. Nonperturbative (NP) $\mathcal{O}(a)$ improvement [22] uses the axial Ward identity to tune C_{SW} and remove all $\mathcal{O}(a)$ artifacts provided one simultaneously improves the coupling g^2, the quark mass m_q, and the currents [22]. The advantage of the clover action is that it is local and is only a ~ 15% overhead on Wilson fermion simulations. Further details of the improvement the clover action provides at finite lattice spacing is given in Chapter 6.

The name "clover" is associated with the SW fermion action due to the lattice discretisation of the field strength tensor, $F_{\mu\nu}$. An expression for $F_{\mu\nu}$ is obtained by considering the sum of the four plaquettes surrounding any lattice

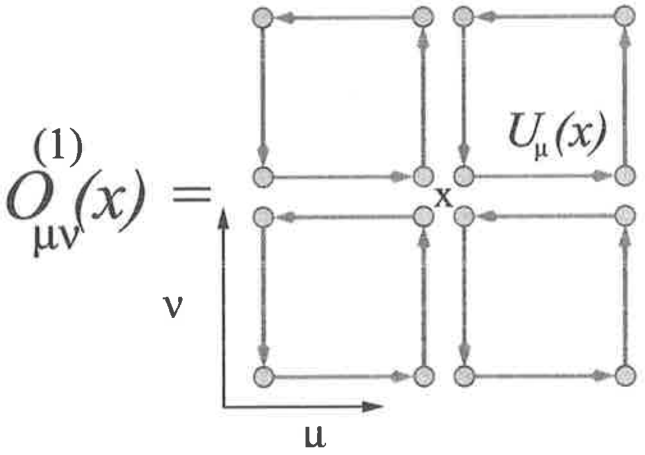

Figure 3.3: Loops required to construct $F_{\mu\nu}$

site in the $\mu - \nu$ plane as shown in Fig. 3.3. Using the expansion in Eq. (3.5) and (3.6) for the plaquette, we obtain the lattice expression for $F_{\mu\nu}$

$$ga^2 F_{\mu\nu} = \frac{-i}{2}\left[\mathcal{O}^{(1)}_{\mu\nu} - \mathcal{O}^{(1)\dagger}_{\mu\nu} - \frac{1}{3}\mathrm{Tr}(\mathcal{O}^{(1)}_{\mu\nu} - \mathcal{O}^{(1)\dagger}_{\mu\nu})\right], \tag{3.36}$$

where we have made $F_{\mu\nu}$ traceless by subtracting 1/3 of the trace from each diagonal element. Substantial progress has been made to improve $F_{\mu\nu}$ to $\mathcal{O}(a^6)$ by adding terms constructed using larger Wilson loops [23]. A discussion of improving $F_{\mu\nu}$ can be found in Appendix B.

3.3.4 Highly Improved Actions

In the previous section we have described how it is possible to remove $\mathcal{O}(a)$ errors from the fermion action by introducing the dimension-five clover term. This action, however, may still have a^2 errors which become large at coarse lattice spacings. For this reason there has been some interest in developing a quark action that has errors only of $\mathcal{O}(a^3)$ and higher.

An attempt at such an improved action is the $D234$ class of actions introduced by Alford, Klassen and Lepage [24] which involves second, third and fourth order derivatives. For isotropic lattices,

$$\begin{aligned} M_{D234c} &= m(1+0.5ram) + \sum_\mu \left\{\gamma_\mu \Delta^{(1)}_\mu - \frac{C_3}{6}a^2\gamma_\mu\Delta^{(3)}_\mu\right\} \\ &+ r\sum_\mu \left\{-\frac{1}{2}a\Delta^{(2)}_\mu - \frac{iaC_F}{4}\sigma_{\mu\nu}F_{\mu\nu} + \frac{C_4}{24}a^2\Delta^{(4)}_\mu\right\}, \end{aligned} \tag{3.37}$$

where $\Delta_\mu^{(n)}$ is the n^{th} order lattice covariant derivative. The term proportional to C_3 is precisely what is needed to kill the leading discretisation error in $\Delta_\mu^{(1)}$ as shown in Eq. (3.18). The terms proportional to r are generated by a field redefinition and thus represent a redundant operator. They, therefore leave unaltered the $\mathcal{O}(a)$ improvement of the naive action. We recognise the three irrelevant terms as the Wilson term, the clover term, and an a^3 correction. At tree-level, the coefficients are unity. As with the Sheikoleslami-Wohlert action, quantum corrections can be included by mean-field improving each coefficient. The coefficients may also be tuned non-perturbatively and tests show that errors are small even at coarse lattice spacings [24]. This action, however, is significantly more computationally expensive than the Wilson or clover actions and as such is not a common choice.

3.4 Lattice Calculations

3.4.1 The Path Integral

The starting point for any Lattice QCD calculation is with the partition function in Euclidean space ($t \to -i\,t$)

$$Z = \int \mathcal{D}A_\mu \, \mathcal{D}\psi \, \mathcal{D}\overline{\psi} \, e^{-S} \tag{3.38}$$

where $S = \int d^4x \, (\frac{1}{4} F_{\mu\nu}F^{\mu\nu} - \overline{\psi} M \psi)$ is the QCD action, M is the Dirac fermion matrix, and $F_{\mu\nu} = \partial_\mu A_\nu - \partial_\nu A_\mu + ig[A_\mu, A_\nu]$ is the field strength tensor. The gauge fields are represented by A_μ and the fermion fields by the Grassmann variables ψ and $\overline{\psi}$ which can be integrated out

$$Z = \int \mathcal{D}A_\mu \, \mathrm{det}M \, e^{\int d^4x \, (\frac{1}{4} F_{\mu\nu}F^{\mu\nu})} \tag{3.39}$$

The fermionic contribution to the action is now contained in $\mathrm{det}M$ and Z is now only an integral over background gauge configurations. The QCD action can now be written

$$S = S_{\mathrm{gauge}} + S_{\mathrm{quarks}} = \int d^4x \, (\frac{1}{4} F_{\mu\nu}F^{\mu\nu} - \sum_i \log \mathrm{det}M_i), \tag{3.40}$$

where the sum in the last term is over quark flavours. By setting $\mathrm{det}M = constant (= 1)$, we remove the contribution of sea quark loops to the path integral. This is known as the "*Quenched Approximation*" and results presented in this thesis are made using this approximation. Historically, the justification for such an approximation is the phenomenological observation that the neglect of sea quark loops corresponds to the neglect of OZI-suppressed processes. This is expected to be valid for large quark masses where the momentum transfer in gluons required to create the $q\bar{q}$ pair becomes large. As a result, g becomes small due to asymptotic freedom. Another aspect is that the quenched approximation emerges in the large N_c limit of QCD, where N_c is the number of colours. Also, sea quark loops have a perturbative effect of simply renormalising the coupling, g. Since we set the scale by comparing to phenomenological quantities, the renormalisation of g is absorbed in setting the scale. However, quenched chiral perturbation theory tells us that calculations made at small quark masses will suffer non-analyticities due to differences in the meson cloud. Non-analytic behaviour in the Δ mass is a good example of this and is seen for the first time in quenched simulations through the use of FLIC fermions in Chapter 6.

3.4.2 Expectation Values Of Observables

Any ensemble of lattice gauge field configurations $\{U^{[i]}\}$ is created through a Markov process [17]. This involves generating each configuration $U^{[i]}$ from the preceding one, $U^{[i-1]}$, using a Monte Carlo algorithm satisfying

$$P(U^{[i-1]} \rightarrow U^{[i]})P[U^{[i-1]}] = P(U^{[i]} \rightarrow U^{[i-1]})P[U^{[i]}] \tag{3.41}$$

where $P(U \rightarrow U')$ is the probability of generating configuration U' from the configuration U and depends on $\beta = 6/g^2$, the parameter which fixes the lattice spacing. The initial configuration $U^{[0]}$ is usually chosen to be "cold", *i.e.* when all the links are set to the identity, or "hot", where each link is a random $SU(3)$ matrix [25, 26]

Calculation of physical observables are obtained via expectation values

$$\langle \mathcal{O}(\ldots) \rangle = \frac{1}{Z} \int \mathcal{D}A_\mu \, \mathcal{O} \, e^{-S} \simeq \frac{1}{N} \sum_i \mathcal{O}(\ldots [U^{[i]}]), \tag{3.42}$$

where N is the number of generated configurations. The operator $\mathcal{O}$ can be any given combination of operators expressed in terms of time-ordered products of gauge and quark fields. Using Wick's Theorem for contracting fields, it is possible to re-express quark fields in terms of quark propagators, removing any dependence on the quark fields as dynamical variables. The quark propagator is calculated by simply inverting the Dirac operator on any given background field

$$S_F(y, j, b; x, i, a) = (M^{-1})^{y,j,b}_{x,i,a}. \tag{3.43}$$

This gives the amplitude for the propagation of a quark from site x with spin-colour i, a to site-spin-colour y, j, b.

In order to gain an idea of how to proceed in calculating physical observables, consider the momentum-space two-point function where $t > 0$

$$G(\vec{p},t) = \int d^3p\, e^{-i\vec{p}.\vec{x}} \langle \Omega | T[\mathcal{O}_f(\vec{x},t)\mathcal{O}_i(0)] | \Omega \rangle \,. \tag{3.44}$$

If we let $\mathcal{O}_f = \mathcal{O}_i = A_4 = \bar{\psi}\gamma_4\gamma_5\psi$, the fourth component of the axial current, which has a large coupling to the pion, the 2-point function in Eq. (3.44) now describes the procedure where the "source" operator, $\mathcal{O}_i$, creates a state with quantum numbers of the pion from the vacuum; the evolution of this state via the QCD Hamiltonian to the point $(\vec{x},t)$; and the annihilation of this state by the "sink" operator, $\mathcal{O}_f$, back to the vacuum. Since $\mathcal{O}_i$ will create a state that is a linear combination of all eigenstates of the Hamiltonian that have the quantum numbers of the pion, *i.e.* the pion and its excited states, we can insert a complete set of intermediate states, n, with momentum, p', in Eq. (3.44),

$$G(\vec{p},t) = \int d^3p\, e^{-i\vec{p}\cdot\vec{x}} \int d^3p' \sum_{n=1}^{N} \langle \Omega | \mathcal{O}_f(\vec{x},t) | n, p' \rangle \langle n, p' | \mathcal{O}_i(0) | \Omega \rangle \,, \tag{3.45}$$

We can make use of translational invariance to write

$$\begin{aligned} G(\vec{p},t) &= \int d^3p\, e^{-i\vec{p}\cdot\vec{x}} \int d^3p' \sum_{n=1}^{N} \langle \Omega | e^{\hat{H}t} e^{-i\hat{\vec{P}}\cdot\vec{x}} \mathcal{O}_f(0) e^{i\hat{\vec{P}}\cdot\vec{x}} e^{-\hat{H}t} | n, p' \rangle \langle n, p' | \mathcal{O}_i(0) | \Omega \rangle \\ &= \int d^3p \int d^3p'\, e^{-i(\vec{p}-\vec{p}')\cdot\vec{x}} \sum_{n=1}^{N} e^{-E_n t} \langle \Omega | \mathcal{O}_f(0) | n, p' \rangle \langle n, p' | \mathcal{O}_i(0) | \Omega \rangle \\ &= \sum_{n=1}^{N} e^{-E_n t} \langle \Omega | \mathcal{O}_f(0) | n, p \rangle \langle n, p | \mathcal{O}_i(0) | \Omega \rangle \,. \end{aligned} \tag{3.46}$$

At $\vec{p} = 0$, $E_n \to M_n$ and masses are extracted. If $\mathcal{O}$ has overlap with more than one state, then as a result of exponential damping, the ground (lowest mass) state can be isolated by examining the large t behaviour of Eq. (3.46)

$$G(\vec{p},t) \overset{t\to\infty}{=} \langle \Omega | \mathcal{O}_f(0) | \pi \rangle \langle \pi | \mathcal{O}_i(0) | \Omega \rangle\, e^{-M_\pi t}. \tag{3.47}$$

Since $\langle \Omega | A_4(\vec{p} = 0) | \pi \rangle = M_\pi f_\pi$, the pion mass and decay constant are extracted from the exponential fall-off in time and from the amplitude respectively.

If we now consider all the possible Wick contractions of the two fermion fields in Eq. (3.47), the correlation function can now be written in terms of a product of two quark propagators, S_F,

$$\begin{aligned} \langle \Omega | A_4^\dagger(x) A_4(0) | \Omega \rangle &= -\langle \Omega | \bar{\psi}(x)\gamma_4\gamma_5\psi(x)\, \bar{\psi}(0)\gamma_4\gamma_5\psi(0) | \Omega \rangle \\ &= \langle \Omega | \mathrm{tr}\, S_F(0,x)\gamma_4\gamma_5 S_F(x,0)\gamma_4\gamma_5 | \Omega \rangle \\ &= \frac{1}{N} \sum_{\{U\}} \mathrm{tr}\, S_F(0,x,[U])\gamma_4\gamma_5 S_F(x,0,[U])\gamma_4\gamma_5. \end{aligned} \tag{3.48}$$

Then by making use of the H discrete symmetry and properties of the γ matrices (see Appendix A)

$$\langle\Omega|A_4^\dagger(x)A_4(0)|\Omega\rangle = -\frac{1}{N}\sum_{\{U\}}\mathrm{tr}\Big\{S_F^\dagger(x,0,[U])\gamma_4 S_F(x,0,[U])\gamma_4\Big\} \tag{3.49}$$

where the trace is only over the colour indices, and on each configuration the fermion propagator is computed by inverting the fermion matrix (Eq. (3.43)) numerically.

4

Symanzik Improvement In The Static Quark Potential

4.1 Introduction

One of the signs of a confining theory is the fact that the potential energy between two charges ($Q\bar{Q}$) grows with an increase in separation. This leads to the idea of a "string" joining the two charges. In Lattice QCD, this is tested by calculating the expectation value of Wilson loops $\langle \mathcal{W} \rangle$. Of course, in full QCD the vacuum contains many $q\bar{q}$ loops so the linear rising of the potential is screened. The string between the $Q\bar{Q}$ breaks when the energy in the string is large enough to create an additional $q\bar{q}$ out of the vacuum and create two mesons. A signal that this has occured would be a flattening of the potential at some separation R. In quenched QCD however, sea quarks are given an infinite mass ($\det M = \text{constant}(= 1)$ in Eq. 3.40) and are thus suppressed. For this reason, it is not possible to see string breaking in quenched QCD.

While string breaking in the static quark potential between two infinitely heavy quarks in full dynamical-fermion QCD has long been predicted, direct observation of string breaking in lattice QCD is still a point of controversy [27–36]. The main reason for this appears to be due to difficulty in isolating the ground state of the static quark potential at large $q\bar{q}$ separations [33]. Overlap of standard operators for separating a static $q\bar{q}$ pair with excited states of the potential and close spacing in the spectrum of the potential at large separations demand significant Euclidean time evolution in order to isolate the ground state [33, 37, 38].

Accessing large Euclidean times is extremely difficult. APE smearing [39, 40] is widely recognized as an effective way to approach this region. The smearing of the spatial links of the lattice mocks up the flux tube joining two static quarks in the ground state potential. The smeared operator provides better overlap between the vacuum and the ground state potential and improves the signal to noise ratio in the correlation function [41].

As one approaches the large Euclidean space-time regime, statistical errors grow exponentially. While it is easy to fit the lattice data for the effective potential to a plateau ansatz, it is difficult to have confidence that the asymptotic value has been reached. With exponentially growing error bars, correlated χ^2 and goodness of fit parameters can provide a lower bound on the Euclidean time regime, but do not provide information on whether such a bound is sufficient to isolate the ground state potential.

Techniques for evaluating the extent to which the ground state dominates the Wilson loop are needed. Fortunately for the standard single-plaquette based Wilson gluon action, methods exist. However, these methods break down when improved actions are used.

Recently, novel ideas have been explored in the search for string breaking [33, 42–47]. While string breaking has been observed for some of these methods, string breaking using only Wilson loops is proving elusive [28, 36]. We are motivated by the encouraging results of Ref. [33–35] studying string breaking via Wilson loops in $2+1$ dimensional QCD. There, using improved actions on coarse lattices in three dimensions, string breaking was observed. These authors emphasize that Euclidean time evolution of the order of 1 fm is required to isolate the ground state potential. The efficiency afforded by the use of coarse lattices is argued to be key to achieving this goal.

Here we explore a systematic comparison of the static quark potential obtained from standard Wilson and Symanzik improved field configurations. Given the same number of configurations, similar lattice spacing and equivalent analysis techniques, we illustrate how the Standard Wilson action does as well as the Symanzik improved action in extracting the long-range $q\bar{q}$ potential. While the authors of Ref. [33] emphasize the efficiency of the improved action approach, we find that unimproved actions on reasonably coarse lattices offer the most efficient and suitably accurate use of limited computer resources.

Section 4.2 briefly explains our technique for calculating the static quark potential from Wilson loops. Here we present an alternative way of exploring the off-axis static quark potential. This new method provides additional information on the extent to which the ground-state potential dominates the Wilson loop and can provide confidence that sufficient evolution in Euclidean time has occurred. Section 4.3 outlines the details of the configurations used in the simulations. In Section 4.4, we present and discuss our results and in Section 4.5 we summarise.

4.2 The Static Quark Potential

The spectrum of the static quark potential is determined from Wilson loops $W(r,t)$ of area $r \times t$,

$$W(r,t) = \sum_i C_i(r)\, \exp(-V_i(r)\, t)\,. \tag{4.1}$$

In order to enhance $C_1(r)$, which measures the overlap of the loop with the ground state potential, the spatial links are APE smeared [39,40]. This smearing procedure replaces a spatial link $U_\mu(x)$, with a sum of the link and α times its spatial staples:

$$\begin{aligned} U_\mu(x) \rightarrow (1-\alpha)U_\mu \quad &+ \quad \frac{\alpha}{4}\sum_{\substack{\nu=1\\ \nu\neq\mu}}^{3} \Big[U_\nu(x)U_\mu(x+\nu a)U_\nu^\dagger(x+\mu a) \\ &+ \quad U_\nu^\dagger(x-\nu a)U_\mu(x-\nu a)U_\nu(x-\nu a+\mu a) \Big]\,. \end{aligned} \tag{4.2}$$

This is applied to all spatial links on the lattice followed by projection back to SU(3), and repeated n times.

Tuning the smearing parameters is key to the success of the approach. They govern both the Euclidean time extent of the Wilson loop correlation function and the relative contributions of ground to excited state contributions. It is vital to have a quantitative technique for tuning these parameters in order to optimise future studies of string breaking. The measure must be the extent to which the ground state dominates the correlation function.

Efficient methods exist for the unimproved Wilson action for fine tuning the smearing parameters to provide optimal overlap with the ground state potential. For $t = 0$, $W(r, t = 0) = 1$ providing the constraint $\sum_i C_i(r) = 1$ for a given r. For unimproved actions, where the transfer matrix is positive definite, each $C_i(r) \geq 0$. This means $C_1(r)$ can be monitored at large r but small t as the number of smearing sweeps are varied, with the optimal amount of smearing occurring when $C_1(r) \approx 1$. The proximity of $C_1(r)$ to 1 for small t may be easily estimated from the ratio

$$W^{t+1}(r,t)/W^{t}(r,t+1) \tag{4.3}$$

which equals $C_1(r)$ in the limit $C_1(r) \rightarrow 1$. This provides a quantitative measure of ground-state-dominance for unimproved Wilson actions. We note that it is sufficient [48] to fix the smearing fraction, α, and explore the parameter space via the number of smearing sweeps, n.

This procedure can be repeated for a number of alternate paths of links for a given separation r. By using variational techniques as described in Ref. [49], the combination of paths that gives the greatest overlap with the ground state can be found.

Actions improved in the time direction do not satisfy Osterwalder-Schrader [50] positivity [51]. This spoils the positive definite nature of the transfer matrix and the constraint $C_i(r) \geq 0$ is lost. Hence one needs either a new quantitative measure for evaluating ground-state-dominance, or to check the merits for using Symanzik improved gluon actions for the static quark potential at large r.

For exploratory purposes, we fixed $\alpha = 0.7$ and considered the values $n = 10$, 20, 30 and 40. The best results on a $16^3 \times 32$ lattice with lattice spacing ≈ 0.17 fm, are obtained using $\alpha = 0.7$ and $n = 10$ for the unimproved Wilson gauge action. This corresponds to a transverse RMS radius for the smeared links of 0.31 fm, where the transverse RMS radius after n sweeps is defined by

$$\langle r^2 \rangle_n = \frac{\sum_x x^2 \, V_n^2(x)}{\sum_x V_n^2(x)} \tag{4.4}$$

where

$$V_i(x') = \sum_x \left[(1-\alpha)\delta_{x'x} + \frac{\alpha}{4} \sum_{\mu=1}^{2} (\delta_{x',x+\mu} + \delta_{x',x-\mu}) \right] V_{i-1}(x)$$

and

$$V_0(x) = \begin{cases} 1 & x = 0 \\ 0 & x \neq 0 \end{cases} .$$

Analogous to the RMS smearing radius of Jacobi Fermion Source Smearing [52], this provides a reasonable estimate of the transverse smearing of mean field improved links ($U_\mu(x) \sim 1$).

Wilson loops, $W(r,t)$, or more precisely $W(x,y,z,t)$ where $r^2 = x^2 + y^2 + z^2$, are calculated both on-axis, along the Cartesian directions, and off-axis. On-axis Wilson loops are those that lie, e.g., in the $x - t$ plane only; off-axis loops begin, for example, by first stepping into the y or z (or both) directions before proceeding through the $x - t$ plane (Fig. 4.1). This provides an alternative to the usual method of calculating the off axis potential by building paths in three different directions using small elemental squares, rectangles or cubes (as in Fig. 4.2) and multiplying them together to form larger paths (see, for example, Ref. [53]). These standard techniques for calculating the off-axis potential may be combined with the approach described here using the variational method described extensively in Ref. [49].

Due to the periodicity of the lattice, the size of our Wilson loops are limited from 1 to a little over half the smallest lattice dimension in the on-axis directions

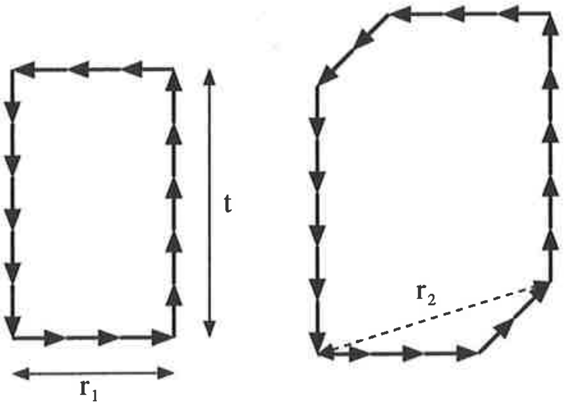

Figure 4.1: Construction of on-axis (left) and off-axis (right) Wilson loops using gauge links.

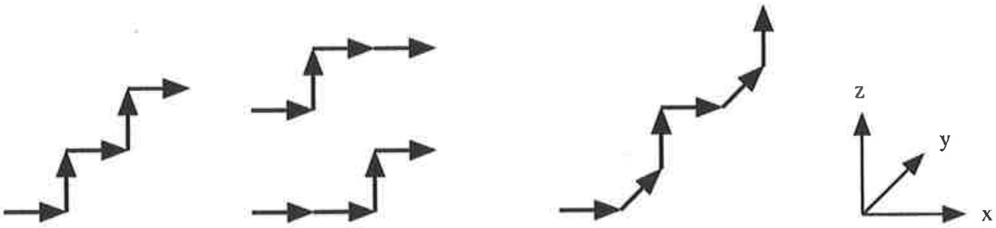

Figure 4.2: The usual method for constructing loops with separation (3,2,0) (left) and (2,2,2) (right) using the elementary building blocks (1,0,0), (1,1,0), (2,1,0), and (1,1,1)

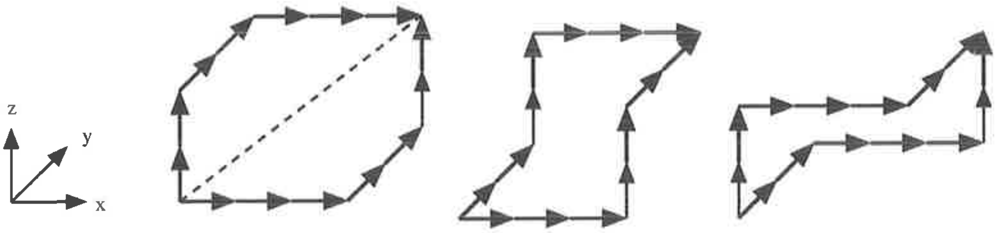

Figure 4.3: Six possible paths for a separation $\vec{r} = (3, 2, 2)$

and between 0 and 3 in the transverse directions. For example, for a $16^3 \times 32$ lattice, the sizes of the Wilson Loops, $t \times x \times y \times z$, vary from a $1 \times 1 \times 0 \times 0$ loop, to a $10 \times 10 \times 3 \times 3$ loop. Statistics are improved by transposing the loops over all points on the lattice and by rotating through the three spatial directions

In order to efficiently calculate Wilson loops of various sizes, including off-axis loops, we build products of links in each direction that we are considering for our Wilson loop. Link products extending from every lattice site are calculated in parallel. The loops are then formed in parallel by multiplying the appropriate sides together. Each side is created by reusing the components of the previous loop and one additional link. The same approach can be extended to loops that travel off-axis.

In an attempt to isolate the ground state potential for off-axis paths, one symmetrizes over the path of links connecting the off-axis heavy quark propagators, exploiting the full cubic symmetry of the lattice. For example, two points separated by n_x sites in the x-direction, n_y sites in the y-direction and n_z sites in the z-direction, may be connected by n_x link products in the x-direction, n_y link products in the y-direction and n_z link products in the z-direction which we denote by the triplet xyz. Instead of only calculating off-axis paths in the specific order xyz, we average over spatial paths calculated in the order $xyz, xzy, yxz, yzx, zxy, zyx$. Figure 4.3 shows the six possible paths for a separation $\vec{r} = (3, 2, 2)$. We calculated loops using this path-symmetrized technique as well as loops using a non-path-symmetrized operator where the order xyz alone is considered. The former form of operator is designed to suppress excited states by incorporating the full hyper-cubic symmetry of the lattice, whereas the latter operator is susceptible to excited state contamination. By comparing the static quark potential for these two operators, one can gain qualitative information on the effect of excited states in the static quark potential.

4.3 Numerical Simulations

Gauge configurations are generated with a mean-field improved, plaquette plus rectangle gluon action (Eq. (3.15)) using the Cabibbo-Marinari [54] pseudoheatbath algorithm with three diagonal $SU(2)$ subgroups. Simulations are performed using a parallel algorithm with appropriate link partitioning [55]. Configurations are generated on a $16^3 \times 32$ lattice at $\beta = 5.74$ using a standard Wilson action (Eq. (3.8)) which corresponds to a lattice spacing $a = 0.165(2)$ fm, and on a $16^3 \times 32$ lattice at $\beta = 4.38$ using the Symanzik improved action (Eq. 3.15) which also corresponds to a lattice spacing $a = 0.165(2)$ fm. Thus the two lattices have the same lattice spacing and physical volume.

Configurations are selected after 5000 thermalization sweeps from a cold start. The mean link, u_0, is averaged every 10 sweeps and updated during thermalization. For both the standard Wilson action and the Symanzik improved action, configurations are selected every 500 sweeps. The following analysis is based on an ensemble of 100 configurations for each action.

4.4 Simulation Results

The effective potential is obtained from

$$V_t(r) = \log\left(\frac{W(r,t)}{W(r,t+1)}\right), \tag{4.5}$$

which is expected to be independent of t for $t \gg 0$. Figure 4.4 displays the effective potential as a function of Euclidean time, t, obtained from 100 configurations generated via the Symanzik improved action at $\beta = 4.38$. For $r \geq 7$, we find that the signal is generally dominated by noise for $t > 4$, so we set the upper limit of our fitting range to $t_{\max} = 4$. The good plateau behavior at small Euclidean time is a reflection of the optimized smearing. Choosing the lower limit $t_{\min} = 1$ leads to large χ^2/d.o.f for large r. We fix the fitting range to be, in most cases, $t = 2$ to 4. The string tension is then extracted from the ansatz,

$$V(r) = V_0 + \sigma r - e/r \tag{4.6}$$

where $e = \pi/12$ [56], and V_0 and σ are fit parameters.

The values for $V(r) + e/r = \sigma r + V_0$ are then fitted to a line and the slope, σ, and intercept, V_0, are extracted. We fit the range $3 < r < 7$ such that we are not sensitive to the coulomb term and its associated dicretisation artifacts [57]. The error analysis is done using the Bootstrap method and all errors quoted are statistical only. Using $\sqrt{\sigma} = 440$ MeV to set the scale, the lattice spacings are determined.

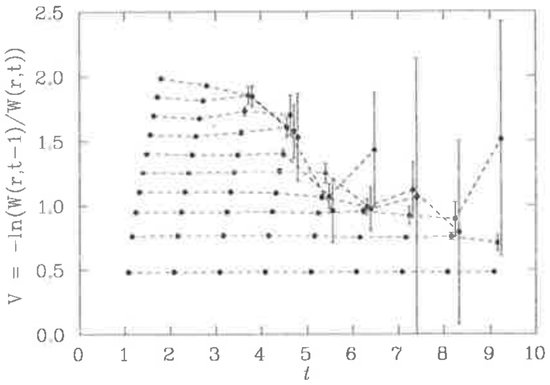

Figure 4.4: Euclidean time evolution of the effective potential. From bottom up, the "horizontal" lines correspond to $r = 1$ through 10. Here we use the Symanzik improved action with $\beta = 4.38$ and 10 sweeps of smearing at $\alpha = 0.7$. Axes are in lattice units. Points are offset to the right for clarity.

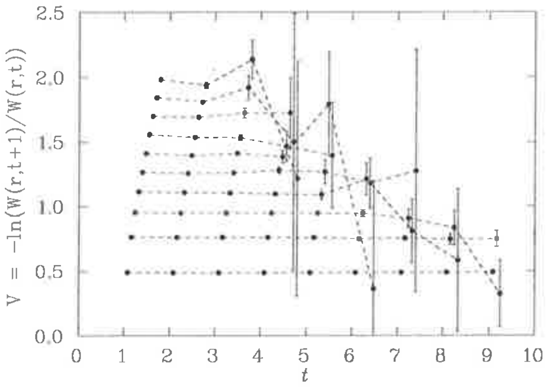

Figure 4.5: Euclidean time evolution of the effective potential. From bottom up, the "horizontal" lines correspond to $r = 1$ through 10. Here we use the standard unimproved Wilson action with $\beta = 5.74$ and 10 sweeps of smearing at $\alpha = 0.7$. Axes are in lattice units. Points are offset to the right for clarity.

4.4.1 Wilson Loop Correlation Function

To have any hope of seeing string breaking in QCD with dynamical fermions, the gauge links must first be smeared to improve the overlap of the ground state. The effects of smearing the spatial links (Eq. (4.2)) before calculating Wilson Loops is well known. Smearing provides access to the static quark potential at larger distances, providing a better chance of eventually being able to detect string breaking. Also, the lines with smeared links exhibit better plateau behavior in $V_t(r)$ than the unsmeared ones, indicating that we have better isolation of the ground state.

Figs. 4.4 and 4.5 illustrate the time dependence of Eq. 4.5 for Symanzik improved and standard Wilson gluon actions respectively. For clarity, we only plot values for r that are obtained from on-axis loops. For both the improved and unimproved actions, we see a clean signal up to $r \approx 8$ for the first three or four time slices. For r values greater than this, the quality of the statistical signal does not allow values of t larger than 2 or 3 to be included in the fits.

4.4.2 Off Axis Perturbations and Symmetry

Our method for stepping off-axis requires the use of a path-symmetrized operator. Fig. 4.6 displays results for the path-symmetrized operator for separating the $q\bar{q}$ pair, while Fig. 4.7 illustrates the non-path-symmetrized result. Both plots are obtained with 10 smearing sweeps at $\alpha = 0.7$. Banding is clearly evident in the non-path-symmetrized case but as soon as we path-symmetrize our operators, the banding largely disappears in off-axis points up to about $r = 7$. After $r = 7$, the banding still persists in off-axis points where loops of the form $r \times 1 \times 3$, $r \times 2 \times 3$ or $r \times 3 \times 3$ (where $r =$ on-axis step size and is greater than 7) are used. However the banding is negligible in off-axis points up to, and including, $r \times 2 \times 2$. Since our off-axis points are obtained by firstly stepping in one direction and then stepping in a different Cartesian direction, we are forming a right angle, not an approximate straight line. The fact that for $r < 7$, the $r \times 3 \times 3$ points lie on the line-of-best-fit is an interesting result and provides support for the use of this operator in a variational approach when searching for ground state dominance and its associated string breaking in full QCD. However, the persistence of banding at large r is an indicator that further Euclidean time evolution is required to isolate the ground state potential.

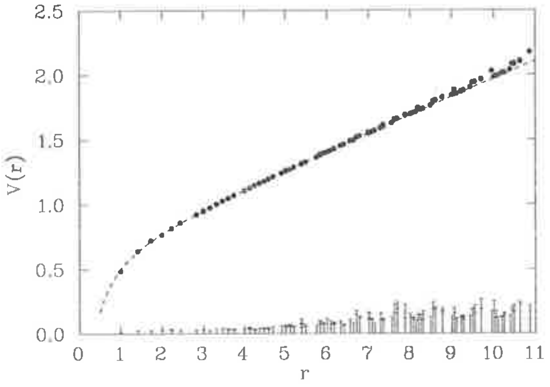

Figure 4.6: The static quark potential, $V(r)$, as a function of the separation r. Data is from the Symanzik improved action at $\beta = 4.38$ with 10 sweeps of smearing at $\alpha = 0.7$ and a path-symmetrized operator. Time slices $t = 1$ to 4 are used in the fit of the correlation function. Error bars are magnified by a factor of 20 and placed on the r-axis for clarity.

Figure 4.7: The static quark potential, $V(r)$, as a function of the separation r. Data is from the Symanzik improved action at $\beta = 4.38$ with 10 sweeps of smearing at $\alpha = 0.7$ and a non-path-symmetrized operator. Time slices $t = 1$ to 4 are used in the fit of the correlation function. Statistical error bars are too small to be seen.

4.4.3 Effect Of Using Symanzik Improved Gauge Field Configurations

Historically, the main feature of improved gauge field actions is the improved rotational symmetry [15]. This can be seen in our configurations by comparing Figs. 4.8 and 4.9. These graphs are enlargements of the small-r area. The off axis points for the Symanzik improved $\beta = 4.38$ lattices lie closer to the line of best fit through the Cartesian points, $r = 3$ to 7, than the unimproved Wilson $\beta = 5.74$ lattices.

However, here we are most interested in the large distance properties of the Wilson loop. To draw firm conclusions on the merits of using Symanzik improved actions in the search for string breaking, we create a matched set of standard Wilson gluon configurations, tuned to reproduce the string tension of the $\beta = 4.38$ improved configurations.

Figs. 4.6 and 4.10 compare Symanzik improved and unimproved Wilson results for $V(r)$ extracted from correlated fits within the range $1 \leq t \leq 4$. A similar comparison is made with Figs. 4.11 and 4.12 within the range $2 \leq t \leq 4$. Magnified error bars are plotted on the X-axis to allow a comparison of signal to noise between the two actions. Exponential growth in the error bars for large r is apparent in the fits with $2 \leq t \leq 4$.

It is crucial to compare matched lattices with the same lattice spacing and same physical volume. For example, a comparison of an unimproved Wilson lattice with $\beta = 5.70$ and lattice spacing $a = 0.181(2)$, with a Symanzik improved lattice at $\beta = 4.38$ and $a = 0.165(2)$ leads one to incorrectly conclude that Symanzik improved actions lead to an improvement in the signal-to-noise ratio of the static quark potential at large $q\bar{q}$ separations. The unimproved configurations with $\beta = 5.70$ lose the signal around $r/a = 7.5$ ($r = 1.37$ fm) when using time slices $t = 2 - 4$, whereas the improved configurations hold the signal up to $r/a = 9.5$ ($r = 1.59$ fm) when using $t = 2 - 4$. This effect is due to the slightly larger lattice spacing in the $\beta = 5.70$ simulations, which spoils the signal-to-noise ratio even after the larger lattice spacing is taken into account.

Close inspection of Figs. 4.10 and 4.12, where the Euclidean time regimes $1 \leq t \leq 4$ and $2 \leq t \leq 4$ are compared, reveals how the off-axis points can also be used to gain confidence in ground state dominance. In Fig. 4.10, banding is apparent. However, upon adjusting the Euclidean time regime for the fit to larger times in Fig. 4.12, the banding is largely removed.

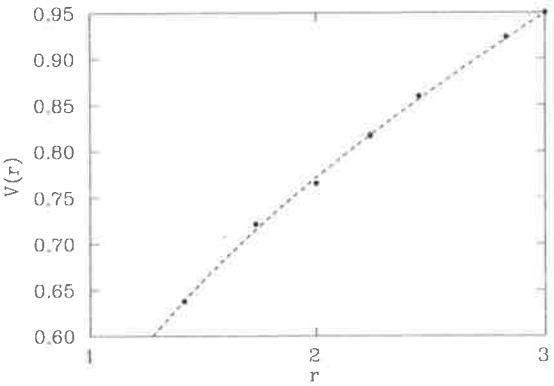

Figure 4.8: A close up of the static quark potential, $V(r)$, as a function of the separation r. Data is from the Symanzik improved action at $\beta = 4.38$ with 10 sweeps of smearing at $\alpha = 0.7$ and a path-symmetrized operator. Time slices $t = 2$ to 4 are used in the fit of the correlation function. The dashed line is a fit of Eq. 4.6 to on axis points $r = 3$ to 7.

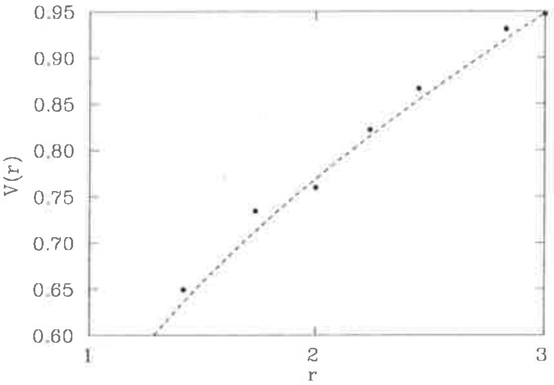

Figure 4.9: A close up of the static quark potential, $V(r)$, as a function of the separation r. Data is from the unimproved Wilson action at $\beta = 5.74$ with 10 sweeps of smearing at $\alpha = 0.7$ and a path-symmetrized operator. Time slices $t = 2$ to 4 are used in the fit of the correlation function. The dashed line is a fit of Eq. 4.6 to on axis points $r = 3$ to 7.

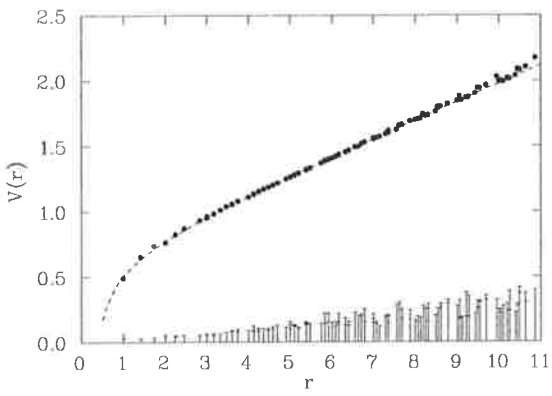

Figure 4.10: The static quark potential, $V(r)$, as a function of the separation r. Data is from the unimproved Wilson action at $\beta = 5.74$ with 10 sweeps of smearing at $\alpha = 0.7$ and a path-symmetrized operator. Time slices $t = 1$ to 4 are used in the fit of the correlation function. Error bars are magnified by a factor of 20 and placed on the r-axis for clarity.

4.5 Summary

We have calculated the static quark potential in quenched QCD using Symanzik improved and unimproved Wilson gluon actions. We have kept the lattice spacing and the physical volume of these lattices equal so that we can meaningfully compare the results. The number of gauge field configurations (100 here) is also held fixed for each action. We have explicitly shown that, despite the relatively coarse lattice spacing, the unimproved and computationally less expensive Wilson action does just as well as the improved action in extracting the $q\bar{q}$ potential at large separations. If one wishes to keep non-perturbative physics such as non-trivial topological fluctuations on the lattice, then one needs $a < 0.15$ fm [58], and thus $r/a > 7$ is required to reach the string breaking distance of about 1.1 fm [43]. In this case, the unimproved, standard Wilson gauge action is ideal for todays string breaking searches and computational resources can be redirected elsewhere. Another advantage for using unimproved Wilson gauge configurations is that we recover the extremely useful method for calculating the overlap with the ground state, $C_1(r)$, and thus tuning the smearing parameters.

We also explored the use of unconventional paths in accessing off-axis values of r in the static quark potential. These paths can provide insight into the

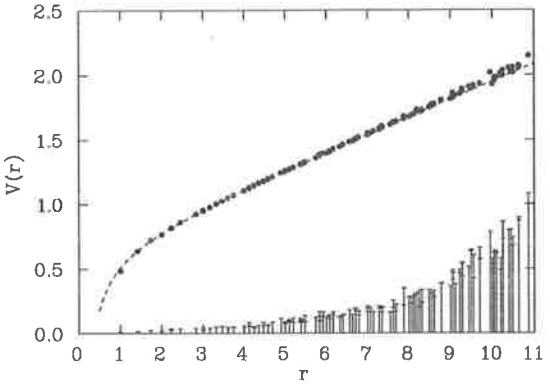

Figure 4.11: The static quark potential, $V(r)$, as a function of the separation r. Data is from the Symanzik improved action at $\beta = 4.38$ with 10 sweeps of smearing at $\alpha = 0.7$ and a path-symmetrized operator. Here time slices $t = 2$ to 4 are used in the fit of the correlation function. Error bars are magnified by a factor of 20 and placed on the r-axis for clarity.

extent to which the ground state potential dominates the Wilson loop at large Euclidean times. Provided the paths are symmetrized, these new paths provide useful information on the ground state potential and nearby excited potentials. Combined with standard paths and variational techniques, these paths offer additional promise for the search for string breaking in lattice QCD.

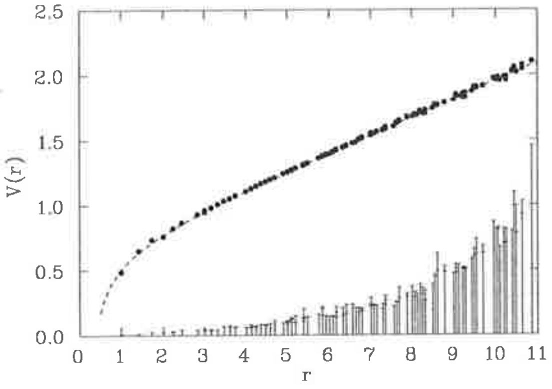

Figure 4.12: The static quark potential, $V(r)$, as a function of the separation r. Data is from the unimproved Wilson action at $\beta = 5.74$ with 10 sweeps of smearing at $\alpha = 0.7$ and a path-symmetrized operator. Time slices $t = 2$ to 4 are used in the fit of the correlation function. Error bars are magnified by a factor of 20 and placed on the r-axis for clarity.

5

Scale Determinations For An Improved Gluon Action

As we saw in the previous chapter, it is important to accurately set the physical scale of the lattice spacing so that quantities calculated on the lattice can be connected to the physical world. Every physical observable calculated on the lattice is dimensionless. For example, a lattice calculation of the nucleon mass is related to physical result and the lattice spacing by

$$M_N^{\text{lattice}} \equiv M_N^{\text{physical}}\, a,$$

where the lattice spacing is in units of (fm) and the physical mass in (GeV). In units where $\hbar c = 1$, 0.1973 GeV fm $= 1$.

A comprehensive study of the behaviour of the lattice spacing for the Wilson gauge action has been performed by Edwards *et al.* [57]. This type of study has yet to be done for the Symanzik improved gluon action defined in Eq. (3.15). This is the subject of this chapter.

5.1 Setting The Scale

We saw in the previous chapter that lattice data for the static quark potential can be fitted with the ansatz in Eq. (4.6). A more accurate ansatz has been suggested [57, 59] which makes a correction to the Coulomb term to account for the difference between the lattice one-gluon-exchange expression and the continuum version,

$$V(\mathbf{r}) = V_0 + \sigma r - e\left[\frac{1}{\mathbf{r}}\right] + l\left(\left[\frac{1}{\mathbf{r}}\right] - \frac{1}{r}\right). \tag{5.1}$$

Here $\left[\frac{1}{\mathbf{r}}\right]$ denotes the tree-level lattice Coulomb term

$$\left[\frac{1}{\mathbf{r}}\right] = 4\pi \int \frac{d^3\mathbf{k}}{(2\pi)^3} \cos(\mathbf{k}\cdot\mathbf{r}) D_{44}(0,\mathbf{k}), \tag{5.2}$$

and $D_{44}(k)$ is the time-time component of the gluon propagator. In the continuum limit, $\left[\frac{1}{\mathbf{r}}\right] \to \frac{1}{r}$.

As mentioned in Section 4.4, it is possible to fit the linear part of the static quark potential at large distances to extract the lattice string tension ($\sigma_L = a^2\sigma_p$) and by using the physical value, $\sqrt{\sigma_p} = 440$ MeV, the lattice spacing is determined.

A drawback to using the string tension to set the scale is that it is essential to have the potential at large $q\bar{q}$ separations, r, where errors are becoming large. Another problem with the string tension is that in full QCD, the string tension is not well-defined due to string breaking.

An alternative to this method was suggested by Sommer [60] who proposed an intermediate distance scale r_c via the force between a quark and an antiquark

$$r_c^2 V'(r_c) = r_c^2 F(r_c) = c \, , \tag{5.3}$$

for some real number c. A common choice takes $c = 1.65$ which corresponds to $r_c \approx r_0 = 0.5$ fm. At this distance, potentials can be accurately measured on the lattice. Another, less common, choice would be $c = 1$ and $r_1 = 0.35$ fm [61]. For coarser lattices, it is possible to use values of $r_c \approx 1$ fm [57].

Following the procedure outlined in Ref. [57], we fit Eq. (5.1) to the lattice data and obtain V_0, σ, e and l. By using

$$V_c(r) \equiv V_0 + \sigma r - e/r$$

as the continuum limit of Eq. (5.1), we can insert the derivative of this equation into Eq. (5.3) to obtain an ansatz for r_c,

$$r_c = \sqrt{\frac{c - e}{\sigma}} \tag{5.4}$$

5.2 Results

The simulations are performed on a variety of lattices with volumes $8^3 \times 16$, $10^3 \times 20$, $12^3 \times 24$, $16^3 \times 32$, $20^3 \times 40$, $24^3 \times 36$ and couplings in the range $3.75 \leq \beta \leq 5.0$. The full details of the lattices used are given in Table 5.1.

The procedure for calculating the static quark potential follows that given in Sections 4.2 and 4.4. Due to the increase in error at large distances and times, potentials calculated on coarse lattices must be fitted at early times and shorter distances. As an example, if the signal becomes noisy after $t = 4$ for a lattice with spacing 0.2 fm, then it is possible to only access information up to 0.8 fm. This means that for a lattice with a spacing 0.4 fm, only the first two timeslices are available for fits before the signal is lost. Where possible, the first time slice has been omitted from the fits so we have more confidence that the ground state potential is isolated. The calculated lattice spacings for each value of β are given in Table 5.1.

β	Volume	N_{configs}	$a\sqrt{\sigma}$	a_σ (fm)	r_0/a	u_0
3.75	$8^3 \times 16$	200	0.932(45)	0.418(20)		0.8195
3.92	$10^3 \times 20$	100	0.787(40)	0.353(18)		0.8329
4.10	$12^3 \times 24$	50	0.611(20)	0.272(9)	1.94(3)	0.8557
4.286	$8^3 \times 16$	50	0.423(28)	0.190(13)	2.63(4)	0.8721
4.38	$16^3 \times 32$	100	0.368(5)	0.165(3)	3.19(1)	0.8761
4.53	$20^3 \times 40$	33	0.299(11)	0.134(5)	3.90(12)	0.8859
4.60	$12^3 \times 24$	50	0.272(11)	0.122(5)	4.31(12)	0.8889
4.60	$16^3 \times 32$	50	0.272(11)	0.122(5)	4.31(12)	0.8889
4.80	$16^3 \times 32$	100	0.207(5)	0.093(2)	5.65(9)	0.8966
5.00	$24^3 \times 36$	10	0.172(15)	0.077(9)		0.9029

Table 5.1: Lattice spacings, β and volumes. The values for a_σ are set using $\sqrt{\sigma} = 440$ MeV. The scale for the small $\beta = 4.60$ lattice estimates are taken from the large $\beta = 4.60$ lattice

5.3 The Scaling Function

The two-loop scaling function of $SU(3)$ gauge theory [62] is given by

$$f(g^2) \equiv (b_0 g^2)^{-\frac{b_1}{2b_0^2}} \exp -\frac{1}{2b_0 g^2}, \quad b_0 = \frac{11}{(4\pi)^2}, \quad b_1 = \frac{102}{(4\pi)^4}. \tag{5.5}$$

The lattice spacing can be fitted using

$$a(g) = \frac{f(g^2)}{\Lambda}, \tag{5.6}$$

where Λ is a fit parameter

Since we are using a gauge action that is mean-field improved, for every value of $\beta = 6/g^2$ that we input into our simulations, there will be a corresponding mean-field improved version of beta, β_{IMP}, as seen by

$$S_{\text{Imp}} = \beta_0 \sum_{x,\mu>\nu} \left\{ \frac{5}{3}(1 - P_{\mu\nu}) - \frac{1}{12}(1 - \frac{R^{1\times2}_{\mu\nu}}{u_0^2}) + \frac{1}{12}(1 - \frac{R^{2\times1}_{\nu\mu}}{u_0^2}) \right\} \tag{5.7}$$

$$= \beta_0 u_0^4 \sum_{x,\mu>\nu} \left\{ \frac{5}{3}(1 - \frac{P_{\mu\nu}}{u_0^4}) - \frac{1}{12}(1 - \frac{R^{1\times2}_{\mu\nu}}{u_0^6}) + \frac{1}{12}(1 - \frac{R^{2\times1}_{\nu\mu}}{u_0^6}) \right\}$$

$$+ \text{ terms independent of the gauge fields} \tag{5.8}$$

and we define $\beta = \beta_{\text{IMP}} = \beta_0\, u_0^4$ in agreement with Eq. (3.15). As a consequence, the lattice spacing will scale via Eq. (5.5) best when $\beta_{\text{IMP}} = 6/g^2$ is used to define

g. We therefore calculate the tadpole improvement parameter via the plaquette measure of Eq. (3.14) and the values for each value of (input) β are given in Table 5.1. Fig. 5.1 shows the behaviour of β_{IMP} with β. We are then able to plot the lattice spacing obtained from the string tension as a function of β_{IMP} as shown in Fig. 5.2. We fit the data in Table 5.1 using Eq. (5.6) to obtain $\Lambda = 0.59$.

Using Figs. 5.2 and 5.1, it is now possible to work backwards and make an estimate for the value of β one should choose to achieve the desired lattice spacing.

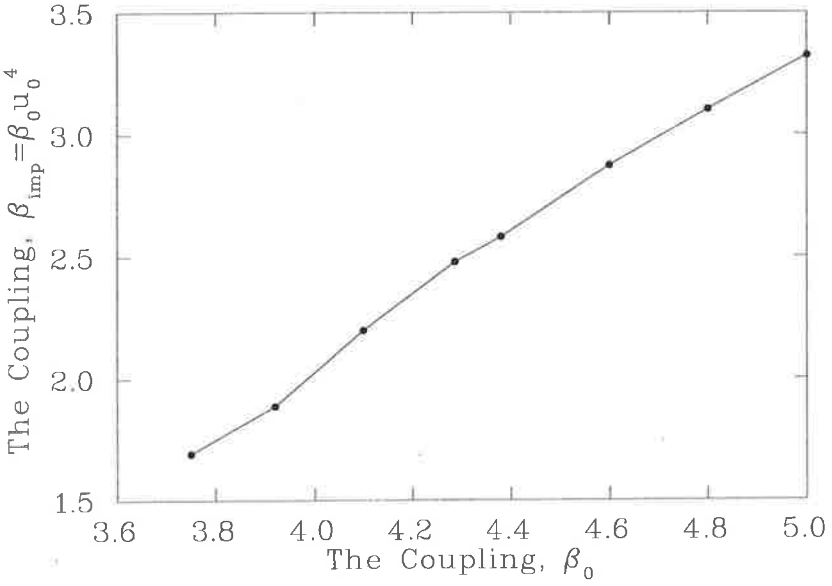

Figure 5.1: β_{imp} as a function β

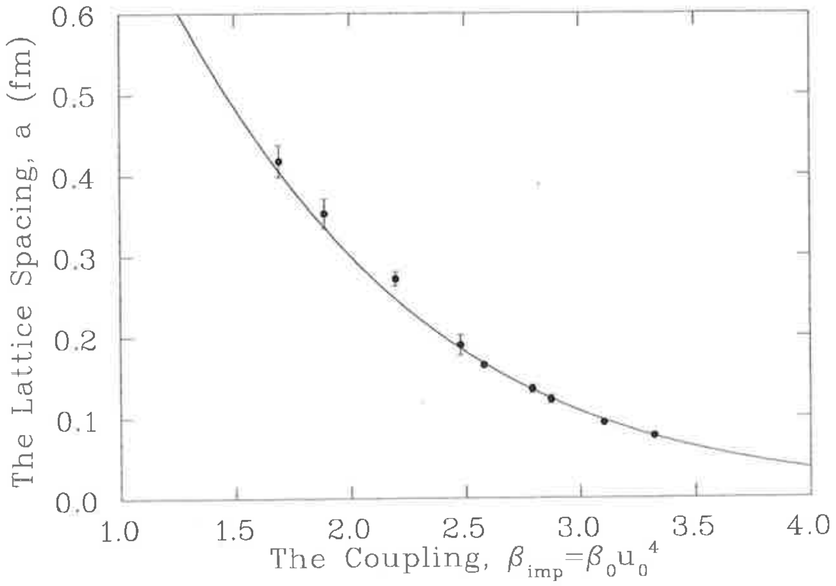

Figure 5.2: Data from Table 5.1 using $\sqrt{\sigma} = 440$ MeV. The solid line is a fit to our data using Eq. (5.6).

6

Fat-Link Irrelevant Clover Fermion Actions

6.1 Introduction

The origin of the masses of light hadrons represents one of the most fundamental challenges to QCD. Despite the universal acceptance of QCD as the basis from which to derive hadronic properties, there has been slow progress in understanding the generation of hadron mass from first principles. Solving the problem of the hadronic mass spectrum would allow considerable improvement in our understanding of the nonperturbative nature of QCD. The only available method at present to derive hadron masses directly from QCD is a numerical calculation on the lattice.

The high computational cost required to perform accurate lattice calculations at small lattice spacings has led to increased interest in quark action improvement. As mentioned in Section 3.3.3, the Sheikholeslami-Wohlert (clover) action [21] introduces an additional irrelevant dimension-five operator to the standard Wilson [11] quark action,

$$S_{\rm SW} = S_{\rm W} - \frac{iaC_{\rm SW}r}{4}\ \bar{\psi}(x)\sigma_{\mu\nu}F_{\mu\nu}\psi(x)\ , \tag{6.1}$$

where $S_{\rm W}$ is the standard Wilson action defined in Eq. (3.22) and $C_{\rm SW}$ is the clover coefficient which can be tuned to remove $\mathcal{O}(a)$ artifacts,

$$C_{\rm SW} \;=\; \left\{ \begin{array}{ll} 1 & \text{at tree-level}\ , \\ 1/u_0^3 & \text{mean-field improved}\ , \end{array} \right. \tag{6.2}$$

with u_0 the tadpole improvement factor (Eq. (3.14)) which corrects for the quantum renormalization of the operators. Nonperturbative (NP) $\mathcal{O}(a)$ improvement [22] tunes $C_{\rm SW}$ to all powers in g^2 and displays excellent scaling, as shown by Edwards *et al.* [63], who studied the scaling properties of the nucleon and vector meson masses for various lattice spacings (see also Section 6.4 below). In particular, the linear behavior of the NP-improved clover actions, when plotted against a^2, demonstrates that $\mathcal{O}(a)$ errors are removed. It was also found in Ref. [63] that a linear extrapolation of the mean-field improved data fails, indicating that $\mathcal{O}(a)$ errors are still present.

The established approach to nonperturbative (NP) improvement [22] tunes the coefficient of the clover operator to all powers in g^2. Unfortunately, this formulation of the clover action is susceptible to the problem of exceptional configurations as the quark mass becomes small. Chiral symmetry breaking in the clover fermion action introduces an additive mass renormalization into the Dirac operator that can give rise to singularities in quark propagators at small quark masses. In practice, this prevents the simulation of small quark masses and the use of coarse lattices ($\beta < 5.7 \sim a > 0.18$ fm) [64,65]. Furthermore, the plaquette version of $F_{\mu\nu}$ in Eq. (3.36), which is commonly used in Eq. (6.1), has large $\mathcal{O}(a^2)$ errors, which can lead to errors of the order of 10% in the topological charge even on very smooth configurations [48].

The idea of using fat links in fermion actions was first explored by the MIT group [66] and more recently has been studied by DeGrand *et al.* [64,67,68], who showed that the exceptional configuration problem can be overcome by using a fat-link (FL) clover action. Moreover, the renormalization of the coefficients of action improvement terms is small. In principle it is acceptable to smear the links of the relevant operators. The symmetry of the APE smearing process ensures that effects are $\mathcal{O}(a^2)$. The factors multiplying the link and staple ensure the leading order term is e^{iagA_μ}, an element of SU(3). Issues of projecting the smeared links to SU(3) are $\mathcal{O}(a^2)$ effects and therefore correspond to irrelevant operators [69]. However, the net effect of APE smearing the links of the relevant operators is to remove gluon interactions at the scale of the cutoff. While this has some tremendous benefits, the short-distance quark interactions are lost. As a result decay constants and vector-pseudoscalar mass splittings of heavy mesons, which are sensitive to the wave function at the origin, are suppressed [70].

A possible solution to this is to work with two sets of links in the fermion action. In the relevant dimension-four operators, one works with the untouched links generated via Monte Carlo methods, while the smeared fat links are introduced only in the higher dimension irrelevant operators. The effect this has on decay constants and vector-pseudoscalar mass splittings of heavy mesons is under investigation and will be reported elsewhere.

In this chapter we present results of simulations of the spectrum of light mesons and baryons using this variation on the clover action. In particular, we will start with the standard clover action and replace the links in the irrelevant operators with APE smeared [39, 40], or fat links. We shall refer to this action as the Fat-Link Irrelevant Clover (FLIC) action. Although the idea of using fat links only in the irrelevant operators of the fermion action was developed here independently, suggestions have appeared previously [71]. A published version of these results can be found in Ref. [72–74].

In Section 6.2 we describe the gauge configurations used in our lattice simulations, while Section 6.3 contains the procedure for creating the FLIC fermion action. The results of an investigation of the scaling of this action at finite lattice spacing are presented in Section 6.4. In Section 6.5 we investigate the problem of exceptional configurations by performing simulations of hadron masses at light quark masses corresponding to $m_\pi/m_\rho = 0.35$. Section 6.6 discusses the evidence for enhancement in octet-decuplet mass splittings as one approachs the chiral limit in the quenched approximation and finally in Section 6.7 we summarise the results.

6.2 The Gauge Action

The simulations are performed using a tree-level $\mathcal{O}(a^2)$–Symanzik-improved [16] gauge action on $12^3 \times 24$ and $16^3 \times 32$ lattices with lattice spacings of 0.093, 0.122 and 0.165 fm determined from the string tension with $\sqrt{\sigma} = 440$ MeV. Initial studies of FLIC, mean-field improved clover and Wilson quark actions were made using 50 configurations. The scaling analysis of FLIC fermions was performed with a total of 200 configurations at each lattice spacing and volume. In addition, for the light quark simulations, 94 configurations are used on a $20^3 \times 40$ lattice with $a = 0.134$ fm. Gauge configurations are generated using the Cabibbo-Marinari pseudoheat-bath algorithm with three diagonal SU(2) subgroups looped over twice. Simulations are performed using a parallel algorithm with appropriate link partitioning [55], and the error analysis is performed by a third-order, single-elimination jackknife, with the χ^2 per degree of freedom (N_{DF}) obtained via covariance matrix fits.

6.3 Fat-Link Irrelevant Fermion Action

Fat links [64, 67] are created by averaging or smearing links on the lattice with their nearest neighbours in a gauge covariant manner (APE smearing). The smearing procedure [39, 40] replaces a link, $U_\mu(x)$, with a sum of the link and α times its staples

$$\begin{aligned} U_\mu(x) \;\rightarrow\; U'_\mu(x) \;=\; (1-\alpha)U_\mu(x) + \frac{\alpha}{6}\sum_{\substack{\nu=1\\ \nu\neq\mu}}^{4} \Big[& U_\nu(x)U_\mu(x+\nu a)U_\nu^\dagger(x+\mu a) \\ & + U_\nu^\dagger(x-\nu a)U_\mu(x-\nu a)U_\nu(x-\nu a+\mu a)\Big] , \end{aligned} \quad (6.3)$$

followed by projection back to SU(3). We select the unitary matrix $U_\mu^{\rm FL}$ which maximizes

$$\mathcal{R}e\,{\rm tr}(U_\mu^{\rm FL}\,U_\mu'^\dagger)\,,$$

by iterating over the three diagonal SU(2) subgroups of SU(3). Performing eight iterations over these subgroups gives gauge invariance up to seven significant figures. We repeat the combined procedure of smearing and projection n times. We create our fat links by setting $\alpha = 0.7$ and comparing $n = 4$ and 12 smearing sweeps. The mean-field improved FLIC action now becomes

$$S_{\rm SW}^{\rm FL} = S_{\rm W}^{\rm FL} - \frac{iC_{\rm SW}\kappa r}{2(u_0^{\rm FL})^4}\,\bar\psi(x)\sigma_{\mu\nu}F_{\mu\nu}\psi(x)\,, \tag{6.4}$$

where $F_{\mu\nu}$ is constructed using fat links, $u_0^{\rm FL}$ is calculated in an analogous way to Eq. (3.14) with fat links, and where the mean-field improved Fat-Link Irrelevant Wilson action is

$$\begin{aligned} S_{\rm W}^{\rm FL} = \sum_x \bar\psi(x)\psi(x) \quad &+ \quad \kappa\sum_{x,\mu}\bar\psi(x)\Bigg[\gamma_\mu\bigg(\frac{U_\mu(x)}{u_0}\psi(x+\hat\mu) - \frac{U_\mu^\dagger(x-\hat\mu)}{u_0}\psi(x-\hat\mu)\bigg) \\ &- \quad r\bigg(\frac{U_\mu^{\rm FL}(x)}{u_0^{\rm FL}}\psi(x+\hat\mu) + \frac{U_\mu^{\rm FL\dagger}(x-\hat\mu)}{u_0^{\rm FL}}\psi(x-\hat\mu)\bigg)\Bigg]\,, \end{aligned} \tag{6.5}$$

with $\kappa = 1/(2m+8r)$. We take the standard value $r = 1$. Our notation uses the Pauli (Sakurai) representation of the Dirac γ-matrices defined in Appendix A. In particular, the γ-matrices are hermitian and $\sigma_{\mu\nu} = [\gamma_\mu,\ \gamma_\nu]/(2i)$.

As reported in Table 6.1, the mean-field improvement parameter for the fat links is very close to 1. Hence, the mean-field improved coefficient for $C_{\rm SW}$ is expected to be adequate[1]. In addition, actions with many irrelevant operators (*e.g.* the D$_{234}$ action) can now be handled with confidence as tree-level knowledge of the improvement coefficients should be sufficient. Another advantage is that one can now use highly improved definitions of $F_{\mu\nu}$ (involving terms up to u_0^{12}), which give impressive near-integer results for the topological charge [23]. A discussion of $F_{\mu\nu}$ improvement can be found in Appendix B.

In particular, we employ the 3-loop $\mathcal{O}(a^4)$-improved definition of $F_{\mu\nu}$ in which the standard clover-sum of four 1×1 loops lying in the μ,ν plane is combined with 2×2 and 3×3 loop clovers. Bilson-Thompson *et al.* [23] find

$$F_{\mu\nu} = \frac{-i}{8}\left[\left(\frac{3}{2}W_{\mu\nu}^{1\times1} - \frac{3}{20u_0^4}W_{\mu\nu}^{2\times2} + \frac{1}{90u_0^8}W_{\mu\nu}^{3\times3}\right) - {\rm h.c.}\right]_{\rm Traceless} \tag{6.6}$$

---

[1] Our experience with topological charge operators suggests that it is advantageous to include u_0 factors, even as they approach 1.

n	u_0^{FL}	$(u_0^{\mathrm{FL}})^4$
0	0.88894473	0.62445197
4	0.99658530	0.98641100
12	0.99927343	0.99709689

Table 6.1: The value of the mean link for different numbers of APE smearing sweeps, n, at $\alpha = 0.7$ on a $16^3 \times 32$ lattice at $\beta = 4.60$ which corresponds to a lattice spacing of 0.122 fm set by the string tension.

where $W^{n\times n}$ is the clover-sum of four $n \times n$ loops and $F_{\mu\nu}$ is made traceless by subtracting 1/3 of the trace from each diagonal element of the 3×3 color matrix. This definition reproduces the continuum limit with $\mathcal{O}(a^6)$ errors. On approximately self-dual configurations, this operator produces integer topological charge to better than 4 parts in 10^4. We also consider a 5-loop improved $F_{\mu\nu}$ for the $20^3 \times 40$ lattice at $\beta = 4.53$. Since the results for the 5-loop operator agree with the 3-loop version to better than 4 parts in 10^4 [23], we are effectively using the same action as far the scaling analysis is concerned.

Work by DeForcrand *et al.* [75] suggests that 7 cooling sweeps are required to approach topological charge within 1% of integer value. This is approximately 16 APE smearing sweeps at $\alpha = 0.7$ [58]. However, achieving integer topological charge is not necessary for the purposes of studying hadron masses, as has been well established. To reach integer topological charge, even with improved definitions of the topological charge operator, requires significant smoothing and associated loss of short-distance information. Instead, we regard this as an upper limit on the number of smearing sweeps.

Using unimproved gauge fields and an unimproved topological charge operator, Bonnet *et al.* [48] found that the topological charge settles down after about 10 sweeps of APE smearing at $\alpha = 0.7$. Consequently, we create fat links with APE smearing parameters $n = 12$ and $\alpha = 0.7$. This corresponds to ~ 2.5 times the smearing used in Refs. [64, 67]. Further investigation reveals that improved gauge fields with a small lattice spacing ($a = 0.122$ fm) are smooth after only 4 sweeps. Hence, we perform calculations with 4 sweeps of smearing at $\alpha = 0.7$ and consider $n = 12$ as a second reference. Table 6.1 lists the values of u_0^{FL} for $n = 0$, 4 and 12 smearing sweeps.

We also compare our results with the standard Mean-Field Improved Clover (MFIC) action. We mean-field improve as defined in Eqs. 6.4 and 6.5 but with thin links throughout. For this action, the standard 1-loop definition of $F_{\mu\nu}$ is used.

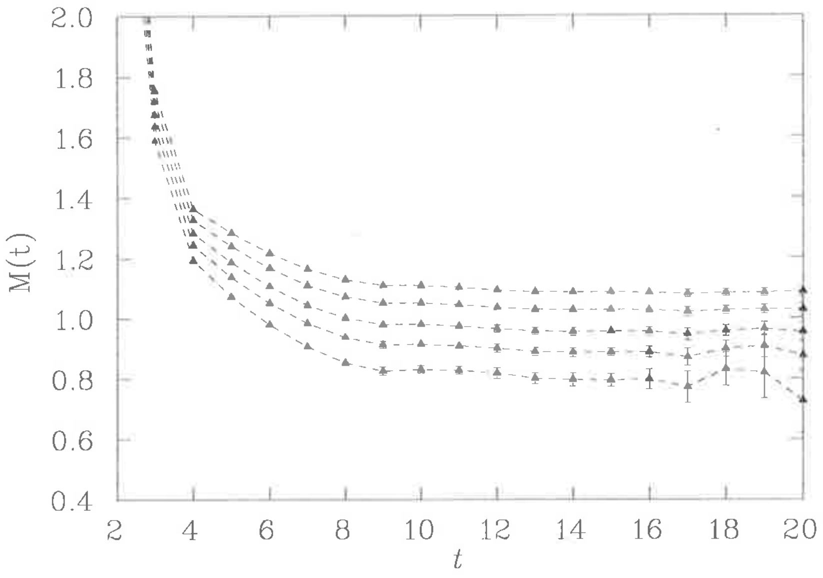

Figure 6.1: Effective mass plot for the nucleon for the FLIC action on a $16^3 \times 32$ lattice at $\beta = 4.60$ which corresponds to a lattice spacing of 0.122 fm set by the string tension. The fat links are created with 4 sweeps of smearing at $\alpha = 0.7$ from 200 configurations. The five sets of points correspond to the κ values listed in Table 6.2, with κ increasing from top down.

A fixed boundary condition is used for the fermions by setting

$$U_t(\vec{x}, nt) = 0 \qquad \text{and} \qquad U_t^{\mathrm{FL}}(\vec{x}, nt) = 0 \qquad \forall\, \vec{x} \tag{6.7}$$

in the hopping terms of the fermion action. The fermion source is centered at the space-time location $(x, y, z, t) = (1, 1, 1, 3)$, which allows for two steps backward in time without loss of signal, for all simulations except those on the $20^3 \times 40$ lattice at $\beta = 4.53$ which has the fermion source located at $(x, y, z, t) = (1, 1, 1, 8)$. Gauge-invariant gaussian smearing [76] in the spatial dimensions is applied at the source to increase the overlap of the interpolating operators with the ground states.

6.4 Scaling of FLIC Fermions

Hadron masses are extracted from the Euclidean time dependence of the calculated two-point correlation functions. Analogous to Eq. (3.44), for baryons the correlation functions are given by

$$G(t;\vec{p},\Gamma) = \sum_{x} e^{-i\vec{p}\cdot\vec{x}}\ \Gamma^{\beta\alpha}\langle\Omega|T[\chi^{\alpha}(x)\bar{\chi}^{\beta}(0)]|\Omega\rangle\ , \tag{6.8}$$

where χ are standard baryon interpolating fields, Ω represents the QCD vacuum, Γ is a 4×4 matrix in Dirac space, and α, β are Dirac indices. At large Euclidean times one has

$$G(t;\vec{p},\Gamma) \simeq \frac{Z^2}{2E_p}\ e^{-E_p t}\ \mathrm{tr}\left[\Gamma(-i\gamma\cdot p + M)\right]\ , \tag{6.9}$$

where Z represents the coupling strength of $\chi(0)$ to the baryon, and $E_p = (\vec{p}^2 + M^2)^{1/2}$ is the energy. Selecting $\vec{p} = 0$ and $\Gamma = (1 + \gamma_4)/4$, the effective baryon mass is then given by

$$M(t) = \log[G(t)] - \log[G(t+1)]\ . \tag{6.10}$$

Meson masses are determined via analogous standard procedures. The critical value of κ, $\kappa_{\rm cr}$, is determined by linearly extrapolating m_π^2 as a function of m_q to zero and the quark masses are defined by $m_q = (1/\kappa - 1/\kappa_{\rm cr})/(2a)$.

Figure 6.1 shows the nucleon effective mass plot for the FLIC action on a $16^3\times32$ lattice at $\beta = 4.60$ which corresponds to a lattice spacing of 0.122 fm set by the string tension. The fat links are created with 4 APE smearing sweeps at $\alpha = 0.7$ ("FLIC4"). The effective mass plots for the other hadrons are similar, and all display acceptable plateau behavior. Good values of $\chi^2/N_{\rm DF}$ are obtained for many different time-fitting intervals as long as one fits after time slice 8. All fits for this action are therefore performed on time slices 9 through 14. For the Wilson action and the FLIC action with $n = 12$ ("FLIC12"), the effective mass plots look similar to Fig. 6.1 and display good plateau behaviour. The fitting regimes used for these actions are 9-13 and 9-14, respectively.

The values of κ used in the simulations for all quark actions are given in Table 6.3. We have also provided the values of $\kappa_{\rm cr}$ for these fermion actions when using our mean-field improved, plaquette plus rectangle, gauge action at $\beta = 4.60$. We have mean-field improved our fermion actions so we expect the values for $\kappa_{\rm cr}$ to be close to the tree-level value of 0.125. Improved chiral properties are seen for the FLIC and MFIC actions, with FLIC4 performing better than FLIC12.

κ	$m_\pi\, a$	$m_\rho\, a$	$m_{\rm N}\, a$	$m_\Delta\, a$
0.1260	0.5797(23)	0.7278(39)	1.0995(58)	1.1869(104)
0.1266	0.5331(24)	0.6951(45)	1.0419(64)	1.1387(121)
0.1273	0.4744(27)	0.6565(54)	0.9709(72)	1.0816(152)
0.1279	0.4185(30)	0.6229(65)	0.9055(82)	1.0310(194)
0.1286	0.3429(37)	0.5843(97)	0.8220(102)	0.9703(286)

Table 6.2: Values of κ and the corresponding π, ρ, N and Δ masses for the FLIC action with 4 sweeps of smearing at $\alpha = 0.7$ on a $16^3 \times 32$ lattice at $\beta = 4.60$. The value for $\kappa_{\rm cr}$ is provided in Table 6.3. A string tension analysis incorporating the lattice coulomb term provides $a = 0.122(2)$ fm for $\sqrt{\sigma} = 440$ MeV.

	Wilson	FLIC12	FLIC4	MFIC
κ_1	0.1346	0.1286	0.1260	0.1196
κ_2	0.1353	0.1292	0.1266	0.1201
κ_3	0.1360	0.1299	0.1273	0.1206
κ_4	0.1367	0.1305	0.1279	0.1211
κ_5	0.1374	0.1312	0.1286	0.1216
$\kappa_{\rm cr}$	0.1390	0.1328	0.1300	0.1226

Table 6.3: Values of κ and $\kappa_{\rm cr}$ for the four different actions on a $16^3 \times 32$ lattice at $\beta = 4.60$ which corresponds to a lattice spacing of 0.122 fm set by the string tension.

The behavior of the ρ, nucleon and Δ masses as a function of squared pion mass are shown in Fig. 6.2 for the various actions. The first feature to note is the excellent agreement between the FLIC4 and FLIC12 actions. On the other hand, the Wilson action appears to lie somewhat low in comparison. It is also reassuring that all actions give the correct mass ordering in the spectrum. The value of the squared pion mass at $m_\pi/m_\rho = 0.7$ is plotted on the abscissa for the three actions as a reference point. This point is chosen in order to allow comparison of different results by interpolating them to a common value of $m_\pi/m_\rho = 0.7$, rather than extrapolating them to smaller quark masses, which is subject to larger systematic and statistical uncertainties.

The scaling behavior of the different actions is illustrated in Fig. 6.3. The present results for the Wilson action agree with those of Ref. [63]. The first feature to observe in Fig. 6.3 is that actions with fat-link irrelevant operators

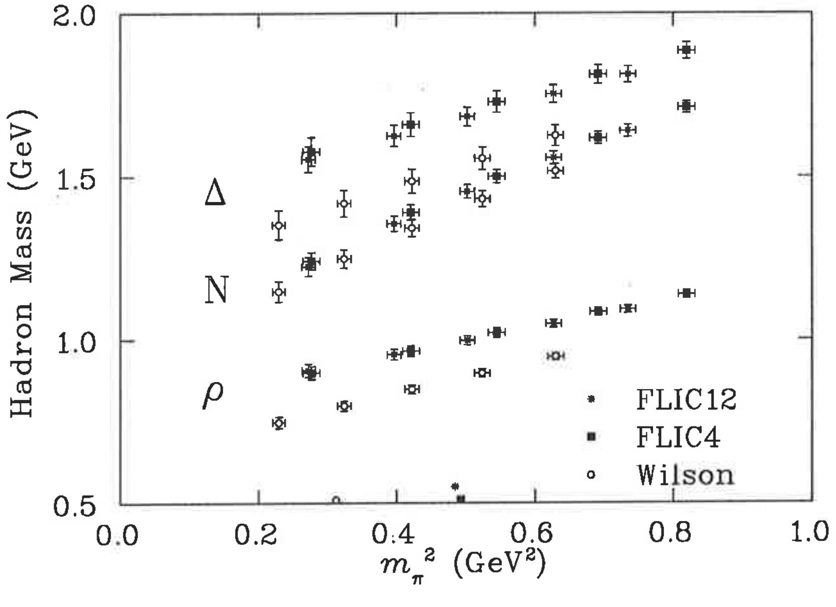

Figure 6.2: Masses of the nucleon, Δ and ρ meson versus m_π^2 for the FLIC4, FLIC12 and Wilson actions on a $16^3 \times 32$ lattice at $\beta = 4.60$ which corresponds to a lattice spacing of 0.122 fm set by the string tension.

perform extremely well. For both the vector meson and the nucleon, the FLIC actions perform significantly better than the mean-field improved clover action. It is also clear that the FLIC4 action performs systematically better than the FLIC12. This suggests that 12 smearing sweeps removes too much short-distance information from the gauge-field configurations. On the other hand, 4 sweeps of smearing combined with our $\mathcal{O}(a^4)$ improved $F_{\mu\nu}$ provides excellent results, without the fine tuning of $C_{\rm SW}$ in the NP improvement program.

Notice that for the ρ meson, a linear extrapolation of previous mean-field improved clover results in Fig. 6.3 passes through our mean-field improved clover result at $a^2\sigma \sim 0.075$ which lies systematically low relative to the FLIC actions. However, a linear extrapolation does not pass through the continuum limit result, thus confirming the presence of significant $\mathcal{O}(a)$ errors in the mean-field improved clover fermion action. While there are no NP-improved clover plus improved glue simulation results at $a^2\sigma \sim 0.075$, the simulation results that are

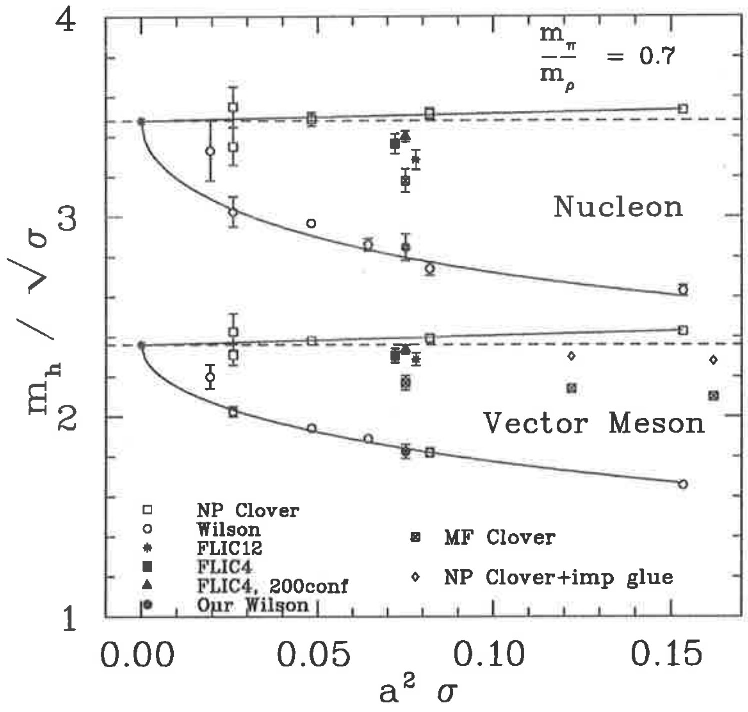

Figure 6.3: Nucleon and vector meson masses for the Wilson, NP-improved, mean-field clover and FLIC actions. Results from the present simulations, indicated by the solid points, are obtained by interpolating the results of Fig. 6.2 to $m_\pi/m_\rho = 0.7$. The fat links are constructed with $n = 4$ (solid squares) and $n = 12$ (stars) smearing sweeps at $\alpha = 0.7$. The solid triangles are results for the FLIC4 action when 200 configurations are used in the analysis. The FLIC results are offset from the central value for clarity. Our MF clover result at $a^2\sigma \sim 0.075$ lies systematically low relative to the FLIC actions.

available indicate that the fat-link results also compete well with those obtained with a NP-improved clover fermion action.

Having determined FLIC4 is the preferred action, we have increased the number of configurations to 200 for this action. As expected, the error bars are halved and the central values for the FLIC4 points move to the upper end of the error bars on the 50 configuration result, further supporting the promise of excellent scaling.

In order to further test the scaling of the FLIC action at different lattice spacings, we consider four different lattice spacings and three different volumes. The lattice spacings and volumes are given in Table 5.1 and the results are displayed in Fig. 6.4. The two different volumes used at $a^2\sigma \sim 0.075$ indicate a small finite volume effect, which increases the mass for the smaller volume at $a^2\sigma \sim 0.075$ and ~ 0.045. Examination of points from the small and large volumes separately indicates continued scaling toward the continuum limit. While the finite volume effect will produce a different continuum limit value, the slope of the points from the smaller and larger volumes agree, consistent with errors of $\mathcal{O}(a^2)$.

Focusing on simulation results from physical volumes with extents ~ 2 fm and larger, we perform a simultaneous fit of the FLIC, NP-improved clover and Wilson fermion action results. The fits are constrained to have a common continuum limit and assume errors are $\mathcal{O}(a^2)$ for FLIC and NP-improved clover actions and $\mathcal{O}(a)$ for the Wilson action. An acceptable χ^2 per degree of freedom is obtained for both the nucleon and ρ-meson fits. These results indicate that FLIC fermions provide a new form of nonperturbative $\mathcal{O}(a)$ improvement. The FLIC fermion results display nearly perfect scaling indicating $\mathcal{O}(a^2)$ errors are small for this action.

6.5 Search For Exceptional Configurations

Chiral symmetry breaking in the Wilson action allows continuum zero modes of the Dirac operator to be shifted into the negative mass region. This problem is accentuated as the gauge fields become rough ($a \longrightarrow$ large). Local lattice artefacts at the scale of the cutoff (often referred to as dislocations) give rise to spurious near zero modes. The quark propagator can then encounter singular behaviour as the quark mass becomes light.

Exceptional configurations are a severe problem in quenched QCD (QQCD) because instantons are low action field configurations which appear readily in QQCD. These instanton configurations give rise to approximate zero modes which should be suppressed at light quark masses by $\det M$ in Eq. (3.39) which

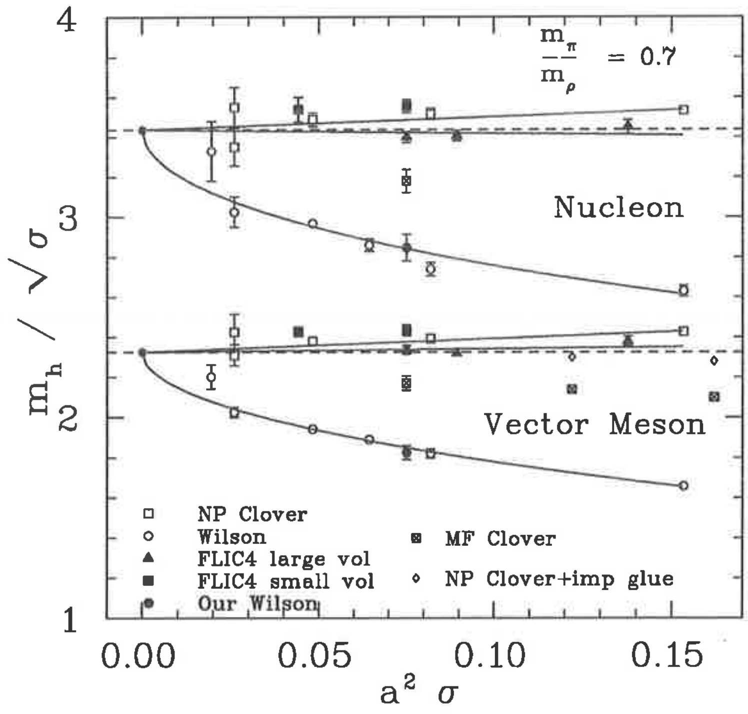

Figure 6.4: Nucleon and vector meson masses for the Wilson, Mean-Field (MF) improved, NP-improved clover and FLIC actions obtained by interpolating simulation results to $m_\pi/m_\rho = 0.7$. For the FLIC action ("FLIC4"), fat links are constructed with $n = 4$ APE-smearing sweeps with smearing fraction $\alpha = 0.7$, except for the point at $a^2\sigma \sim 0.09$ which has $n = 6$. Results from the current simulations are indicated by the solid symbols; those from earlier simulations by open or hatched symbols. The solid-lines illustrate fits, constrained to have a common continuum limit, to FLIC, NP-improved clover and Wilson fermion action results obtained on physically large lattice volumes.

is present in the link updates in full QCD. This determinant is not present in QQCD and as a result, near-zero modes are overestimated in the ensemble.

The addition of the clover term to the fermion action broadens the distribution of near-zero modes. As a result, the clover action is notorious for revealing the exceptional configuration problem in QQCD. The FLIC action hopes to reduce the number of exceptional configurations by smoothing the gauge fields of the irrelevant operator via APE smearing [39, 40]. The smoothing procedure has the effect of suppressing the local lattice artifacts and narrowing the distribution of near-zero modes, enabling simulations to be performed at light quark masses not currently accessible with the standard mean-field or non-perturbative improved clover fermion actions.

In order to access the light quark regime, we would like our preferred action to be efficient when inverting the fermion matrix. Fig. 6.5 compares the convergence rates of the different actions on a $16^3 \times 32$ lattice at $\beta = 4.60$ by plotting the number of stabilized biconjugate gradient [77] iterations required to invert the fermion matrix as a function of m_π/m_ρ. For any particular value of m_π/m_ρ, the FLIC actions converge faster than both the Wilson and mean-field improved clover fermion actions. Also, the slopes of the FLIC lines are smaller in magnitude than those for Wilson and mean-field improved clover actions, which provides great promise for performing cost effective simulations at quark masses closer to the physical values. Problems with exceptional configurations have prevented such simulations in the past.

The ease with which one can invert the fermion matrix using FLIC fermions (also see Ref [78]) leads us to attempt simulations down to light quark masses corresponding to $m_\pi/m_\rho = 0.35$. Previous attempts with Wilson-style fermion actions on configurations with lattice spacing ≥ 0.1 fm have only succeeded in getting down to $m_\pi/m_\rho = 0.47$ [79]. In order to search for exceptional configurations, we follow the technique used by Della Morte *et al.* [79] and note that in the absence of exceptional configurations, the standard deviation of an observable will be independent of the number of configurations considered in the average. Exceptional configurations reveal themselves by introducing a significant jump in the standard deviation as the configuration is introduced into the average. In severe cases, exceptional configurations can lead to divergences in correlation functions or prevent the matrix inversion process from converging.

The simulations are on a $20^3 \times 40$ lattice with a lattice spacing of 0.134 fm set by the string tension which corresponds to a physical length $\sim$ 2.7 fm. We have used an initial set of 100 configurations, using $n = 6$ sweeps of APE-smearing and a five-loop improved lattice field-strength tensor. Fig. 6.6 shows the standard deviation of the pion mass for eight quark masses on subsets of 30 (consecutive) configurations with a cyclic property enforced from configuration

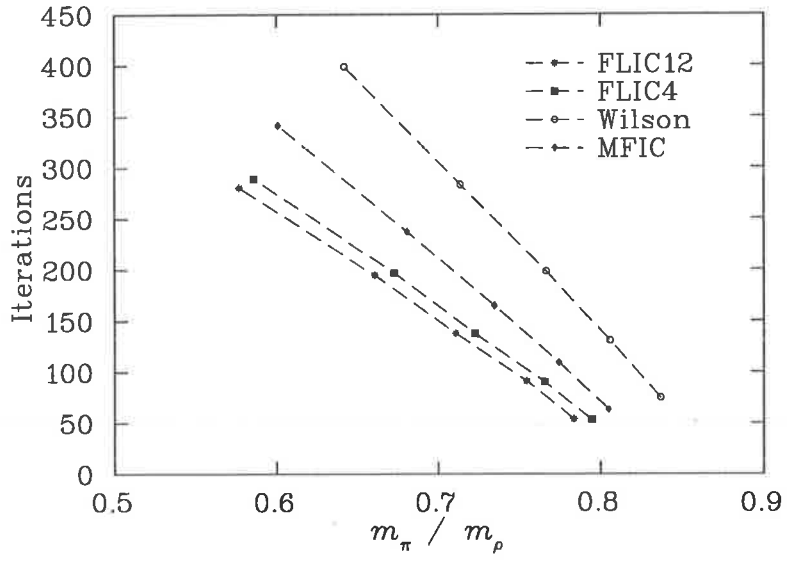

Figure 6.5: Average number of stabilized biconjugate gradient iterations for the Wilson, FLIC and mean-field improved clover (MFIC) actions plotted against m_π/m_ρ. The fat links are constructed with $n = 4$ (solid squares) and $n = 12$ (stars) smearing sweeps at $\alpha = 0.7$ on a $16^3 \times 32$ lattice at $\beta = 4.60$ which corresponds to a lattice spacing of 0.122 fm set by the string tension.

100 to configuration 1. At first glance, it is obvious that the error blows up for several quark masses at $N = 12$ and drops again at $N = 41$. As configurations 12 through 41 are included in the average at $N = 12$, this indicates that configuration number 41 is a candidate for an exceptional configuration. An inspection of the pion mass in Fig. 6.7 shows that the pion mass for the third lightest quark mass decreases significantly more than the second or fourth lightest quark masses. This indicates that $\kappa_{\rm cr}$ for this configuration lies somewhere between κ_6 and κ_7. A solution to this problem would be to use the the modified quenched approximation (MQM) from Ref. [65] and move $\kappa_{\rm cr}$ on this configuration back to the ensemble average for $\kappa_{\rm cr}$. However, since the movement of $\kappa_{\rm cr}$ is largely a quenched artifact and would be suppressed in a full QCD simulation we prefer to simply identify and remove such configurations from the ensemble. Obviously, if we find that a signicant percentage of our configurations are having trouble at a particular quark mass, then it would make no sense to proceed with

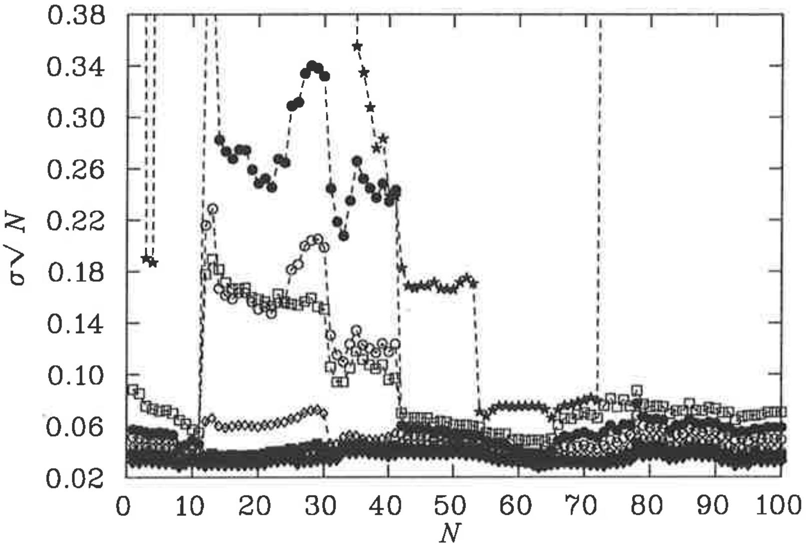

Figure 6.6: The standard deviation in the error of the π mass calculated on 30 configurations plotted against the starting configuration number for the FLIC-fermion action on a $20^3 \times 40$ lattice with $a = 0.134$ fm.

the simulation. We would then have to conclude that we have reached the light quark mass limit of our action and simply step back to the next lightest mass.

Now let us return to Fig. 6.6. In addition to the highly exceptional configuration number 41, we also notice a large increase in error in the lightest quark mass for configuration numbers 2, 13, 30, 34 and 53. Upon removal of these configurations, we see in Fig. 6.8 a near-constant behaviour of the standard deviation for the remaining configurations. This means that our elimination rate for our FLIC6 action on a lattice with a spacing 0.134 fm is about 6%. So for the 100 configurations used in this analysis, we are able to use 94 of them to extract hadron masses.

6.6 Octet-Decuplet Mass Splittings

Figure 6.9 shows the N and Δ masses as a function of m_π^2 for the FLIC-fermion action on a $20^3 \times 40$ lattice with $a = 0.132$ fm (which corresponds to a string

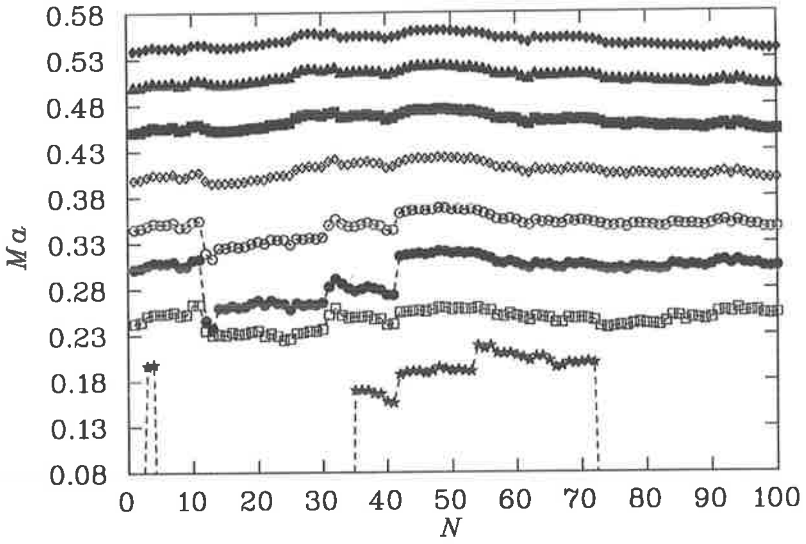

Figure 6.7: The π mass calculated on 30 configurations plotted against the starting configuration number for the FLIC-fermion action on a $20^3 \times 40$ lattice with $a = 0.134$ fm.

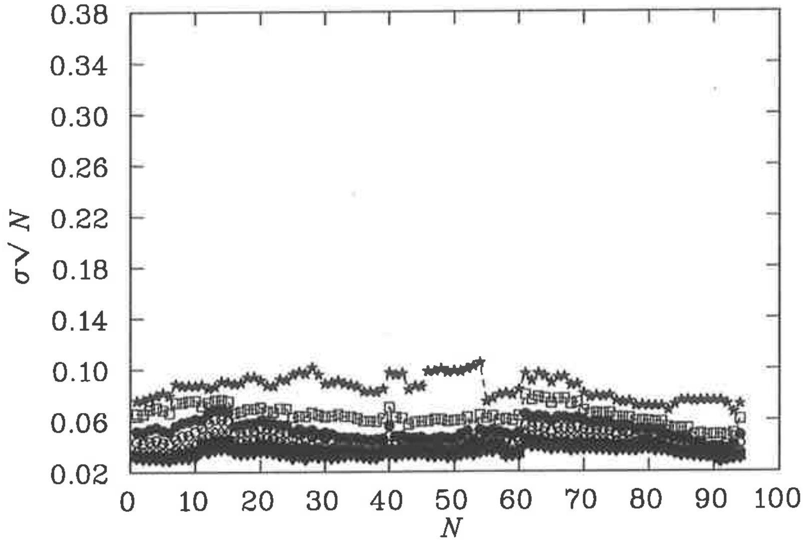

Figure 6.8: The standard deviation in the error of the π mass calculated on 30 configurations plotted against the starting configuration number for the FLIC-fermion action on a $20^3 \times 40$ lattice with $a = 0.134$ fm. Configuration numbers 2, 13, 30, 34, 41 and 53 have been omitted.

κ	$m_\pi\, a$	$m_\rho\, a$	$m_{\rm N}\, a$	$m_\Delta\, a$
0.1278	0.5400(30)	0.7304(55)	1.0971(80)	1.2238(98)
0.1283	0.4998(31)	0.7053(58)	1.0522(84)	1.1899(102)
0.12885	0.4521(34)	0.6774(63)	1,0006(91)	1.1528(108)
0.1294	0.3990(38)	0.6491(72)	0.9465(101)	1.1162(115)
0.1299	0.3434(43)	0.6228(87)	0.8944(116)	1.0841(125)
0.13025	0.2978(47)	0.6040(107)	0.8562(134)	1.0630(135)
0.1306	0.2419(54)	0.5845(143)	0.8172(171)	1.0443(154)
0.1308	0.1972(69)	0.5812(213)	0.7950(215)	1.0380(189)

Table 6.4: Values of κ and the corresponding π, ρ, N and Δ masses for the FLIC action with 6 sweeps of smearing at $\alpha = 0.7$. A string tension analysis provides $a = 0.134(2)$ fm for $\sqrt{\sigma} = 440$ MeV.

tension scale with $\sqrt{\sigma} = 450$ MeV) such that the nucleon extrapolation passes through the physical value for clarity. An upward curvature in the Δ mass for decreasing quark mass is observed in the FLIC fermion results. This behavior, increasing the quenched $N - \Delta$ mass spitting, was predicted by Young *et al.* [80] using quenched chiral perturbation theory (QχPT) formulated with a finite-range regulator. A finite-regulated QχPT fit to the FLIC-fermion results is illustrated by the solid curves. The dashed curves estimate the correction that will arise in unquenching the lattice QCD simulations [80]. We note that after we have corrected for the absence of sea quark loops, our results agree simultaneously with the physical values for both the nucleon and Δ.

We also calculate the light quark mass behaviour of the octet and decuplet hyperons. The strange quark mass is chosen in order to reproduce the physical strange quark mass according to the phenomenological value of an $s\bar{s}$ pseudoscalar meson,

$$m_{ss}^2 = 2m_K^2 - m_\pi^2. \tag{6.11}$$

Upon substitution of the physical masses for the π and K mesons, this corresponds to an $s\bar{s}$ pseudoscalar meson mass of ~ 0.470 GeV^2 which occurs at our third heaviest quark mass. The form of our interpolating fields that we use to excite these states from the QCD vacuum are discussed in detail in Section 7.3. The results from this calculation are given in Table 6.5 and are illustrated in Fig. 6.10. The results show the correct ordering and in particular, we notice a mass splitting between the *strangeness* $= -1$ ($I = 1$) Σ and ($I = 0$) Λ baryons becoming evident in the light quark mass regime.

Just as we saw the non-analytic behavior of quenched chiral perturbation the-

κ	$m_\Lambda\, a$	$m_\Sigma\, a$	$m_\Xi\, a$	$m_{\Sigma*}\, a$	$m_{\Xi*}\, a$
0.1278	1.0696(84)	1.0616(83)	1.0381(87)	1.2002(101)	1.1765(104)
0.1283	1.0376(86)	1.0328(86)	1.0206(88)	1.1776(104)	1.1652(106)
0.12885	1.0006(91)	1.0006(91)	1,0006(91)	1.1528(108)	1.1528(108)
0.1294	0.9615(97)	0.9680(97)	0.9799(94)	1.1284(113)	1.1406(110)
0.1299	0.9235(106)	0.9383(106)	0.9603(98)	1.1070(118)	1.1299(113)
0.13025	0.8955(117)	0.9178(116)	0.9462(102)	1.0930(124)	1.1229(115)
0.1306	0.8667(137)	0.8980(132)	0.9323(109)	1.0806(132)	1.1166(118)
0.1308	0.8544(154)	0.8919(152)	0.9254(114)	1.0772(142)	1.1145(120)

Table 6.5: Values of the octet Λ, Σ, Ξ and decuplet Σ^*, Ξ^* masses for each value of κ for the FLIC action with 6 sweeps of smearing at $\alpha = 0.7$. A string tension analysis provides $a = 0.134(2)$ fm for $\sqrt{\sigma} = 440$ MeV.

ory in the Δ-baryon mass in Fig. 6.9 leading to an enhancement of the quenched $N - \Delta$ mass spitting, Fig. 6.11 shows a similar enhancement for the decuplet-octet mass splittings in Σ and Ξ baryons respectively. In Section 2.5 and in particular Eq. (2.7), we saw that the quark model predicts that the hyperfine splittings should approximately satisfy

$$\Xi_s^* - \Xi_s = \Sigma_s^* - \Sigma_s .$$

Fig. 6.12 shows that even though the quenched approximation enhances the splitting between octet and decuplet baryons, the splittings for the Σ and Ξ baryons still satisfy Eq. (2.7).

If we consider a naive extrapolation of the points in Fig. 6.12, we might expect the results to produce the following mass splittings in the chiral limit

$$\begin{aligned} \Delta - N &\approx 400\,\text{MeV} \\ \Sigma_s^* - \Sigma_s &\approx \Xi_s^* - \Xi_s \approx 290\,\text{MeV}, \end{aligned}$$

which gives a ratio

$$\frac{\Sigma_s^* - \Sigma_s}{\Delta - N} = \frac{\Xi_s^* - \Xi_s}{\Delta - N} = 0.725 \,, \qquad (6.12)$$

so we see that inspite of the enhanced mass splitting between octet and decuplet baryons in quenched QCD, the ratio of the splittings agree well with the experimental ratios in Eq. (2.10) and with the quark model prediction in Eq. (2.9). The value obtained from the QQCD simulations agrees extremelly well with the experimental result involving the Ξ baryons and reasonably well with the prediction of the quark model. Agreement of the quenched QCD results with the quark model prediction is not, perhaps, suprising since both have a suppressed meson cloud. Similarly, one expects a suppression of the meson cloud when two (heavy) strange quarks are present in a baryon.

6.7 Summary

In this chapter, we have found that minimal smearing provides better scaling behavior. Our results suggest that too much smearing removes relevant information from the gauge fields, leading to a poorer performance.

We have calculated hadron masses to test the scaling of the Fat-Link Irrelevant Clover fermion action, in which only the irrelevant, higher-dimension operators involve smeared links. One of the main conclusions of this work is that the use of fat links in the irrelevant operators provides a new form of nonperturbative $\mathcal{O}(a)$ improvement. This technique competes well with $\mathcal{O}(a)$ nonperturbative improvement on mean field-improved gluon configurations, with the advantage of a reduced exceptional configuration problem.

Quenched simulations at quark masses down to $m_\pi/m_\rho = 0.35$ have been successfully performed on a $20^3 \times 40$ lattice with a lattice spacing of 0.134 fm on 94 out of 100 configurations. Simulations at such light quark masses reveal non-analytic behaviour of quenched chiral perturbation theory and provides for an interesting analysis of the hyperfine splitting between octet and decuplet baryons.

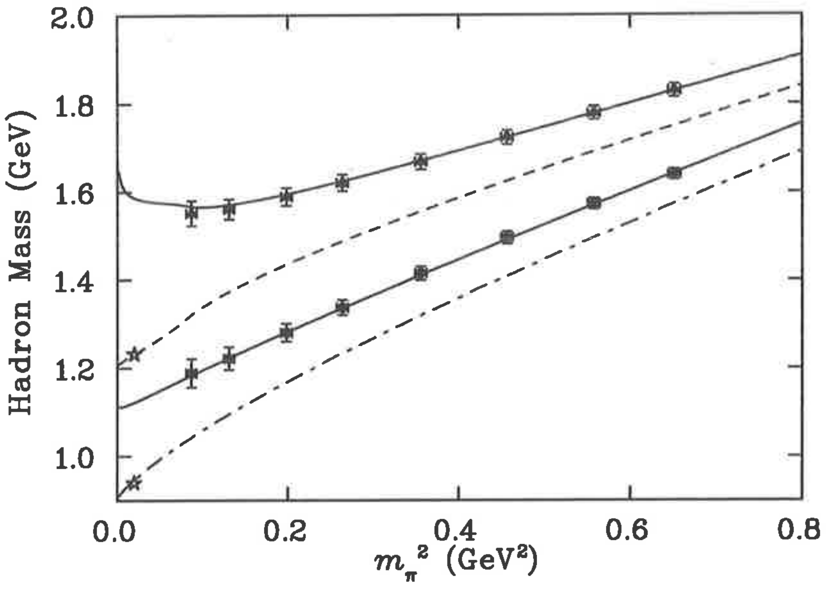

Figure 6.9: Nucleon and Δ masses for the FLIC-fermion action on a $20^3 \times 40$ lattice. Here we select $a = 0.132$ fm (which corresponds to the string tension with $\sqrt{\sigma} = 450$ MeV) such that the nucleon extrapolation passes through the physical value for clarity. The solid curves illustrate fits of quenched chiral perturbation theory using a finite regulator to the lattice QCD results. The dashed curves estimate the correction that will arise in unquenching the lattice QCD simulations. Stars at the physical pion mass denote experimentally measured values.

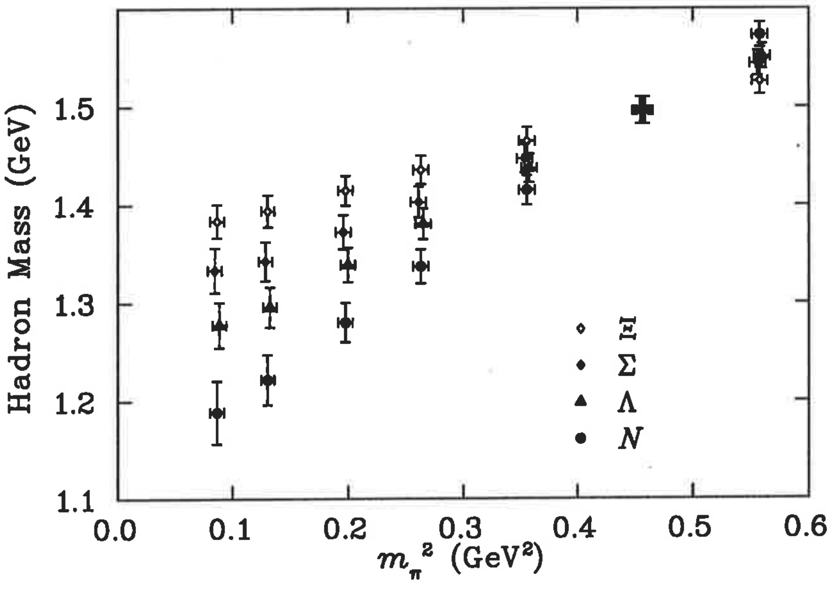

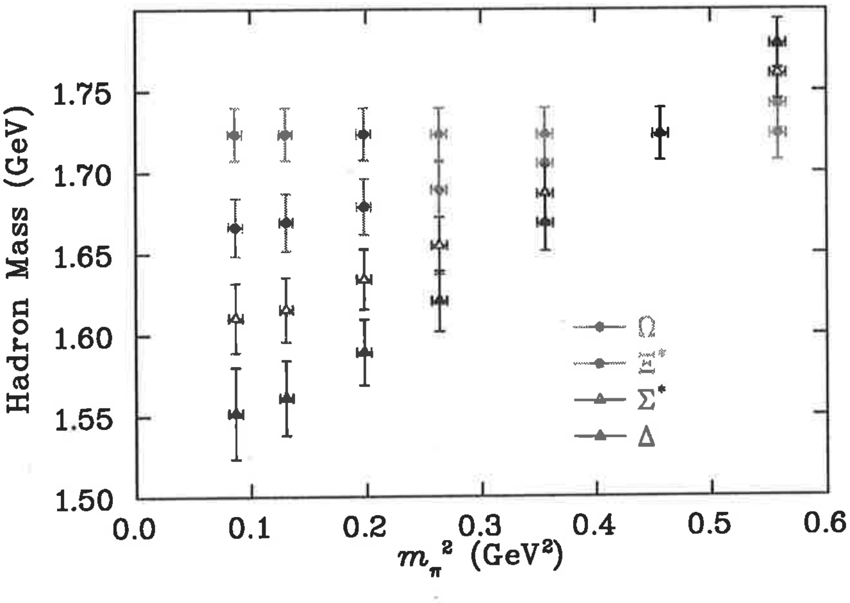

Figure 6.10: Octet (top) and decuplet (bottom) baryon masses for the FLIC-fermion action on a $20^3 \times 40$ lattice with $a = 0.132$ fm.

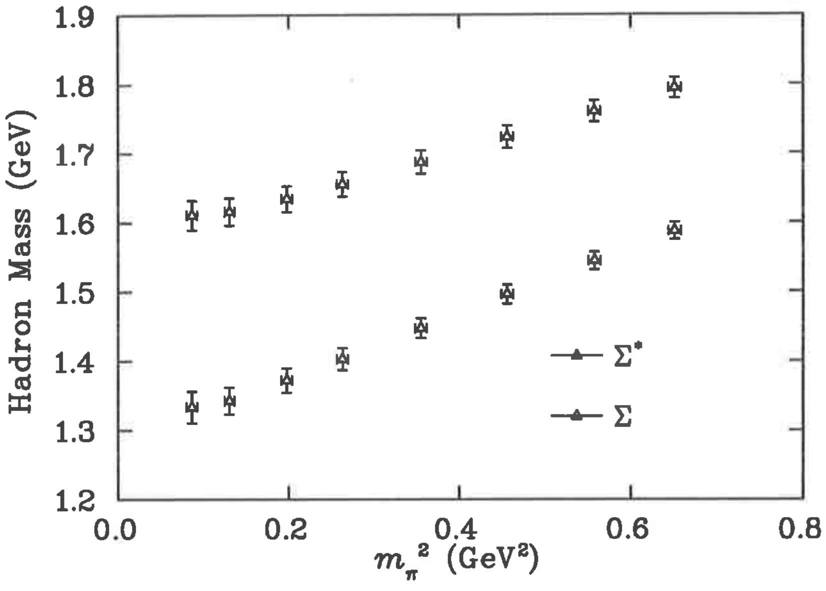

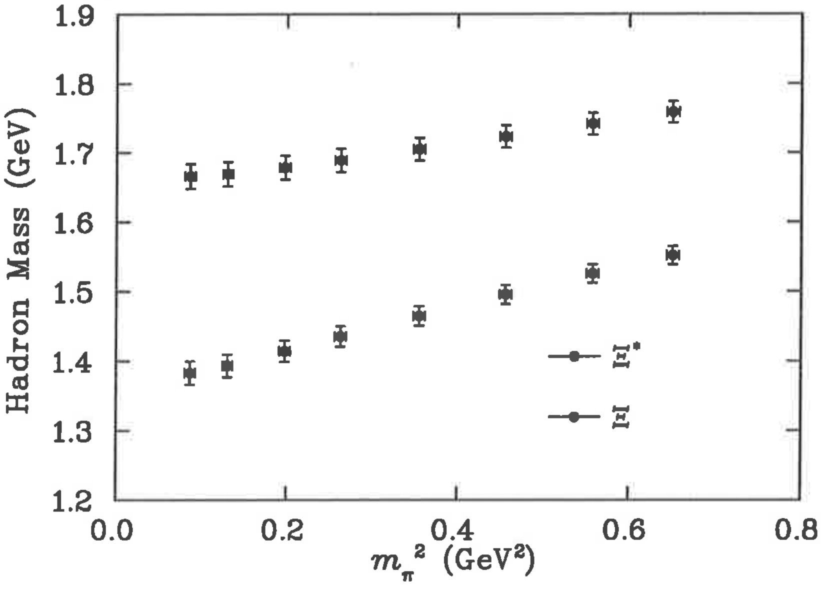

Figure 6.11: Octet and decuplet baryon masses for Σ (top) and Ξ (bottom) for the FLIC-fermion action on a $20^3 \times 40$ lattice with $a = 0.132$ fm.

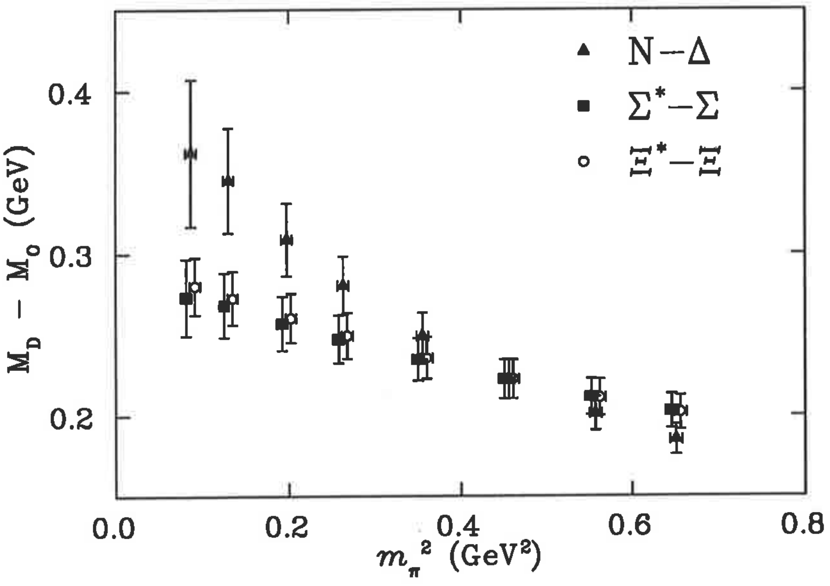

Figure 6.12: Octet-decuplet baryon mass splittings for the FLIC-fermion action on a $20^3 \times 40$ lattice with $a = 0.132$ fm.

7

Excited Baryons in Lattice QCD

7.1 Introduction

Understanding the dynamics responsible for baryon excitations provides valuable insight into the forces which confine quarks inside baryons and into the nature of QCD in the nonperturbative regime. This is a driving force behind the experimental effort of the CLAS Collaboration at Jefferson Lab, which is currently accumulating data of unprecedented quality and quantity on various $N \to N^*$ transitions. With the increased precision of the data comes a growing need to understand the observed N^* spectrum within QCD. Although phenomenological low-energy models of QCD have been successful in describing many features of the N^* spectrum (for a recent review see Ref. [81]), they leave many questions unanswered, and calculations of N^* properties from first principles are indispensable.

Recall from Chapter 2 that one of the long-standing puzzles in spectroscopy has been the low mass of the first positive parity excitation of the nucleon (the $J^P = \frac{1}{2}^+$ $N^*(1440)$ Roper resonance) compared with the lowest lying odd parity excitation. In a valence quark model, in a harmonic oscillator basis, the $\frac{1}{2}^-$ state naturally occurs below the $N = 2$, $\frac{1}{2}^+$ state [82]. Without fine tuning of parameters, valence quark models tend to leave the mass of the Roper resonance too high. Similar difficulties in the level orderings appear for the $\frac{3}{2}^+$ $\Delta^*(1600)$ and $\frac{1}{2}^+$ $\Sigma^*(1690)$, which has led to speculations that the Roper resonances may be more appropriately viewed as "breathing modes" of the confining cavity [83], or described in terms of meson-baryon dynamics alone [84], or as hybrid baryon states with explicitly excited glue field configurations [85].

Another challenge for spectroscopy is presented by the $\Lambda^{1/2-}(1405)$, whose anomalously small mass has been interpreted as an indication of strong coupled channel effects involving $\Sigma\pi$, $N\bar{K}$, $\cdots$ [86], and a weak overlap with a three-valence constituent-quark state. In fact, the role played by Goldstone bosons in baryon spectroscopy has received considerable attention recently [80,87].

It has been argued [88] that a spin-flavor interaction associated with the exchange of a pseudoscalar nonet of Goldstone bosons between quarks can better explain the level orderings and hyperfine mass splittings than the traditional (color-magnetic) one gluon exchange mechanism. On the other hand, some elements of this approach, such as the generalization to the meson sector or consistency with the chiral properties of QCD, remain controversial [81, 89, 90]. Furthermore, neither spin-flavor nor color-magnetic interactions are able to account for the mass splitting between the $\Lambda^{1/2^-}(1405)$ and the $\Lambda^{3/2^-}(1520)$ (a splitting between these can arise in constituent quark models with a spin-orbit interaction, however, this is known to lead to spurious mass splittings elsewhere [81, 91]). Recent work [92] on negative parity baryon spectroscopy in the large-N_c limit has identified important operators associated with spin-spin, spin-flavor and other interactions which go beyond the simple constituent quark model, as anticipated by early QCD sum-rule analyses [93].

The large number of states predicted by the constituent quark model and its generalizations which have not been observed (the so-called "missing" resonances) presents another problem for spectroscopy. If these states do not exist, this may suggest that perhaps a quark–diquark picture (with fewer degrees of freedom) could afford a more efficient description, although lattice simulation results provide no evidence for diquark clustering [94]. On the other hand, the missing states could simply have weak couplings to the πN system [81]. Such a case would present lattice QCD with a unique opportunity to complement experimental searches for N^*'s, by identifying excited states not easily accessible to experiment (as in the case of glueballs or hybrids).

In attempting to answer these questions, one fact that will be clear is that it is not sufficient to look only at the standard low mass hadrons (π, ρ, N and Δ) on the lattice — one must consider the entire N^* (and in fact the entire excited baryon) spectrum. In this chapter we present results of octet baryon mass simulations using an $\mathcal{O}(a^2)$ improved gluon action and an improved Fat Link Irrelevant Clover (FLIC) [72] quark action. All formalism of correlation functions and interpolating fields presented in this chapter is done in the Dirac representation of the γ matrices (see Appendix A). After reviewing in Section 7.2 the main elements of lattice calculations of excited hadron masses and a brief overview of earlier calculations, we describe in Section 7.3 various features of interpolating fields used in this analysis. In Section 7.4 we present results for $J^P = \frac{1}{2}^{\pm}$ nucleons and hyperons. Finally, in Section 7.5 we make concluding remarks and discuss some future extensions of this work.

7.2 Excited Baryons on the Lattice

The history of excited baryons on the lattice is quite brief, although recently there has been growing interest in finding new techniques to isolate excited baryons, motivated partly by the experimental N^* program at Jefferson Lab. The first comprehensive analysis of the positive parity excitation of the nucleon was performed by Leinweber [95] using Wilson fermions and an operator product expansion spectral ansatz. DeGrand and Hecht [96] used a "wave function technique" to access P-wave baryons. Subsequently, Lee & Leinweber [97] introduced a parity projection technique to study the negative parity $\frac{1}{2}^-$ states using an $\mathcal{O}(a^2)$ tree-level tadpole-improved $\mathrm{D}_{\chi 34}$ quark action, and an $\mathcal{O}(a^2)$ tree-level tadpole-improved gauge action. Following this, Lee [98] reported results using a D_{234} quark action with an improved gauge action on an anisotropic lattice to study the $\frac{1}{2}^+$ and $\frac{1}{2}^-$ excitations of the nucleon. The RIKEN-BNL group [99] has also performed an analysis of the $N^*(\frac{1}{2}^-)$ and $N'(\frac{1}{2}^+)$ excited states using domain wall fermions. More recently, a nonperturbatively improved clover quark action has been used by Richards et al. [100, 101] to study the $N^*(\frac{1}{2}^-)$ and $\Delta^*(\frac{3}{2}^-)$ states.

Following standard notation, we define a two-point correlation function for a baryon B as

$$G_B(t,\vec{p}) \equiv \sum_{\vec{x}} e^{-i\vec{p}\cdot\vec{x}} \langle 0 \,|T \chi_B(x)\; \bar{\chi}_B(0)|\, 0\rangle \ , \tag{7.1}$$

where χ_B is a baryon interpolating field with definite parity under parity operation, and where we have suppressed Dirac indices. The choice of interpolating field χ_B is discussed in Section 7.3 below. The overlap of a positive parity field χ_B with positive or negative parity states $|B^\pm\rangle$ is parameterized by a coupling strength $\lambda_{B^\pm}$

$$\begin{aligned} \langle 0 \,|\, \chi_B(0) \,|\, B^+(p,s)\rangle &= \lambda_{B^+}\sqrt{\frac{M_{B^+}}{E_{B^+}}}\, u_{B^+}(p,s) \ , & (7.2)\\ \langle 0 \,|\, \chi_B(0) \,|\, B^-(p,s)\rangle &= \lambda_{B^-}\sqrt{\frac{M_{B^-}}{E_{B^-}}}\, \gamma_5 u_{B^-}(p,s) \ , & (7.3) \end{aligned}$$

where $E_{B^\pm} = \sqrt{M_{B^\pm}^2 + \vec{p}^{\,2}}$ is the energy, and $u_{B^\pm}(p,s)$ a Dirac spinor with normalisation $1/\sqrt{2E_B}$. For large Euclidean time, the correlation function can be written as a sum of the lowest energy positive and negative parity contributions

$$G_B(t,\vec{p}) \;\approx\; \lambda_{B^+}^2 \frac{(\gamma\cdot p + M_{B^+})}{2E_{B^+}} e^{-E_{B^+}\,t} + \lambda_{B^-}^2 \frac{(\gamma\cdot p - M_{B^-})}{2E_{B^-}} e^{-E_{B^-}\,t} \ , \tag{7.4}$$

when a fixed boundary condition in the time direction is used to remove backward propagating states. The positive and negative parity states are isolated by taking the trace of G_B with the operator $\Gamma_\pm$, where

$$\Gamma_\pm \;=\; \frac{1}{2}\left(1 \pm \frac{M_{B^\pm}}{E_{B^\pm}}\gamma_4\right) \ . \tag{7.5}$$

For $\vec{p} = 0$, $\Gamma_\pm^2 = \Gamma_\pm$ so that $\Gamma_\pm$ are then parity projectors. For $\vec{p} = 0$, $E_{B^\pm} = M_{B^\pm}$ and using the operator $\Gamma_\pm$ we can isolate the mass, $M_{B^\pm}$, of the baryon $B^\pm$. In this case, positive parity states propagate in the (1, 1) and (2, 2) elements of the Dirac matrix of Eq. (7.4), while negative parity states propagate in the (3, 3) and (4, 4) elements.

In terms of the correlation function G_B, the baryon effective-mass function is defined by

$$M_B(t + 1/2) = \log[G_B(t, \vec{0})] - \log[G_B(t + 1, \vec{0})] \ . \qquad (7.6)$$

Meson masses are determined via analogous standard procedures.

7.3 Interpolating Fields

In this analysis we consider two types of interpolating fields which have been used in the literature. The notation adopted follows that of Leinweber *et al.* [102]. To access the positive parity proton we use as interpolating fields

$$\chi_1^{p+}(x) \quad = \quad \epsilon_{abc} \left(u_a^T(x)\ C\gamma_5\ d_b(x) \right) u_c(x)\ , \qquad (7.7)$$

and

$$\chi_2^{p+}(x) \quad = \quad \epsilon_{abc} \left(u_a^T(x)\ C\ d_b(x) \right) \gamma_5\ u_c(x)\ , \qquad (7.8)$$

where the fields u, d are evaluated at Euclidean space-time point x, C is the charge conjugation matrix, a, b and c are color labels, and where the superscript T denotes the transpose. Here we introduce the convenient shorthand notation

$$\begin{aligned} \mathcal{F}(S_{f_1}, S_{f_2}, S_{f_3}) = \epsilon^{abc}\epsilon^{a'b'c'} \Big\{ &\ S_{f_1}^{aa'}(x,0) \quad \mathrm{tr}\left[S_{f_2}^{bb'}(x,0) S_{f_3}^{cc'\,T}(x,0) \right] \\ &+\ S_{f_1}^{aa'}(x,0) \quad S_{f_3}^{cc'\,T}(x,0)\, S_{f_2}^{bb'}(x,0) \Big\}, \end{aligned} \qquad (7.9)$$

where $S^{aa'}(x,0)$ is the quark propagator in the background link-field configuration U and f_1, f_2, f_3 are flavor labels. This allows us to express the correlation functions in a compact form. Hence, we can write the associated correlation function for χ_1^{p+} as

$$G_{11}^{p+}(t, \vec{p}; \Gamma) = \left\langle \sum_{\vec{x}} e^{-i\vec{p}\cdot\vec{x}} \mathrm{tr} \left[-\Gamma\ \mathcal{F}\left(S_u,\ S_u,\ C\gamma_5 S_d \gamma_5 C \right) \right] \right\rangle, \qquad (7.10)$$

where $\langle \ldots \rangle$ is the ensemble average over the link fields and Γ is the $\Gamma_\pm$ projection operator from Eq. 7.5. For ease of notation, we will now drop the angle brackets and all the following correlation functions, G, will be understood to be ensemble averages. Similarly, for χ_2^{p+}

$$G_{22}^{p+}(t,\vec{p};\Gamma) = \sum_{\vec{x}} e^{-i\vec{p}\cdot\vec{x}} \mathrm{tr}\left[-\Gamma\ \mathcal{F}\left(\gamma_5 S_u \gamma_5,\ \gamma_5 S_u \gamma_5,\ C\gamma_5 S_d \gamma_5 C\right)\right], \qquad (7.11)$$

while the interference terms from these two interpolating fields are given by

$$\begin{aligned} G_{12}^{p+}(t,\vec{p};\Gamma) &= \sum_{\vec{x}} e^{-i\vec{p}\cdot\vec{x}} \mathrm{tr}\Big[-\Gamma\ \Big\{\mathcal{F}\left(S_u\gamma_5,\ S_u\gamma_5,\ C\gamma_5 S_d \gamma_5 C\right)\Big\}\Big], & (7.12)\\ G_{21}^{p+}(t,\vec{p};\Gamma) &= \sum_{\vec{x}} e^{-i\vec{p}\cdot\vec{x}} \mathrm{tr}\Big[-\Gamma\ \Big\{\mathcal{F}\left(\gamma_5 S_u,\ \gamma_5 S_u,\ C\gamma_5 S_d \gamma_5 C\right)\Big\}\Big]. & (7.13) \end{aligned}$$

The neutron interpolating field is obtained via the exchange $u \leftrightarrow d$, and we can also obtain the strangeness –2, Ξ interpolating field by replacing the doubly represented u or d quark fields in Eqs. (7.7) and (7.8) by s quark fields. As pointed out by Leinweber [95], because of the Dirac structure of the "diquark" in the parentheses in Eq.(7.7), the field χ_1^{p+} involves both products of *upper* × *upper* × *upper* and *lower* × *lower* × *upper* components of spinors for positive parity baryons, so that in the nonrelativistic limit $\chi_1^{p+} = \mathcal{O}(1)$. Here upper and lower refer to the large and small spinor components in the standard Dirac representation of the γ matrices. A representation independent language would use large and small in place of upper and lower. Furthermore, since the "diquark" couples to a total spin 0, one expects an attractive force between the two quarks, and hence a lower energy state than for a state in which two quarks do not couple to spin 0.

The χ_2^{p+} interpolating field, on the other hand, is known to have little overlap with the ground state [95,103]. Inspection of the structure of the Dirac matrices in Eq.(7.8) reveals that it involves only products of *upper* × *lower* × *lower* components for positive parity baryons, so that $\chi_2^{p+} = \mathcal{O}(p^2/E^2)$ vanishes in the nonrelativistic limit. As a result of the mixing, the "diquark" term contains a factor $\vec{\sigma}\cdot\vec{p}$, meaning that the quarks no longer couple to spin 0, but are in a relative $L = 1$ state. One expects therefore that two-point correlation functions constructed from the interpolating field χ_2^{p+} are dominated by larger mass states than those arising from χ_1^{p+} at early Euclidean times.

While the masses of negative parity baryons can be and are obtained directly from the (positive parity) interpolating fields in Eqs.(7.7) and (7.8) by using the parity projectors $\Gamma_\pm$, it is instructive nevertheless to examine the general properties of the negative parity interpolating fields. Interpolating fields with strong overlap with the negative parity proton can be constructed by multiplying the previous positive parity interpolating fields by γ_5, $\chi^{B-} \equiv \gamma_5\, \chi^{B+}$. In contrast to the positive parity case, both the interpolating fields χ_1^{p-} and χ_2^{p-} mix upper and lower components, and consequently both χ_1^{p-} and χ_2^{p-} are $\mathcal{O}(p/E)$.

Physically, two nearby $J^P = \frac{1}{2}^-$ states are observed in the nucleon spectrum. In simple quark models, the splitting of these two orthogonal states is largely attributed to the extent to which scalar diquark configurations compose the wave function. It is reasonable to expect χ_1^{p-} to have better overlap with scalar diquark dominated states, and thus provide a lower effective mass in the large Euclidean time regime explored in lattice simulations. If the effective mass associated with the χ_2^{p-} correlator is larger, then this would be evidence of significant overlap of χ_2^{p-} with the higher lying $N\frac{1}{2}^-$ states. In this event, a correlation matrix analysis (see Appendix C) will be used to isolate these two states.

Interpolating fields for the other members of the flavor SU(3) octet are constructed along similar lines. For the positive parity Σ^0 hyperon one has [102]

$$\chi_1^{\Sigma}(x) = \frac{1}{\sqrt{2}}\epsilon_{abc}\left\{\left(u_a^T(x)\ C\gamma_5\ s_b(x)\right) d_c(x)\ +\ \left(d_a^T(x)\ C\gamma_5\ s_b(x)\right) u_c(x)\right\}\ , \tag{7.14}$$

and similarly for the χ_2^{Σ} field. Interpolating fields used for accessing other charge states are obtained by $d \to u$ or $u \to d$. Notice that χ_1^{Σ} transforms as a triplet under SU(2) isospin. An SU(2) singlet interpolating field can be constructed by replacing "+" $\longrightarrow$ "−" in Eq. (7.14). For the SU(3) octet Λ interpolating field (denoted by "Λ^8"), one has

$$\begin{aligned}\chi_1^{\Lambda^8}(x) &= \frac{1}{\sqrt{6}}\epsilon_{abc}\left\{2\left(u_a^T(x)\ C\gamma_5\ d_b(x)\right) s_c(x) + \left(u_a^T(x)\ C\gamma_5\ s_b(x)\right) d_c(x)\right.\\ &\qquad \left. -\ \left(d_a^T(x)\ C\gamma_5\ s_b(x)\right) u_c(x)\right\}\ ,\end{aligned} \tag{7.15}$$

which leads to the following correlation function

$$\begin{aligned}G_{11}^{\Lambda^8}(t,\vec{p};\Gamma) &= \frac{1}{6}\sum_{\vec{x}} e^{-i\vec{p}\cdot\vec{x}}\\ &\mathrm{tr}\left[-\Gamma\ \left\{\ 2\mathcal{F}\left(S_s,\, S_d,\, \widetilde{C}S_u\widetilde{C}^{-1}\right) + 2\mathcal{F}\left(S_s,\, S_u,\, \widetilde{C}S_d\widetilde{C}^{-1}\right)\right.\right.\\ &\quad +\ 2\mathcal{F}\left(S_d,\, S_s,\, \widetilde{C}S_u\widetilde{C}^{-1}\right) + 2\mathcal{F}\left(S_u,\, S_s,\, \widetilde{C}S_d\widetilde{C}^{-1}\right)\\ &\quad \left.\left. -\ \mathcal{F}\left(S_d,\, S_u,\, \widetilde{C}S_s\widetilde{C}^{-1}\right) -\ \mathcal{F}\left(S_u,\, S_d,\, \widetilde{C}S_s\widetilde{C}^{-1}\right)\right\}\right]\end{aligned} \tag{7.16}$$

where $\widetilde{C} = C\gamma_5$. Similarly, the interpolating field (and thus correlation function) for $\chi_2^{\Lambda^8}$ is obtained by simply moving the γ_5 in each of the terms as was done to obtain Eq. (7.8) from Eq. (7.7).

The interpolating field for the SU(3) flavor singlet (denoted by "Λ^1") is given by [102]

$$\begin{aligned}\chi_1^{\Lambda^1}(x) &= -2\,\epsilon_{abc}\big\{-\big(u_a^T(x)\;C\gamma_5\;d_b(x)\big)\,s_c(x) + \big(u_a^T(x)\;C\gamma_5\;s_b(x)\big)\,d_c(x)\\ &\qquad - \big(d_a^T(x)\;C\gamma_5\;s_b(x)\big)\,u_c(x)\big\}\ , \qquad (7.17)\end{aligned}$$

where the last two terms are common to both $\chi_1^{\Lambda^8}$ and $\chi_1^{\Lambda^1}$. The correlation function resulting from this field involves quite a few terms,

$$\begin{aligned}&G_{11}^{\Lambda^1}(t,\vec{p};\Gamma) =\\ &\sum_{\vec{x}} e^{-i\vec{p}\cdot\vec{x}} tr\Big[-\Gamma\,\Big\{\ \gamma_5 S_s^{aa'}\,\widetilde{C} S_d^{cc'\,T}\widetilde{C}^{-1}\,S_u^{bb'}\gamma_5 + \gamma_5 S_u^{aa'}\,\widetilde{C} S_d^{cc'\,T}\widetilde{C}^{-1}\,S_s^{bb'}\gamma_5\\ &\qquad +\gamma_5 S_s^{aa'}\,\widetilde{C} S_u^{cc'\,T}\widetilde{C}^{-1}\,S_d^{bb'}\gamma_5 + \gamma_5 S_d^{aa'}\,\widetilde{C} S_u^{cc'\,T}\widetilde{C}^{-1}\,S_s^{bb'}\gamma_5\\ &\qquad +\gamma_5 S_u^{aa'}\,\widetilde{C} S_s^{cc'\,T}\widetilde{C}^{-1}\,S_d^{bb'}\gamma_5 + \gamma_5 S_d^{aa'}\,\widetilde{C} S_s^{cc'\,T}\widetilde{C}^{-1}\,S_u^{bb'}\gamma_5\\ &\qquad -\gamma_5 S_s^{aa'}\gamma_5\ \mathrm{tr}\Big[S_d^{bb'}\,\widetilde{C} S_u^{cc'\,T}\widetilde{C}^{-1}\Big]\\ &\qquad -\gamma_5 S_u^{aa'}\gamma_5\ \mathrm{tr}\Big[S_s^{bb'}\,\widetilde{C} S_d^{cc'\,T}\widetilde{C}^{-1}\Big]\\ &\qquad -\gamma_5 S_d^{aa'}\gamma_5\ \mathrm{tr}\Big[S_u^{bb'}\,\widetilde{C} S_s^{cc'\,T}\widetilde{C}^{-1}\Big]\Big\}\Big]. \qquad (7.18)\end{aligned}$$

In order to test the extent to which SU(3) flavor symmetry is valid in the baryon spectrum, one can construct another combined interpolating field composed of the terms common to Λ^1 and Λ^8, which does not make any assumptions about SU(3) flavor symmetry properties of Λ. We define

$$\chi_1^{\Lambda^c}(x) = \frac{1}{\sqrt{2}}\epsilon_{abc}\big\{\big(u_a^T(x)\;C\gamma_5\;s_b(x)\big)\,d_c(x) - \big(d_a^T(x)\;C\gamma_5\;s_b(x)\big)\,u_c(x)\big\}\,, \qquad (7.19)$$

to be our "common" interpolating field which is the isosinglet analogue of χ_1^{Σ} in Eq. (7.14).

To appreciate the structure of the "common" correlation function, one can introduce the function

$$\begin{aligned}\overline{\mathcal{F}}(S_{f_1},S_{f_2},S_{f_3}) = \epsilon^{abc}\epsilon^{a'b'c'}\ &\Big\{\ S_{f_1}^{aa'}(x,0)\,\mathrm{tr}\Big[S_{f_2}^{bb'}(x,0)S_{f_3}^{cc'\,T}(x,0)\Big]\\ &-\ S_{f_1}^{aa'}(x,0)\,S_{f_3}^{cc'\,T}(x,0)\,S_{f_2}^{bb'}(x,0)\Big\}, \qquad (7.20)\end{aligned}$$

which is recognised as $\mathcal{F}$ in Eq. (7.9) with the relative sign of the two terms changed. With this notation, the correlation function of Λ^c is

$$\begin{aligned}G^{\Lambda c}(t,\vec{p};\Gamma) &= \frac{1}{2}\sum_{\vec{x}} e^{-i\vec{p}\cdot\vec{x}}\mathrm{tr}\Big[-\Gamma\,\Big\{\overline{\mathcal{F}}\,(S_d,\,S_u,\,C\gamma_5 S_s\gamma_5 C)\\ &\qquad +\overline{\mathcal{F}}\,(S_u,\,S_d,\,C\gamma_5 S_s\gamma_5 C)\Big\}\Big] \qquad (7.21)\end{aligned}$$

Interpolating fields for $\chi_2^{\Lambda^1}$ and $\chi_2^{\Lambda^c}$, and the corresponding correlation functions, are similarly constructed. Such interpolating fields may be useful in determining the nature of the $\Lambda^*(1405)$ resonance, as they allow for mixing between singlet and octet states induced by SU(3) flavor symmetry breaking.

7.4 Results

The calculations of octet excited baryon masses are performed on a $16^3 \times 32$ lattice at $\beta = 4.60$, which corresponds to a lattice spacing of $a = 0.122(2)$ fm set by the string tension [57] as in Chapter 5 with $\sqrt{\sigma} = 440$ MeV. The analysis in the nucleon sector is based on a sample of 400 configurations, while the baryons containing one or more strange quark is based upon a sample of 200 configurations. For the gauge fields, a mean-field improved plaquette plus rectangle action (Eq. (3.15)) is used, while for the quark fields, a Fat-Link Irrelevant Clover (FLIC) [72] action (Eq. (6.4)) is implemented. Since the results with $n = 4$ sweeps exhibit slightly better scaling than those with $n = 12$ (see Section 6.4), we focus on the results with 4 smearing sweeps. The 12-sweep results are consistent with all our conclusions.

A fixed boundary condition in the time direction is used for the fermions by setting $U_t(\vec{x}, N_t) = 0 \ \forall \ \vec{x}$ in the hopping terms of the fermion action, with periodic boundary conditions imposed in the spatial directions. Gauge-invariant gaussian smearing [76] in the spatial dimensions is applied at the source to increase the overlap of the interpolating operators with the ground states.

Figure 7.1 shows the positive and negative parity nucleon effective mass plots for both χ_1 and χ_2 interpolating fields for the FLIC action. The effective mass plots for the other hadrons are similar, and all display acceptable plateau behavior. Good values of covariance matrix based $\chi^2/N_{\rm DF}$ are obtained for the ground state nucleon (N_1) for many different time-fitting intervals as long as one fits after time slice 8. All fits for the positive parity states obtained with the χ_1 interpolating fields for this action are therefore performed on time slices 9 through 14.

The lowest $J^P = \frac{1}{2}^-$ excitation for the χ_1 interpolating field (N_1^*) uses time slices 9–12. The states obtained from the χ_2 interpolating field, however, plateau at earlier times and are also subject to noise earlier in time than the states obtained with the χ_1 field. For these reasons, good values of $\chi^2/N_{\rm DF}$ are obtained on the time interval 6–8 for the positive parity states, and negative parity states are fitted using the time interval 8–11.

We check the trustworthiness of these masses by comparing the values with those from the diagonalisation discussed in Appendix C using timeslices 8 and

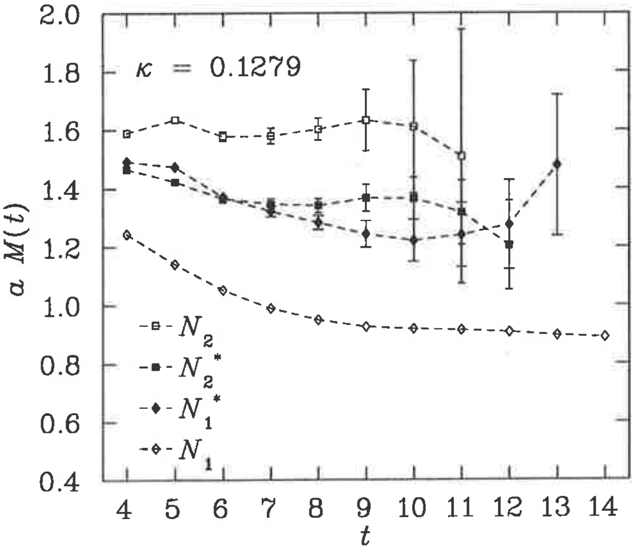

Figure 7.1: Effective masses of the lowest lying positive and negative parity nucleon states using the FLIC action defined with 4 sweeps of smearing at $\alpha = 0.7$. The $J^P = \frac{1}{2}^+$ $(\frac{1}{2}^-)$ states labeled N_1 (N_1^*) and N_2 (N_2^*) are obtained using the χ_1 and χ_2 interpolating fields, respectively.

9. This is done by minimising the measure

$$\frac{1}{N}\sum_{n=1}^{N}\left|1 - \frac{m_{\text{fit}}^{n}}{m_{\text{eigen}}^{n}}\right| .$$

where m_{fit}^n and m_{eigen}^n are the masses of the n^{th} state obtained from a naive exponential fit to the correlation function and the eigenvalue analysis respectively. For perfect agreement (which would coincide to the case where the correlation functions can be expressed in terms of N masses) it is clear that this quantity goes to zero. Our calculations do indeed get small values. Recall that the covariance matrix tells us that $t = 9$ is the earliest time at which it is reasonable to assume that we have a single state in our positive parity correlation function, so it is thus reasonable to assume that at one time step earlier we have only two states involved.

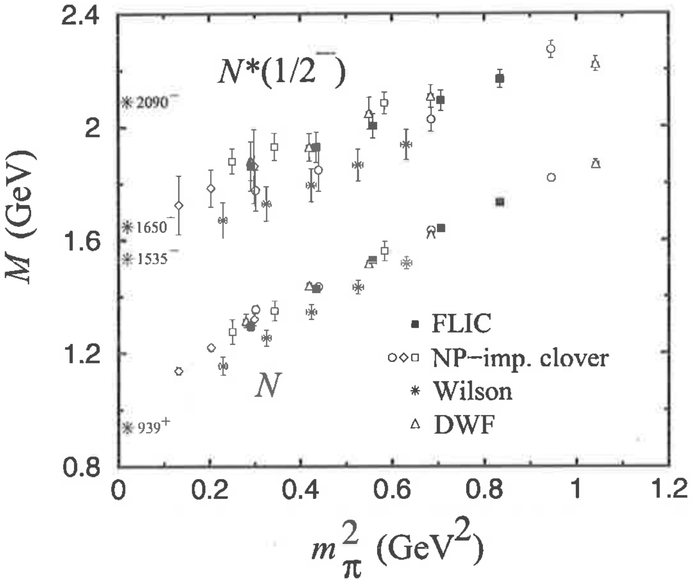

Figure 7.2: Masses of the nucleon (N) and the lowest $J^P = \frac{1}{2}^-$ excitation ("N^*"), obtained from the χ_1 interpolating field. The FLIC and Wilson results are from the present analysis, with the DWF [99] and NP improved clover [100,101] results shown for comparison. The empirical nucleon and low lying $N^*(\frac{1}{2}^-)$ masses are indicated by the asterisks along the ordinate.

In Fig. 7.2 we show the nucleon and $N^*(\frac{1}{2}^-)$ masses as a function of the pseudoscalar meson mass squared, m_π^2. The results of the new simulations, using the χ_1 interpolating field, Eq. (7.7), are indicated by the filled squares for the FLIC action, and by the stars for the Wilson action (the Wilson points are obtained from a sample of 50 configurations). The values of m_π^2 correspond to κ values given in Table 7.1.

For comparison, we also show results from earlier simulations with domain wall fermions (DWF) [99] (open triangles), and a nonperturbatively (NP) improved clover action at $\beta = 6.2$ [100, 101]. The scatter of the different NP improved results is due to different source smearing and volume effects: the open squares are obtained by using fuzzed sources and local sinks, the open circles use Jacobi smearing at both the source and sink, while the open diamonds, which extend to smaller quark masses, are obtained from a larger lattice ($32^3 \times 64$) using Jacobi smearing. The empirical masses of the nucleon and the three lowest $\frac{1}{2}^-$ excitations are indicated by the asterisks along the ordinate.

There is excellent agreement between the different improved actions for the

κ	$m_\pi a$	$m_{N_1} a$	$m_{N_1^*} a$	$m_{N_2^*} a$	$m_{N_2} a$
0.1260	0.5807(18)	1.0969(43)	1.383(13)	1.439(12)	1.676(11)
0.1266	0.5343(19)	1.0397(47)	1.335(15)	1.401(15)	1.641(12)
0.1273	0.4757(21)	0.9699(54)	1.280(18)	1.364(20)	1.604(14)
0.1279	0.4201(23)	0.9067(63)	1.234(23)	1.343(20)	1.579(17)
0.1286	0.3454(27)	0.8283(80)	1.183(34)	1.346(36)	1.569(25)

Table 7.1: Values of κ used in this analysis and the corresponding π, N_1, N_1^*, N_2^* and N_2 masses for the FLIC action with 4 sweeps of smearing at $\alpha = 0.7$. Here $\kappa_{\rm cr} = 0.1300$, and a string tension analysis provides $a = 0.122(2)$ fm for $\sqrt{\sigma} = 440$ MeV.

nucleon mass, in particular between the FLIC, DWF [99] and NP improved clover [100,101] results. On the other hand, the Wilson results lie systematically low in comparison to these due to the large $\mathcal{O}(a)$ errors in this action (see Chapter 6 and Ref. [72]). A similar pattern is repeated for the $N^*(\frac{1}{2}^-)$ masses. Namely, the FLIC, DWF and NP improved clover masses are in good agreement with each other, while the Wilson results again lie systematically lower. A mass splitting of around 400 MeV is clearly visible between the N and N^* for all actions, including the Wilson action, despite its poor chiral properties. Furthermore, the trend of the $N^*(\frac{1}{2}^-)$ data with decreasing m_π is consistent with the mass of the lowest lying physical negative parity N^* states.

Figure 7.3 shows the mass of the $J^P = \frac{1}{2}^+$ state obtained from the χ_2 interpolating field in Eq. (7.8) (denoted by "$N'(1/2^+)$"). Data for the nucleon sector are provided in Table 7.1. As is long known, the positive parity χ_2 interpolating field does not have good overlap with the nucleon ground state [95]. It has been speculated that it may have overlap with the lowest $\frac{1}{2}^+$ excited state, the $N^*(1440)$ Roper resonance [99]. In addition to the FLIC and Wilson results from the present analysis, we also show in Fig. 7.3 the DWF results [99], and results from an earlier analysis with Wilson fermions together with the operator product expansion [95]. The physical values of the lowest three $\frac{1}{2}^+$ excitations of the nucleon are indicated by the asterisks.

The most striking feature of the data is the relatively large excitation energy of the N', some 1 GeV above the nucleon. There is little evidence, therefore, that this state is the $N^*(1440)$ Roper resonance. While it is possible that the Roper resonance may have a strong nonlinear dependence on the quark mass at $m_\pi^2 \lesssim 0.2$ GeV^2, arising from, for example, pion loop corrections, it is unlikely that this behavior would be so dramatically different from that of the $N^*(1535)$

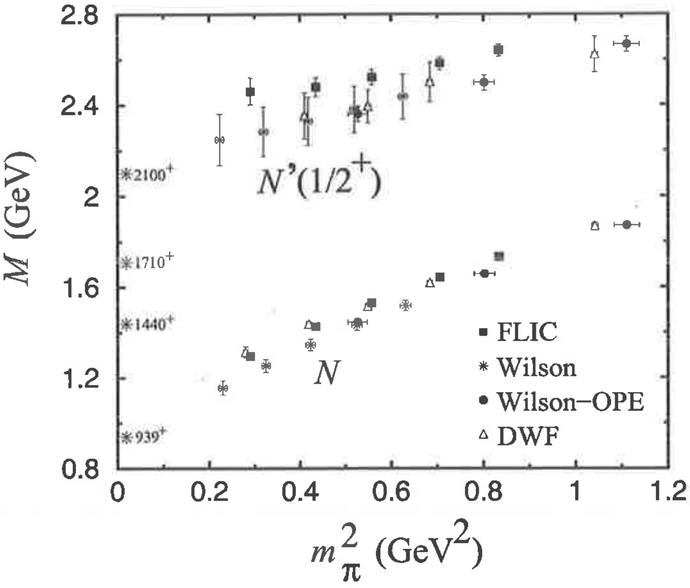

Figure 7.3: Masses of the nucleon, and the lowest $J^P = \frac{1}{2}^+$ excitation ("N'") obtained from the χ_2 interpolating field. The FLIC results are compared with the earlier DWF [99] and Wilson-OPE [95] analyses, as well as with the Wilson results from this analysis. The empirical nucleon and low lying $N^*(\frac{1}{2}^+)$ masses are indicated by asterisks.

so as to reverse the level ordering obtained from the lattice. A more likely explanation is that the χ_2 interpolating field does not have good overlap with either the nucleon or the $N^*(1440)$, but rather a (combination of) excited $\frac{1}{2}^+$ state(s).

Recall that in a constituent quark model in a harmonic oscillator basis, the mass of the lowest mass state with the Roper quantum numbers is higher than the lowest P-wave excitation. It seems that neither the lattice data (at large quark masses and with our interpolating fields) nor the constituent quark model have good overlap with the Roper resonance. Better overlap with the Roper is likely to require more exotic interpolating fields.

In Fig. 7.4 we show the ratio of the masses of the $N^*(\frac{1}{2}^-)$ and the nucleon, using the χ_1 interpolating field. Once again, there is good agreement between the FLIC and DWF actions. However, the results for the Wilson action lie above the others, as do those for the anisotropic D_{234} action [98]. The D_{234} action has been mean-field improved, and uses an anisotropic lattice which is relatively

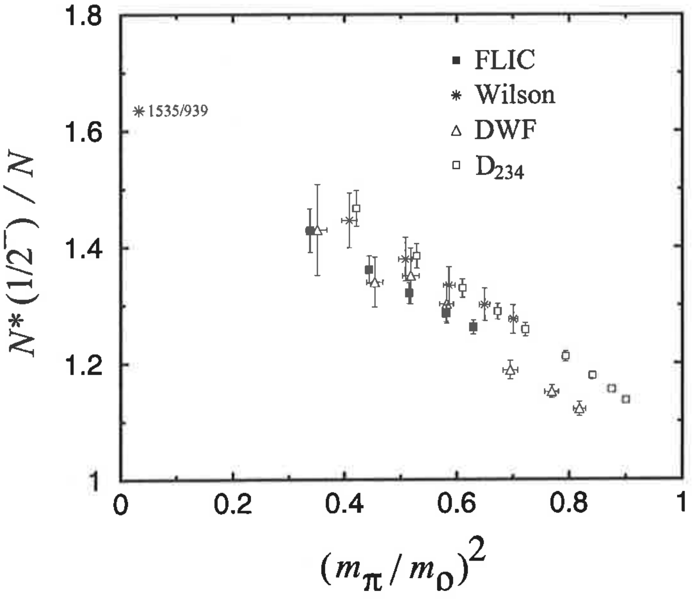

Figure 7.4: Ratio of the ground state $N^*(\frac{1}{2}^-)$ and nucleon masses, from the χ_1 interpolating field. The FLIC and Wilson results are from the present analysis, with results from the D_{234} [98] and DWF [99] actions shown for comparison. The empirical $N^*(1535)/N$ mass ratio is denoted by the asterisk.

coarse in the spatial direction ($a \approx 0.24$ fm). This is perhaps an indication of the need for nonperturbative or fat-link improvement.

The mass splitting between the two lightest $N^*(\frac{1}{2}^-)$ states ($N^*(1535)$ and $N^*(1650)$) can be studied by considering the odd parity content of the χ_1 and χ_2 interpolating fields in Eqs. (7.7) and (7.8). Recall that the "diquarks" in χ_1 and χ_2 couple differently to spin, so that even though the correlation functions built up from the χ_1 and χ_2 fields will be made up of a mixture of many excited states, they will have dominant overlap with different states, yielding different masses [95,97]. By using the variational techniques described in Appendix C, we extract two seperate mass states from our χ_1 and χ_2 interpolating fields. The results from the rotation of the correlation matrix are shown by the solid symbols in Fig. 7.5 and are compared to the standard "naive" fits performed directly on the correlation functions which are shown by the open symbols. The results, shown in Fig. 7.5 for the FLIC action, indicate that indeed the $N^*(\frac{1}{2}^-)$ corresponding to the χ_2 field (labeled "N_2^*") lies above the $N^*(\frac{1}{2}^-)$ associated with the χ_1 field ("N_1^*") and that there is only a need for the variational technique to be used

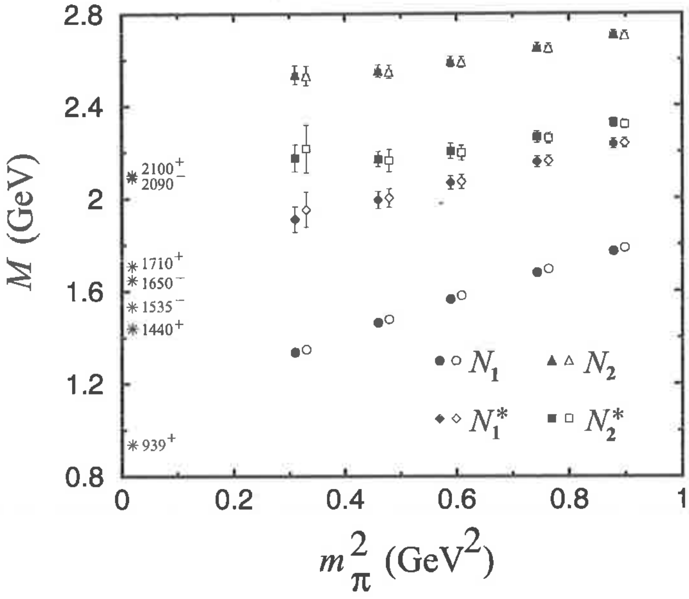

Figure 7.5: Masses of the $J^P = \frac{1}{2}^+$ and $\frac{1}{2}^-$ nucleon states, for the FLIC action. Masses are obtained using the correlation matrix analysis (solid symbols) and naive exponential fits (open symbols). The positive (negative) parity states labeled N_1 (N_1^*) and N_2 (N_2^*) are constructed from the χ_1 and χ_2 interpolating fields, respectively. Empirical masses of the low lying $\frac{1}{2}^\pm$ states are indicated by the asterisks.

for the lightest mass. The masses of the corresponding positive parity states, associated with the χ_1 and χ_2 fields (labeled "N_1" and "N_2", respectively) are shown for comparison. For reference, we also list the empirical values of the low lying $\frac{1}{2}^\pm$ states. It is interesting to note that the mass splitting between the positive parity N_1 and negative parity $N_{1,2}^*$ states (roughly 400–500 MeV) is similar to that between the $N_{1,2}^*$ and the positive parity N_2 state, reminiscent of a constituent–quark harmonic oscillator picture.

Turning to the strange sector, in Fig. 7.6 we show the masses of the positive and negative parity Σ baryons calculated from the FLIC action, and compared with the physical masses of the known positive and negative parity states. The data for these states are listed in Table 7.2. The pattern of mass splittings is similar to that found in Fig. 7.5 for the nucleon. Namely, the $\frac{1}{2}^+$ state associated with the χ_1 field appears consistent with the empirical $\Sigma(1193)$ ground state, while the $\frac{1}{2}^+$ state associated with the χ_2 field lies significantly above the observed first (Roper-like) $\frac{1}{2}^+$ excitation, $\Sigma^*(1660)$. There is also evidence for a

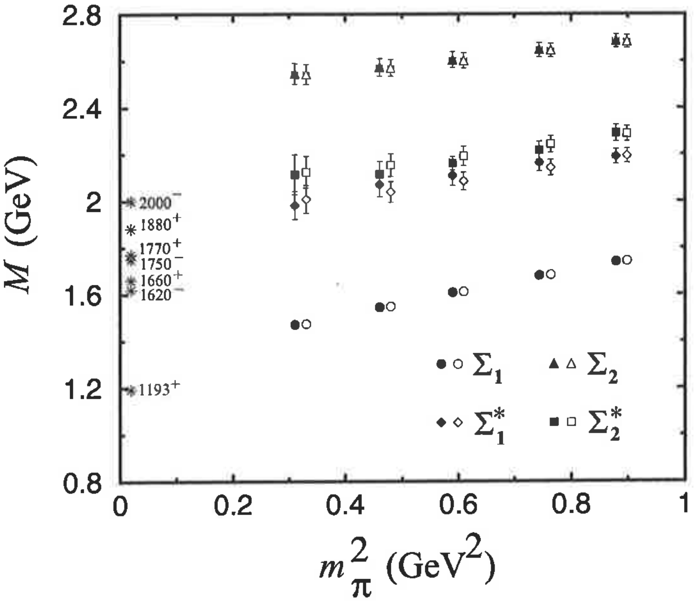

Figure 7.6: As in Fig. 7.5 but for the Σ baryons.

mass splitting between the negative parity states associated with the χ_1 and χ_2 operators, similar to that in the nonstrange sector.

The spectrum of the strangeness -2 positive and negative parity Ξ hyperons is displayed in Fig. 7.7, with data given in Table 7.3. Once again, the pattern of calculated masses repeats that found for the Σ and N masses in Figs. 7.5 and 7.6. The empirical masses of the physical Ξ^* baryons are denoted by asterisks, however, for all but the ground state $\Xi(1318)$, the J^P values are not known.

Finally, we consider the Λ hyperons. In Fig. 7.8 we show the spectrum of positive and negative parity states obtained from our correlation matrix analysis

κ	$m_{\Sigma_1}a$	$m_{\Sigma_1^*}a$	$m_{\Sigma_2^*}a$	$m_{\Sigma_2}a$
0.1260	1.0765(65)	1.356(20)	1.418(22)	1.662(18)
0.1266	1.0395(69)	1.339(23)	1.372(24)	1.638(19)
0.1273	0.9955(76)	1.306(27)	1.338(18)	1.612(21)
0.1279	0.9565(84)	1.282(33)	1.309(34)	1.592(23)
0.1286	0.9103(99)	1.227(37)	1.308(53)	1.575(27)

Table 7.2: As for Table 7.1, but for the Σ states.

κ	$m_{\Xi_1}a$	$m_{\Xi_1^*}a$	$m_{\Xi_2^*}a$	$m_{\Xi_2}a$
0.1260	1.0609(68)	1.342(20)	1.400(22)	1.650(18)
0.1266	1.0395(69)	1.339(23)	1.372(24)	1.638(19)
0.1273	1.0139(72)	1.303(24)	1.380(29)	1.626(20)
0.1279	0.9911(76)	1.302(27)	1.354(36)	1.618(21)
0.1286	0.9636(81)	1.272(30)	1.366(51)	1.612(24)

Table 7.3: As for Table 7.1, but for the Ξ states.

κ	$m_{\Lambda_1}a$	$m_{\Lambda_1^*}a$	$m_{\Lambda_2^*}a$	$m_{\Lambda_2}a$
0.1260	1.0799(65)	1.358(19)	1.413(21)	1.662(17)
0.1266	1.0395(69)	1.339(23)	1.372(24)	1.638(19)
0.1273	0.9900(75)	1.283(25)	1.367(33)	1.614(21)
0.1279	0.9448(83)	1.243(30)	1.361(44)	1.597(24)
0.1286	0.8877(98)	1.189(40)	1.407(80)	1.591(30)

Table 7.4: As for Table 7.1, but for the octet Λ^8 states.

κ	$m_{\Lambda_1}a$	$m_{\Lambda_1^*}a$	$m_{\Lambda_2^*}a$	$m_{\Lambda_2}a$
0.1260	1.0815(65)	1.326(17)	1.394(16)	1.660(17)
0.1266	1.0412(70)	1.294(19)	1.367(18)	1.635(17)
0.1273	0.9916(77)	1.256(22)	1.341(22)	1.608(19)
0.1279	0.9461(84)	1.220(25)	1.327(29)	1.587(20)
0.1286	0.8879(98)	1.173(30)	1.348(51)	1.567(23)

Table 7.5: As for Table 7.1, but for the "common" Λ^c states.

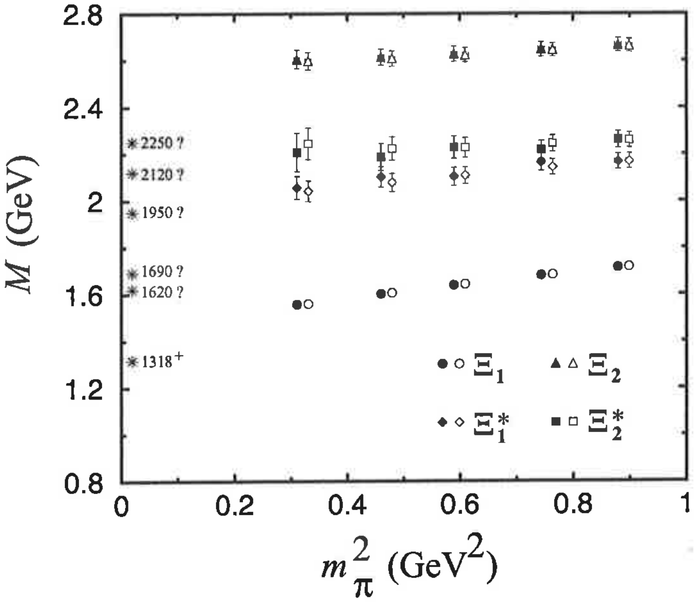

Figure 7.7: As in Fig. 7.5 but for the Ξ baryons. The J^P values of the excited states marked with "?" are undetermined.

for the FLIC action, with the data given in Tables 7.4 and 7.5. The positive (negative) parity states labeled Λ_1 (Λ_1^*) and Λ_2 (Λ_2^*) are constructed from the χ_1^Λ and χ_2^Λ interpolating fields, respectively. The Λ^8 (octet) states are represented by the open symbols, while the isosinglet Λ^c states (made up of terms common to both the octet and singlet fields) are denoted by the filled symbols. The empirical $\Lambda^*(\frac{1}{2}^\pm)$ masses are denoted by asterisks.

A similar pattern of mass splittings is observed to that for the N^*'s in Fig. 7.5. In particular, the negative parity Λ_1^* state (squares) lies $\sim$ 400 MeV above the positive parity Λ_1 ground state (diamonds), for both the Λ^8 and Λ^c fields. There is also clear evidence of a mass splitting between the Λ_1^* (squares) and Λ_2^* (triangles), especially for the Λ^8 field (open symbols), which may indicate sensitivity to the physics responsible for the mass splitting between the negative parity $\Lambda^*(1670)$ and $\Lambda^*(1800)$ states. The fact that the Λ_2^* appears at a higher energy than the Λ_1^* can be attributed to the fact that the latter contains a "diquark" combination coupled to spin 0 (c.f. the masses of the $N_1^*(\frac{1}{2}^-)$ and $N_2^*(\frac{1}{2}^-)$ in Fig. 7.5).

In Figs. 7.9 and 7.10 we compare results obtained from the Λ^8 and Λ^c fields respectively using the two different techniques for extracting masses. Using the naive fitting scheme (open symbols), it is difficult to obtain a mass splitting

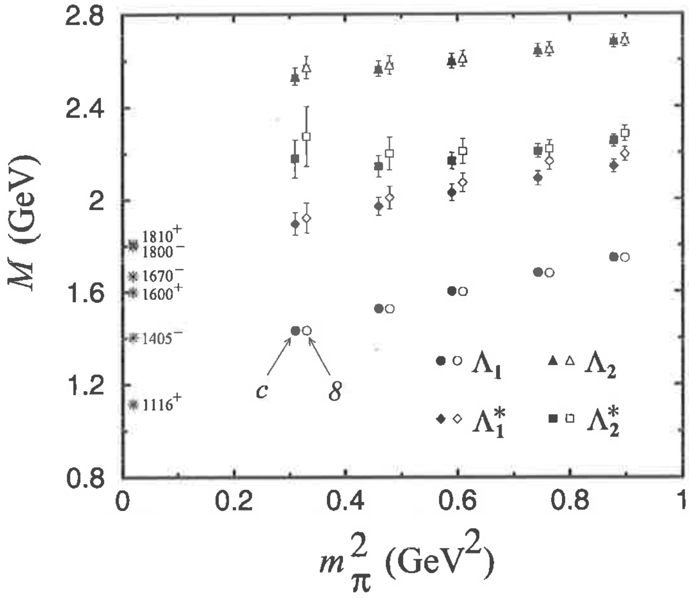

Figure 7.8: Masses of the positive and negative parity Λ states, for the octet Λ^8 (open symbols) and "common" Λ^c (filled symbols) interpolating fields with the FLIC action. The positive (negative) parity states labeled Λ_1 (Λ_1^*) and Λ_2 (Λ_2^*) are the two states obtained from the correlation matrix analysis of the χ_1^Λ and χ_2^Λ interpolating fields. Empirical masses of the low lying $\frac{1}{2}^\pm$ states are indicated by the asterisks.

between Λ_1^* and Λ_2^* for the common interpolating field. Once we perform our correlation matrix analysis however, it is possible to resolve two seperate mass states, as seen by the solid symbols in Fig. 7.10. This may be an indication that the physics responsible for the mass splitting between the negative parity $\Lambda^*(1670)$ and $\Lambda^*(1800)$ states is suppressed in the Λ^c interpolating field. As for the other baryons, there is little evidence that the Λ_2 (circles) has any significant overlap with the first positive parity excited state, $\Lambda^*(1600)$ (c.f. the Roper resonance, $N^*(1440)$, in Fig. 7.5).

While it seems plausible that nonanalyticities in a chiral extrapolation [87] of N_1 and N_1^* results could eventually lead to agreement with experiment, the situation for the $\Lambda^*(1405)$ is not as compelling. Whereas a 150 MeV pion-induced self energy is required for the N_1, N_1^* and Λ_1, 400 MeV is required to approach the empirical mass of the $\Lambda^*(1405)$. This may not be surprising for the octet fields, as the $\Lambda^*(1405)$, being an SU(3) flavor singlet, may not couple strongly to

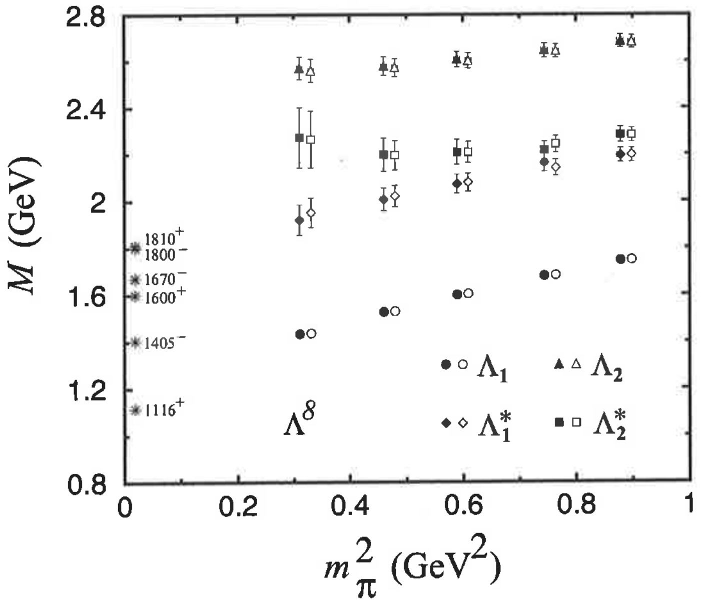

Figure 7.9: As in Fig. 7.5 but for the Λ states obtained using the Λ^8 interpolating field.

an SU(3) octet interpolating field. This large discrepancy suggests that relevant physics may be absent from simulations in the quenched approximation. The behavior of the $\Lambda^*_{1,2}$ states may be modified at small values of the quark mass through nonlinear effects associated with Goldstone boson loops including the strong coupling of the $\Lambda^*(1405)$ to $\Sigma\pi$ and $N\bar{K}$ channels. While some of this coupling will survive in the quenched approximation, generally the couplings are modified and suppressed [80, 104]. It is also interesting to note that the octet Λ_1^* and Λ_2^* masses display a similar behavior to that seen for the Ξ_1^* and Ξ_2^* states, which are dominated by the heavier strange quark. Alternatively, the study of more exotic interpolating fields may indicate the the $\Lambda^*(1405)$ does not couple strongly to χ_1 or χ_2. Investigations at lighter quark masses involving quenched chiral perturbation theory will assist in resolving these issues.

7.5 Summary

Good agreement is obtained between the FLIC and other improved actions, such as the nonperturbatively improved clover [100, 101] and domain wall fermion (DWF) [99] actions, for the nucleon and its chiral partner, with a mass splitting

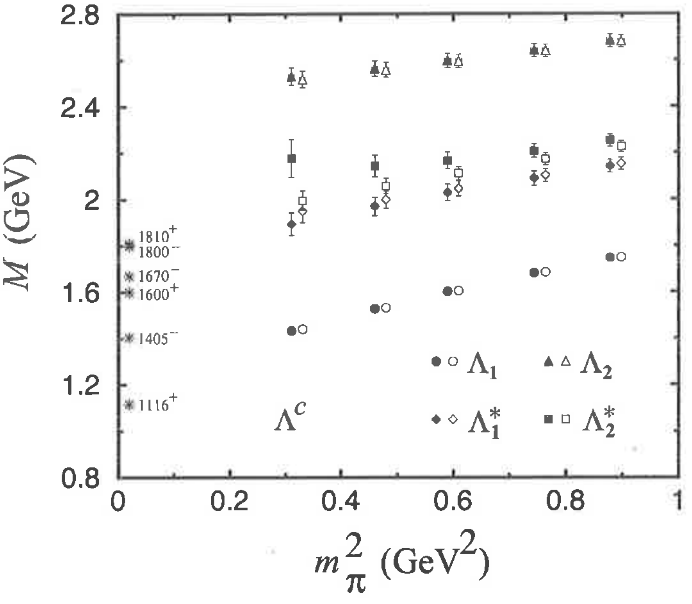

Figure 7.10: As in Fig. 7.5 but for the Λ states obtained using the Λ^c interpolating field.

of $\sim$ 400 MeV. Our results for the $N^*(\frac{1}{2}^-)$ improve on those using the D_{234} [98] and Wilson actions. Despite strong chiral symmetry breaking, the results with the Wilson action are still able to resolve the splitting between the chiral partners of the nucleon. Using the two standard nucleon interpolating fields, we also confirm earlier observations [97] of a mass splitting between the two nearby $\frac{1}{2}^-$ states. We find no evidence of overlap with the $\frac{1}{2}^+$ Roper resonance.

In the strange sector, we have investigated the overlap of various Λ interpolating fields with the low lying $\frac{1}{2}^\pm$ states. Once again a clear mass splitting of $\sim$ 400 MeV between the octet Λ and its parity partner is seen, with some evidence of a mass splitting between the two states primarily associated with the octet Λ_1^* and Λ_2^* interpolating fields. The latter splitting is significantly reduced for the Λ^c correlator, which does not make any assumptions about the SU(3) flavor symmetry properties of the Λ. We find no evidence of strong overlap with the $\frac{1}{2}^+$ "Roper" excitation, $\Lambda^*(1600)$. The empirical mass suppression of the $\Lambda^*(1405)$ is not evident in these quenched QCD simulations, possibly suggesting an important role for the meson cloud of the $\Lambda^*(1405)$ and/or a need for more exotic interpolating fields.

8

Spin 3/2 Baryons

8.1 Introduction

The level orderings in the baryon spectrum and mass splittings between excited baryon multiplets provide important clues to the underlying dynamics governing inter-quark forces and the relevant effective degrees of freedom at low energy [89]. As we saw in Chapter 2, considerable insights into these and other problems of spectroscopy have been gained from QCD-inspired phenomenological models, however, many fundamental questions about the origins of the empirical spectrum remain controversial [81].

The resolution of some of these issues may only be possible with the help of first-principle calculations of the spectrum in lattice QCD — the only method able to provide hadron properties from the fundamental quark and gluon theory. Recent advances in computational capabilities and more efficient algorithms have enabled the first dedicated lattice QCD simulations of the excited states of the nucleon to be undertaken (see Chapter 7 and Refs. [95,97–101,105,106]. Lattice studies of excited hadrons are possible because at the current unphysically large quark masses and finite volumes used in the simulations, most excited states are stable at present. In the future, as lattice simulations extend to smaller quark masses, the effects of excited hadron decays will need to be included [107]. The lattice studies are timely as they complement the first results from the high precision measurements of the N^* spectrum at Jefferson Lab [108].

In the previous chapter we presented our results for the excited nucleon and spin-$\frac{1}{2}$ hyperon spectra using the Fat Link Irrelevant Clover (FLIC) quark action [72] with an $\mathcal{O}(a^2)$-improved gluon action. In this chapter we extend the analysis of Chapter 7 to the spin-$\frac{3}{2}$ sector, and present first results using the FLIC action, in both the isospin-$\frac{1}{2}$ and $\frac{3}{2}$ channels.

Mass splittings between states within SU(3) quark model multiplets provide another important motivation for studying higher spin baryons. Understanding the mass splitting between the $N^*\frac{1}{2}^-(1535)$ and $N^*\frac{3}{2}^-(1520)$, for instance, or between the $\Delta^*\frac{3}{2}^-(1700)$ and $\Delta^*\frac{1}{2}^-(1620)$, can help identify the important mechanisms associated with the hyperfine interactions, or shed light on the spin-orbit force, which has been a central mystery in spectroscopy [93]. In valence quark models, the degeneracy between the $N^*\frac{1}{2}^-$ and $N^*\frac{3}{2}^-$ can be broken by a tensor force associated with mixing between the N^2 and N^4 representations of SU(3) [81], although this generally leaves the $N^*\frac{3}{2}^-$ at a higher energy than the $N^*\frac{1}{2}^-$. On the other hand, a spin-orbit force is necessary to split the $\Delta^*\frac{3}{2}^-$ and $\Delta^*\frac{1}{2}^-$ states. In the Goldstone boson exchange model [88], both of these pairs of states are degenerate. Model-independent analyses in the large N_c limit have found that these mass splittings receive important contributions from operators that do not have simple quark model interpretation [92], such as those simultaneously coupling spin, isospin and orbital angular momentum. Of course, the coefficients of the various operators in such an analysis must be determined phenomenologically. Guidance from lattice QCD is essential.

In the isospin-$\frac{3}{2}$ sector, after applying suitable parity and spin projections, we present the first results for the $\Delta^*\frac{1}{2}^+$ and $\Delta^*\frac{1}{2}^-$ states, as well as the P-wave $\Delta^*\frac{3}{2}^-$. Our results for the $\Delta\frac{3}{2}^+$ are also in good agreement with earlier simulations [109]. A significant advance of this work is the observation of a discernible signal for the $\Delta^*\frac{1}{2}^\pm$ state, which yielded a weak signal in earlier simulations [100, 105]. The lowest excitation of the ground state, namely the $\Delta^*\frac{1}{2}^-$, is found to have a mass $\sim$ 350–400 MeV above the $\Delta\frac{3}{2}^+$, with the $\Delta\frac{3}{2}^-$ slightly heavier. The $\Delta^*\frac{1}{2}^+$ state is found to lie $\sim$ 100–200 MeV above these, although the signal becomes weak at smaller quark masses. This level ordering is consistent with that observed in the empirical mass spectrum.

In the spin-$\frac{3}{2}$ nucleon sector, there is good agreement for the spin-projected $\frac{1}{2}^+$ and $\frac{1}{2}^-$ states with earlier nucleon mass calculations from Chapters 6 and 7 using the standard spin-$\frac{1}{2}$ nucleon interpolating field. Furthermore, we find a good signal for the $N\frac{3}{2}^\pm$ states, with a mass difference of $\sim$ 300 MeV between the spin-$\frac{3}{2}$ parity partners. The $N\frac{1}{2}^-$ and $N\frac{3}{2}^-$ states are nearly degenerate as observed experimentally. However, the $N\frac{3}{2}^-$ lies above the $N\frac{1}{2}^-$ in accord with most constituent quark models.

In Section 8.2 we outline the basic elements of formulating spin-$\frac{3}{2}$ baryons on the lattice, including the choice of interpolating fields and projection operators. A brief preliminary report of states using the formalism developed and presented here appeared in Ref. [110]. In Section 8.3, our results using the FLIC action on a large lattice volume at a fine lattice spacing represent the first quantitative analysis of these states. A summary and remarks about future work are contained in Section 8.4.

8.2 Spin 3/2 Baryons on the Lattice

In this Section the essential elements for a lattice calculation of spin-$\frac{3}{2}$ baryon properties are presented

8.2.1 Spin 3/2 Two-Point Functions

The mass of a spin-$\frac{3}{2}$ baryon on the lattice is obtained from the two-point correlation function $G_{\mu\nu}$ [102, 109],

$$G_{\mu\nu}(t,\vec{p};\Gamma) = \sum_{\vec{x}} e^{-i\vec{p}\cdot\vec{x}}\, \Gamma^{\beta\alpha}\, \langle 0|\, T\left(\chi^{\alpha}_{\mu}(x)\, \overline{\chi}^{\beta}_{\nu}(0)\right) |0\rangle \ , \qquad (8.1)$$

where χ^{α}_{μ} is a spin-$\frac{3}{2}$ interpolating field, Γ is a matrix in Dirac space, α, β are Dirac indices, and μ, ν are Lorentz indices.

In this analysis we consider the following interpolating field for the isospin-$\frac{1}{2}$, spin-$\frac{3}{2}$, positive parity (charge +1) state [111] in the Dirac representation of the γ matrices,

$$\chi^{N}_{\mu} = \epsilon^{abc}\left(u^{Ta}(x)\; C\gamma_5\gamma^{\nu}\; d^{b}(x)\right)\left(g_{\mu\nu} - \frac{1}{4}\gamma_{\mu}\gamma_{\nu}\right)\gamma_5 u^{c}(x) \ , \qquad (8.2)$$

This exact isospin-$\frac{1}{2}$ interpolating field has overlap with both spin-$\frac{3}{2}$ and spin-$\frac{1}{2}$ states and with states of both parities. The resulting correlation function will thus require both spin and parity projection. The quark field operators u and d act at Euclidean space-time point x, C is the charge conjugation matrix, a, b and c are colour labels, and the superscript T denotes the transpose. The charge neutral interpolating field is obtained by interchanging $u \leftrightarrow d$. This interpolating field transforms as a Rarita-Schwinger operator under parity transformations. That is, if the quark field operators transform as

$$\mathcal{P}u(x)\mathcal{P}^{\dagger} = +\gamma_0 u(\tilde{x})\,,$$

where $\tilde{x} = (x_0, -\vec{x})$, and similarly for $d(x)$, then

$$\mathcal{P}\chi^{N}_{\mu}(x)\mathcal{P}^{\dagger} = +\gamma_0 \chi^{N}_{\mu}(\tilde{x}) \ ,$$

and similarly for the Rarita-Schwinger operator

$$\mathcal{P}u_{\mu}(x)\mathcal{P}^{\dagger} = +\gamma_0 u_{\mu}(\tilde{x}) \ . \qquad (8.3)$$

The computational cost of evaluating each of the Lorentz combinations in Eq. (8.2) is relatively high — about 100 times that for the ground state nucleon

[97]. Consequently, in order to maximize statistics in our analysis we consider only the leading term proportional to $g_{\mu\nu}$,

$$\chi_\mu^N \longrightarrow \epsilon^{abc}\left(u^{Ta}(x)\ C\gamma_5\gamma_\mu\ d^b(x)\right)\gamma_5 u^c(x)\ . \tag{8.4}$$

In order to show that the interpolating field defined in Eq. (8.4) has isospin-$\frac{1}{2}$, we first consider the standard proton interpolating field from Eq. (7.7),

$$\chi^p = \epsilon^{abc}(u^{Ta}C\gamma_5 d^b)u^c, \tag{8.5}$$

which we know to have isospin-$\frac{1}{2}$. Applying the isospin raising operator, I^+, on χ^p one finds,

$$\begin{aligned} I^+\chi^p &= \epsilon^{abc}(u^{Ta}C\gamma_5 u^b)u^c \\ &= \epsilon^{abc}(u^{Ta}C\gamma_5 u^b)^T u^c \\ &= -\epsilon^{abc}(u^{Tb}\gamma_5 C^T u^a)u^c \\ &= \epsilon^{abc}(u^{Ta}\gamma_5 C^T u^b)u^c \\ &= -\epsilon^{abc}(u^{Ta}C\gamma_5 u^b)u^c \\ &= 0. \end{aligned}$$

Similarly, for the interpolating field defined in Eq. (8.4), one has

$$\begin{aligned} I^+\chi_\mu^N &= \epsilon^{abc}(u^{Ta}C\gamma_5\gamma_\mu u^b)\gamma_5 u^c \\ &= \epsilon^{abc}(u^{Ta}C\gamma_5\gamma_\mu u^b)^T\gamma_5 u^c \\ &= -\epsilon^{abc}(u^{Tb}\gamma_\mu^T\gamma_5 C^T u^a)\gamma_5 u^c \\ &= \epsilon^{abc}(u^{Ta}CC\gamma_\mu^T CC\gamma_5 C^T u^b)\gamma_5 u^c \\ &= \epsilon^{abc}(u^{Ta}C\gamma_\mu\gamma_5 u^b)\gamma_5 u^c \\ &= -\epsilon^{abc}(u^{Ta}C\gamma_5\gamma_\mu u^b)\gamma_5 u^c \\ &= 0, \end{aligned}$$

where we have used the representation independent identities $C\gamma_\mu C^{-1} = -\gamma_\mu^T$, $C\gamma_5 C^{-1} = \gamma_5^T$ and the identities which hold in the Dirac representation $C^T = C^\dagger = C^{-1} = -C$ with $C = i\gamma_2\gamma_0$ and $\gamma_5^T = \gamma_5$.

We note that $\bar{\chi}_\mu^N$ corresponding to χ_μ^N in Eq. (8.4) is

$$\begin{aligned} \bar{\chi}_\mu^N = \chi_\mu^{N\dagger}\gamma_0 &= -\bar{u}\gamma_5(\bar{d}\gamma_0\gamma_\mu^\dagger\gamma_0\gamma_0\gamma_5^\dagger C^\dagger\gamma_0\bar{u}^T) \\ &= +\bar{u}\gamma_5(\bar{d}\gamma_\mu\gamma_5 C\bar{u}^T), \end{aligned} \tag{8.6}$$

so that

$$\begin{aligned} \chi_\mu^N\bar{\chi}_\nu^N = \quad & \epsilon^{abc}\epsilon^{a'b'c'}(u_\alpha^{Ta}[C\gamma_5\gamma_\mu]_{\alpha\beta}d_\beta^b)\gamma_5 u_\gamma^c\bar{u}_{\gamma'}^{c'}\gamma_5(\bar{d}_{\beta'}^{b'}[\gamma_\nu\gamma_5 C]_{\beta'\alpha'}\bar{u}_{\alpha'}^{Ta'}) \\ & \rightarrow \gamma_5 S_u\gamma_5 \mathrm{tr}\left[\gamma_5 S_u\gamma_5\left(C\gamma_\mu S_d\gamma_\nu C\right)^T\right] + \gamma_5 S_u\gamma_5\left(C\gamma_\mu S_d\gamma_\nu C\right)^T\gamma_5 S_u\gamma_5. \end{aligned} \tag{8.7}$$

where the last line is the result achieved after doing the Grassman integration over the quark fields with the quark fields being replaced by all possible pairwise contractions.

In deriving the Δ interpolating fields, it is simplest to begin with the state containing only valence u quarks, namely the Δ^{++}. The commonly used interpolating field for the Δ^{++} resonance is given by [111],

$$\chi_\mu^{\Delta^{++}}(x) = \epsilon^{abc} \left(u^{Ta}(x)\, C\gamma_\mu\, u^b(x) \right) u^c(x) \ , \tag{8.8}$$

which also transforms as pseudovector under parity. The interpolating field for a Δ^+ state can be similarly constructed [109],

$$\begin{aligned} \chi_\mu^{\Delta^+}(x) \ = \ & \frac{1}{\sqrt{3}} \epsilon^{abc} \Big[2 \left(u^{Ta}(x)\, C\gamma_\mu\, d^b(x) \right) u^c(x) \\ & \qquad + \left(u^{Ta}(x)\, C\gamma_\mu\, u^b(x) \right) d^c(x) \Big] \ . \end{aligned} \tag{8.9}$$

The correlation function is

$$\begin{aligned} \chi_\mu^{\Delta^+} \overline{\chi}_\nu^{\Delta^+} \ = \ & \frac{1}{3}\, \epsilon^{abc} \epsilon^{a'b'c'} \Big\{ 4 S_u^{aa'}\, \gamma_\nu\, C S_u^{Tbb'} C\, \gamma_\mu\, S_d^{cc'} + 4 S_u^{aa'}\, \gamma_\nu\, C S_d^{Tbb'} C\, \gamma_\mu\, S_u^{cc'} \\ & + 4 S_d^{aa'}\, \gamma_\nu\, C S_u^{Tbb'} C\, \gamma_\mu\, S_u^{cc'} + 2 S_u^{aa'} \operatorname{tr} \left[\gamma_\nu\, C S_u^{Tbb'} C\, \gamma_\mu\, S_d^{cc'} \right] \\ & + 2 S_u^{aa'} \operatorname{tr} \left[\gamma_\nu\, C S_d^{Tbb'} C\, \gamma_\mu\, S_u^{cc'} \right] + 2 S_d^{aa'} \operatorname{tr} \left[\gamma_\nu\, C S_u^{Tbb'} C\, \gamma_\mu\, S_u^{cc'} \right] \Big\} , \end{aligned} \tag{8.10}$$

Interpolating fields for other decuplet baryons are obtained by appropriate substitutions of $u(x),\ d(x) \ \rightarrow \ u(x),\ d(x)$ or $s(x)$ fields.

To project a pure spin-$\frac{3}{2}$ state from the correlation function $G_{\mu\nu}$, one needs to use an appropriate spin-$\frac{3}{2}$ projection operator [112],

$$P_{\mu\nu}^{3/2}(p) = g_{\mu\nu} - \frac{1}{3}\gamma_\mu\gamma_\nu - \frac{1}{3p^2} \left(\gamma \cdot p\, \gamma_\mu\, p_\nu + p_\mu\, \gamma_\nu\, \gamma \cdot p \right) \ . \tag{8.11}$$

The corresponding spin-$\frac{1}{2}$ state can be projected by applying the projection operator

$$P_{\mu\nu}^{1/2} = g_{\mu\nu} - P_{\mu\nu}^{3/2} \ . \tag{8.12}$$

To use this operator and retain all Lorentz components, one must calculate the full 4×4 matrix in Dirac and Lorentz space. However, to extract a mass, only one pair of Lorentz indicies is needed, reducing the amount of calculations required by a factor of four. We calculate the third row of the Lorentz matrix and use the projection,

$$G_{33}^s = \sum_{\mu=1}^{4} G_{3\mu}\, g^{\mu\nu}\, P_{\nu 3}^s \ , \tag{8.13}$$

to extract the desired spin states, $s = \frac{1}{2}$ or $\frac{3}{2}$. Following spin projection, the projected correlation function, G^s_{33}, still contains positive and negative parity states.

We use an improved unbiased estimator obtained by summing both U and U^* configurations which occur with equal weight. The net effect is that $G_{\mu\nu}$ is purely real if μ and ν are both either spatial indicies or temperal indicies. If one is a spatial index and the other temporal, then $G_{\mu\nu}$ is purely imaginary (see Appendix C). After spin projection however, $G^s_{\mu\nu}$ is purely real.

8.2.2 Baryon Level

The interpolating field defined in Eq. (8.4) has overlap with both spin-$\frac{3}{2}$ and spin-$\frac{1}{2}$ states with positive and negative parity. The field χ_μ transforms as a pseudovector under parity, as does the Rarita-Schwinger spinor, u_μ. Thus the overlap of χ_μ with baryons is as follows

$$\begin{aligned}
\langle 0|\chi_\mu|N^{\frac{3}{2}+}(p,s)\rangle &= \lambda_{3/2^+}\sqrt{\frac{M_{3/2^+}}{E_{3/2^+}}}\, u_\mu(p,s)\ , && \text{(8.14a)}\\
\langle 0|\chi_\mu|N^{\frac{3}{2}-}(p,s)\rangle &= \lambda_{3/2^-}\sqrt{\frac{M_{3/2^-}}{E_{3/2^-}}}\, \gamma_5 u_\mu(p,s)\ , && \text{(8.14b)}\\
\langle 0|\chi_\mu|N^{\frac{1}{2}+}(p,s)\rangle &= (\alpha_{1/2^+}p_\mu + \beta_{1/2^+}\gamma_\mu)\sqrt{\frac{M_{1/2^+}}{E_{1/2^+}}}\, \gamma_5 u(p,s)\ , && \text{(8.14c)}\\
\langle 0|\chi_\mu|N^{\frac{1}{2}-}(p,s)\rangle &= (\alpha_{1/2^-}p_\mu + \beta_{1/2^-}\gamma_\mu)\sqrt{\frac{M_{1/2^-}}{E_{1/2^-}}}\, u(p,s)\ , && \text{(8.14d)}
\end{aligned}$$

where the factors λ_B, α_B, β_B denote the coupling strengths of the interpolating field χ_μ to the baryon B, and $E_B = \sqrt{\vec{p}^{\,2} + M_B^2}$ is the energy. For the expressions in Eqs. (8.14c) and (8.14d), we note that the spatial components of momentum, p_i, transform as a vector under parity and commute with γ_0, whereas the γ_i do not change sign under parity but anticommute with γ_0. Hence the right-hand-side of Eq. (8.14c) also transforms as a pseudovector under parity in accord with χ_μ.

Similar expressions can also be written for $\bar{\chi}_\mu$,

$$\begin{aligned}
\langle N^{\frac{3}{2}+}(p,s)|\bar{\chi}_\mu|0\rangle &= \lambda^*_{3/2^+}\sqrt{\frac{M_{3/2^+}}{E_{3/2^+}}}\;\bar{u}_\mu(p,s)\;, && (8.15a)\\
\langle N^{\frac{3}{2}-}(p,s)|\bar{\chi}_\mu|0\rangle &= -\lambda^*_{3/2^-}\sqrt{\frac{M_{3/2^-}}{E_{3/2^-}}}\;\bar{u}_\mu(p,s)\gamma_5\;, && (8.15b)\\
\langle N^{\frac{1}{2}+}(p,s)|\bar{\chi}_\mu|0\rangle &= -\sqrt{\frac{M_{1/2^+}}{E_{1/2^+}}}\;\bar{u}(p,s)\gamma_5(\alpha^*_{1/2^+}p_\mu+\beta^*_{1/2^+}\gamma_\mu)\;, && (8.15c)\\
\langle N^{\frac{1}{2}-}(p,s)|\bar{\chi}_\mu|0\rangle &= \sqrt{\frac{M_{1/2^-}}{E_{1/2^-}}}\;\bar{u}(p,s)(\alpha^*_{1/2^-}p_\mu+\beta^*_{1/2^-}\gamma_\mu)\;. && (8.15d)
\end{aligned}$$

Note that we are assuming identical sinks and sources in these equations. In our calculations we use a smeared source and a point sink in which case λ^*, α^* and β^* are no longer complex conjugates of λ, α and β and are instead replaced by $\overline{\lambda}$, $\overline{\alpha}$ and $\overline{\beta}$.

We are now in a position to find the form of Eq. (8.1) after we insert a complete set of intermediate states $\{|B_i(p,s)\rangle\}$. The contribution to Eq. (8.1) from each intermediate state considered is given by

$$\begin{aligned}
&\langle 0|\chi_\mu|N^{\frac{3}{2}+}(p,s)\rangle\langle N^{\frac{3}{2}+}(p,s)|\bar{\chi}_\nu|0\rangle\\
&\quad= +\lambda_{3/2^+}\overline{\lambda}_{3/2^+}\frac{M_{3/2^+}}{E_{3/2^+}}u_\mu(p,s)\bar{u}_\nu(p,s)\\
&\quad= -\lambda_{3/2^+}\overline{\lambda}_{3/2^+}\frac{M_{3/2^+}}{E_{3/2^+}}\frac{(\gamma\cdot p+M_{3/2^+})}{2M_{3/2^+}}\left\{g_{\mu\nu}-\frac{1}{3}\gamma_\mu\gamma_\nu-\frac{2p_\mu p_\nu}{3M^2_{3/2^+}}+\frac{p_\mu\gamma_\nu-p_\nu\gamma_\mu}{3M_{3/2^+}}\right\},\\
&\langle 0|\chi_\mu|N^{\frac{3}{2}-}(p,s)\rangle\langle N^{\frac{3}{2}-}(p,s)|\bar{\chi}_\nu|0\rangle\\
&\quad= -\lambda_{3/2^-}\overline{\lambda}_{3/2^-}\frac{M_{3/2^-}}{E_{3/2^-}}\gamma_5u_\mu(p,s)\bar{u}_\nu(p,s)\gamma_5\\
&\quad= -\lambda_{3/2^-}\overline{\lambda}_{3/2^-}\frac{M_{3/2^-}}{E_{3/2^-}}\frac{(\gamma\cdot p-M_{3/2^-})}{2M_{3/2^-}}\left\{g_{\mu\nu}-\frac{1}{3}\gamma_\mu\gamma_\nu-\frac{2p_\mu p_\nu}{3M^2_{3/2^-}}-\frac{p_\mu\gamma_\nu-p_\nu\gamma_\mu}{3M_{3/2^-}}\right\},\\
&\langle 0|\chi_\mu|N^{\frac{1}{2}+}(p,s)\rangle\langle N^{\frac{1}{2}+}(p,s)|\bar{\chi}_\nu|0\rangle\\
&\quad= -\frac{M_{1/2^+}}{E_{1/2^+}}(\alpha_{1/2^+}p_\mu+\beta_{1/2^+}\gamma_\mu)\gamma_5\frac{\gamma\cdot p+M_{1/2^+}}{2M_{1/2^+}}\gamma_5(\overline{\alpha}_{1/2^+}p_\nu+\overline{\beta}_{1/2^+}\gamma_\nu),\\
&\langle 0|\chi_\mu|N^{\frac{1}{2}-}(p,s)\rangle\langle N^{\frac{1}{2}-}(p,s)|\bar{\chi}_\nu|0\rangle\\
&\quad= \frac{M_{1/2^-}}{E_{-/2^+}}(\alpha_{1/2^-}p_\mu+\beta_{1/2^-}\gamma_\mu)\frac{\gamma\cdot p+M_{1/2^-}}{2M_{1/2^-}}(\overline{\alpha}_{1/2^-}p_\nu+\overline{\beta}_{1/2^-}\gamma_\nu).
\end{aligned}$$

To reduce computational expense, we consider the specific case when $\mu=\nu=3$ and in order to extract masses we require $\vec{p}=(0,0,0)$. In this case we have the simple expressions

$$
\begin{aligned}
\langle 0|\chi_3|N^{\frac{3}{2}+}(p,s)\rangle\langle N^{\frac{3}{2}+}(p,s)|\bar{\chi}_3|0\rangle &= \lambda_{3/2^+}\overline{\lambda}_{3/2^+}\frac{2}{3}\left(\frac{\gamma_0 M_{3/2^+}+M_{3/2^+}}{2M_{3/2^+}}\right), && (8.16\text{a})\\
\langle 0|\chi_3|N^{\frac{3}{2}-}(p,s)\rangle\langle N^{\frac{3}{2}-}(p,s)|\bar{\chi}_3|0\rangle &= \lambda_{3/2^-}\overline{\lambda}_{3/2^-}\frac{2}{3}\left(\frac{\gamma_0 M_{3/2^-}-M_{3/2^-}}{2M_{3/2^-}}\right), && (8.16\text{b})\\
\langle 0|\chi_3|N^{\frac{1}{2}+}(p,s)\rangle\langle N^{\frac{1}{2}+}(p,s)|\bar{\chi}_3|0\rangle &= -\beta_{1/2^+}\overline{\beta}_{1/2^+}\gamma_3\gamma_5\frac{\gamma_0 M_{1/2^+}+M_{1/2^+}}{2M_{1/2^+}}\gamma_5\gamma_3\\
&= +\beta_{1/2^+}\overline{\beta}_{1/2^+}\left(\frac{\gamma_0 M_{1/2^+}+M_{1/2^+}}{2M_{1/2^+}}\right), && (8.16\text{c})\\
\langle 0|\chi_3|N^{\frac{1}{2}-}(p,s)\rangle\langle N^{\frac{1}{2}-}(p,s)|\bar{\chi}_3|0\rangle &= \beta_{1/2^-}\overline{\beta}_{1/2^-}\gamma_3\frac{\gamma_0 M_{1/2^-}+M_{1/2^-}}{2M_{1/2^-}}\gamma_3\\
&= +\beta_{1/2^-}\overline{\beta}_{1/2^-}\left(\frac{\gamma_0 M_{1/2^-}-M_{1/2^-}}{2M_{1/2^-}}\right) && (8.16\text{d})
\end{aligned}
$$

Therefore, in an analogous procedure to that used in Ref. [106], when a fixed boundary condition is used in the time direction, positive and negative parity states are obtained by taking the trace of the spin-projected correlation function, G^s_{33}, in Eq. (8.13) with the operator $\Gamma = \Gamma_\pm$, where

$$\Gamma_\pm = \frac{1}{2}(1 \pm \gamma_4)\,. \tag{8.17}$$

The positive parity states propagate in the (1,1) and (2,2) elements of the Dirac matrix, while negative parity states propagate in the (3,3) and (4,4) elements for both spin-$\frac{1}{2}$ and spin-$\frac{3}{2}$ projected states.

8.3 Results

The analysis is based on a sample of 392 configurations. For the gauge fields, a mean-field improved plaquette plus rectangle action (Eq. (3.15)) is used. The simulations are performed on a $16^3 \times 32$ lattice at $\beta = 4.60$, which corresponds to a lattice spacing of $a = 0.122(2)$ fm set by the string tension [57] with $\sqrt{\sigma} =$ 440 MeV. For the quark fields, the FLIC [72] action (Eq. (6.4)) is implemented. The fat links were created with $n = 4$ smearing sweeps and a smearing fraction, $\alpha = 0.7$.

A fixed boundary condition in the time direction is used for the fermions by setting $U_t(\vec{x}, N_t) = 0 \ \forall \ \vec{x}$ in the hopping terms of the fermion action, with periodic boundary conditions imposed in the spatial directions. Gauge-invariant gaussian smearing [76] in the spatial dimensions is applied at the source to increase the overlap of the interpolating operators with the ground states.

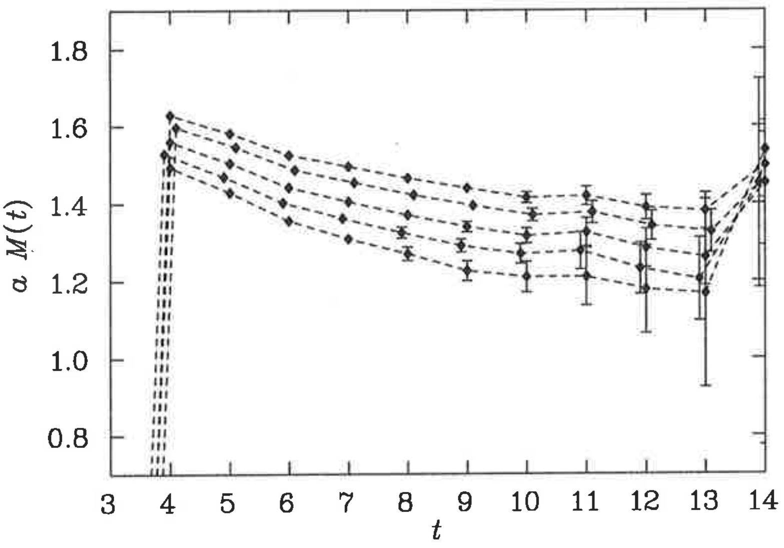

Figure 8.1: Effective mass plot for the $N\frac{3}{2}^-$ state using the FLIC action, from 392 configurations. The five sets of points correspond to the κ values listed in Table 8.1, with κ increasing from top down.

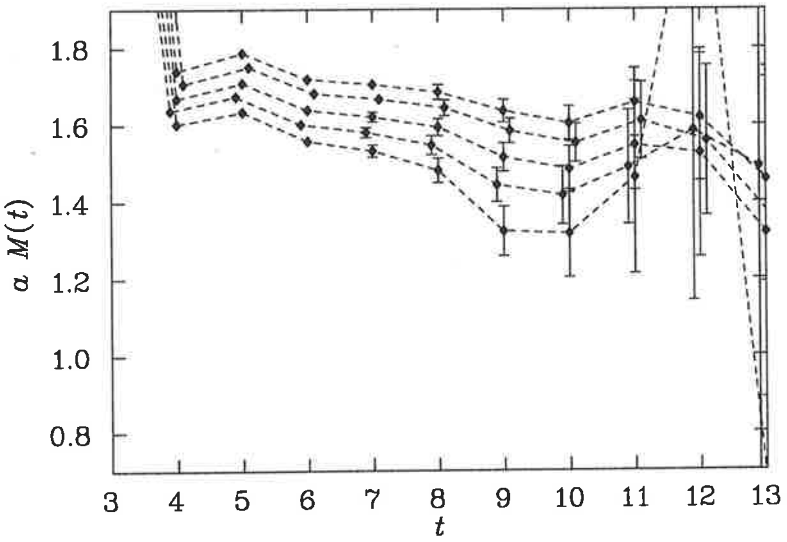

Figure 8.2: As in Fig. 8.1, but for the $N\frac{3}{2}^+$ state.

κ	$m_\pi\, a$	$M_{N\frac{1}{2}^+}\, a$	$M_{N\frac{1}{2}^-}\, a$	$M_{N\frac{3}{2}^+}\, a$	$M_{N\frac{3}{2}^-}\, a$
0.1260	0.5767(11)	1.102(8)	1.412(13)	1.628(34)	1.410(16)
0.1266	0.5305(12)	1.043(9)	1.369(14)	1.577(38)	1.365(19)
0.1273	0.4712(15)	0.970(13)	1.317(17)	1.510(44)	1.312(24)
0.1279	0.4164(15)	0.905(18)	1.271(21)	1.440(53)	1.264(32)
0.1286	0.3421(18)	0.829(32)	1.220(31)	1.329(74)	1.206(49)

Table 8.1: Masses of the π, $N\frac{1}{2}^{\pm}$ and $N\frac{3}{2}^{\pm}$, for several values of κ obtained from the spin-$\frac{3}{2}$ interpolating field, for the FLIC action with 4 sweeps of smearing at $\alpha = 0.7$. Here the value of $\kappa_{\rm cr}$ is $\kappa_{\rm cr} = 0.1300$. A string tension analysis provides $a = 0.122(2)$ fm for $\sqrt{\sigma} = 440$ MeV.

In the analysis we use five values of κ, as indicated in Table 8.1. Extrapolation to $m_\pi^2 = 0$ gives $\kappa_{\rm cr} = 0.1300$. Figure 8.1 shows the effective mass plot for the $N\frac{3}{2}^-$ state for the five κ values used as a function of Euclidean time obtained after performing spin and parity projections on the correlation functions calculated using the interpolating field in Eq. (8.4). We find a good signal for this state up until time slice 13 after which the signal is lost in noise. The effective mass for this state exhibits good plateau behaviour and a good value of the covariance-matrix based $\chi^2/N_{\rm DF}$ is obtained when one fits in the time fitting window of $t = 10$–13 (recall, the source is at $t = 3$). Typically, one finds $\chi^2/N_{\rm DF} \approx 1$ and $\chi^2/N_{\rm DF} < 1.5$ throughout. After performing spin and parity projections to extract the $N\frac{3}{2}^+$ state from the interpolating field in Eq. (8.4), one finds the effective mass plot to be a little noisier, as shown in Fig. 8.2. There is, however, sufficient information here to extract a mass, and a good value of $\chi^2/N_{\rm DF}$ is obtained when one fits in the small time fitting window of $t = 9$–11.

The interpolating field defined in Eq. (8.4) also has overlap with spin-$\frac{1}{2}$ states of both parities. After performing a spin-$\frac{1}{2}$ projection on the correlation functions, we isolate the $N\frac{1}{2}^+$ and $N\frac{1}{2}^-$ states via parity projection and plot the effective masses in Figs. 8.3 and 8.4 respectively. The $N\frac{1}{2}^+$ state suffers contamination from excited states as seen by the long Euclidean time evolution required to reach plateau in Fig. 8.3. A good value of $\chi^2/N_{\rm DF}$ is obtained as long as we fit after time slice 12. For this reason, we use time slices 13–16 to obtain a mass for the $N\frac{1}{2}^+$ state. However, for the $N\frac{1}{2}^-$ state, a plateau is seen at early Euclidean times and a good value of $\chi^2/N_{\rm DF}$ is obtained on time slices 8–11.

The extracted masses of the $N\frac{3}{2}^{\pm}$ and $N\frac{1}{2}^{\pm}$ states are given in Table 8.1 and are displayed in Fig. 8.5 as a function of m_π^2. Earlier results for the $N\frac{1}{2}^{\pm}$ states using the standard spin-$\frac{1}{2}$ interpolating field [72, 106] from Eq. (7.7) are also

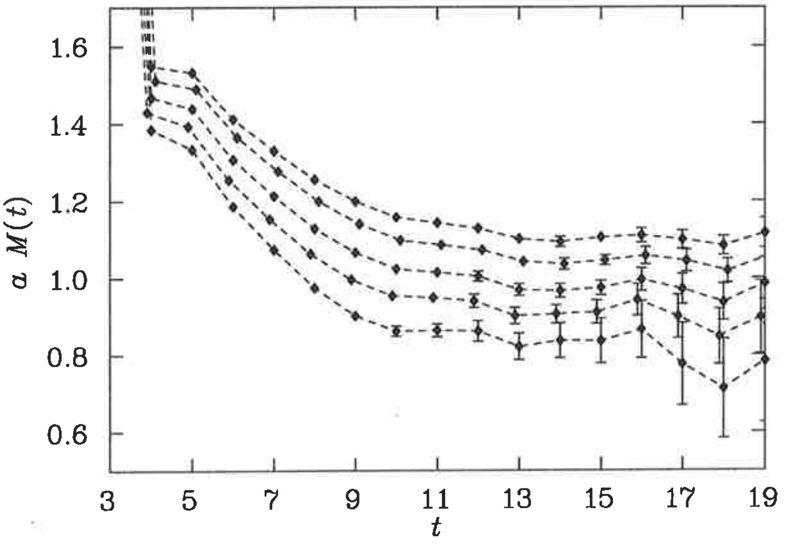

Figure 8.3: As in Fig. 8.1, but for the $N\frac{1}{2}^{+}$ state.

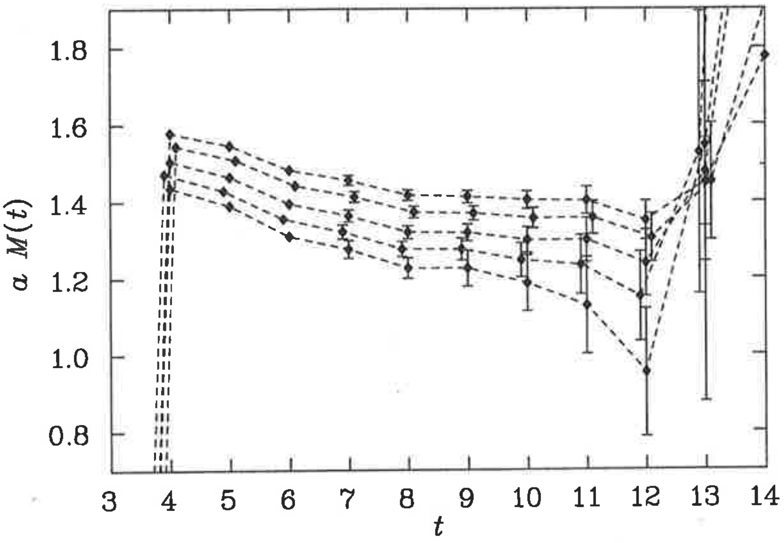

Figure 8.4: As in Fig. 8.1, but for the $N\frac{1}{2}^{-}$ state.

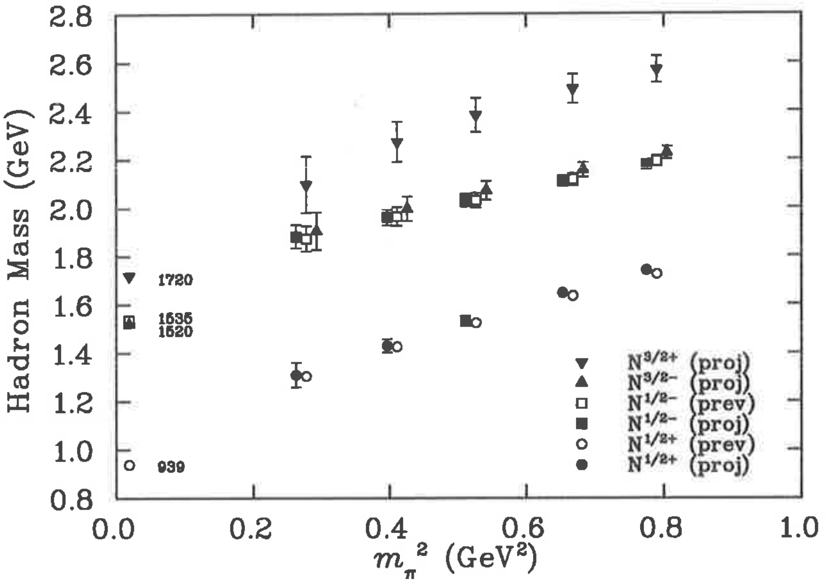

Figure 8.5: Masses of the spin projected $N\frac{3}{2}^-$ (filled triangles), $N\frac{3}{2}^+$ (filled inverted triangles), $N\frac{1}{2}^+$ (filled circles), and $N\frac{1}{2}^-$ (filled squares) states. For comparison, previous results from the direct calculation of the $N\frac{1}{2}^+$ (open circles) and $N\frac{1}{2}^-$ (open squares) from Ref. [106] are also shown. The empirical values of the masses of the $N\frac{1}{2}^+(939)$, $N\frac{1}{2}^-(1535)$, $N\frac{3}{2}^-(1520)$ and $N\frac{3}{2}^+(1720)$ are shown on the left-hand-side at the physical pion mass.

shown with open symbols in Fig. 8.5 for reference. It is encouraging to note the excellent agreement between the spin-projected $\frac{1}{2}^\pm$ states obtained from the spin-$\frac{3}{2}$ interpolating field in Eq. (8.4) and the earlier $\frac{1}{2}^\pm$ results from the same gauge field configurations. To study this agreement more accurately, we consider the ratio of effective masses obtained for each jackknife subensemble. This provides us with a correlated ratio and we find the ratio to be one within statistical uncertainties. We also observe that the $N\frac{3}{2}^-$ state has approximately the same mass as the $N\frac{1}{2}^-$ state which is consistent with the experimentally observed masses. However, our quenched simulations at heavy quark masses puts the $N\frac{3}{2}^-$ state to be slightly heavier than the $N\frac{1}{2}^-$ state which is consistent with

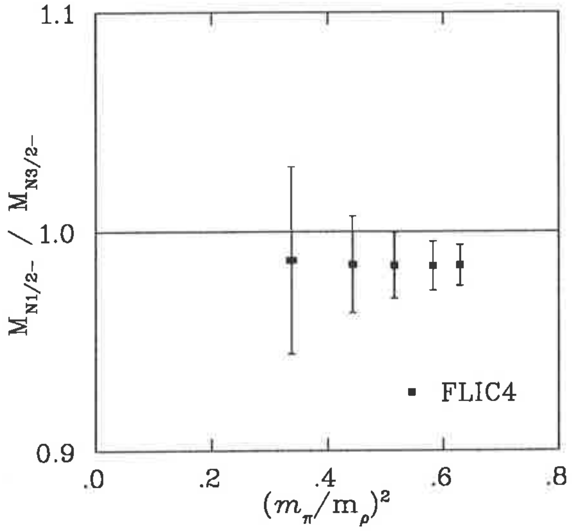

Figure 8.6: Spin projected $N\frac{1}{2}^-/N\frac{3}{2}^-$ mass ratio from the spin-$\frac{3}{2}$ interpolating field defined in Eq. (8.4).

valence quark models. At lighter quark masses the situation is not as clear due to larger, overlapping error bars. To study this mass difference more accurately, we again calculate the correlated ratio of effective masses obtained after appropriate spin and parity projections. This ratio is shown in Fig. 8.6 and we see that $M_{N\frac{1}{2}^-} < M_{N\frac{3}{2}^-}$ for the three heaviest masses. There is little more than a hint that the ratio may become greater than one at the physical mass. The results for the $N\frac{3}{2}^-$ state in Fig. 8.5 indicate a clear mass splitting between the $N\frac{3}{2}^+$ and $N\frac{3}{2}^-$ states obtained from the spin-$\frac{3}{2}$ interpolating field, with a mass difference around 300 MeV. This is slightly larger than the experimentally observed mass difference of 200 MeV.

Turning now to the isospin-$\frac{3}{2}$ sector, the effective mass plot for the $\Delta\frac{3}{2}^+$ state using the interpolating field given in Eq. (8.8) is shown in Figure 8.7 for the five κ values used. An excellent signal is clearly visible, and a good value of the covariance-matrix based $\chi^2/N_{\rm DF}$ is obtained by fitting time slices $t = 11$–14 following the source at $t = 3$. For the effective mass of the negative parity $\Delta\frac{3}{2}^-$, shown in Fig. 8.8, the signal is quite good up to time slice 11-12, but is lost in noise after time slice 12. Time slices $t = 9$–12 provide a fitting window with an

κ	$M_{\Delta\frac{3}{2}^+} a$	$M_{\Delta\frac{3}{2}^-} a$	$M_{\Delta\frac{1}{2}^+} a$	$M_{\Delta\frac{1}{2}^-} a$
0.1260	1.198(8)	1.469(15)	1.643(109)	1.476(34)
0.1266	1.153(9)	1.429(17)	1.604(107)	1.432(41)
0.1273	1.101(12)	1.385(21)	1.561(106)	1.387(54)
0.1279	1.057(15)	1.353(27)	1.530(109)	1.351(76)
0.1286	1.006(22)	1.331(43)	1.502(119)	1.301(126)

Table 8.2: As in Table 8.1, but for the corresponding $\Delta\frac{3}{2}^+$, $\Delta\frac{3}{2}^-$, $\Delta\frac{1}{2}^-$ and $\Delta\frac{1}{2}^+$ masses.

acceptable value of $\chi^2/N_{\rm DF}$.

The results for the $\Delta\frac{3}{2}^+$ and $\Delta\frac{3}{2}^-$ masses are shown in Fig. 8.9 as a function of m_π^2. The trend of the $\Delta\frac{3}{2}^+$ data points with decreasing m_q is clearly towards the $\Delta(1232)$, although some nonlinearity with m_π^2 is expected near the chiral limit [87]. The mass of the $\Delta\frac{3}{2}^-$ lies some 500 MeV above that of its parity partner, although with somewhat larger errors, as expected from the effective mass plots in Figs. 8.7 and 8.8.

After performing a spin projection to extract the $\Delta\frac{1}{2}^\pm$ states, a discernible, but noisy, signal is detected. This indicates that the interpolating field in Eq. (8.8) has only a small overlap with spin-$\frac{1}{2}$ states. However, with 392 configurations we are able to extract a mass for the spin-$\frac{1}{2}$ states at early times, shown in Fig. 8.9. Here we see the larger error bars associated with the $\Delta\frac{1}{2}^\pm$ states. The lowest excitation of the ground state, namely the $\Delta\frac{1}{2}^-$, has a mass $\sim$ 350–400 MeV above the $\Delta\frac{3}{2}^+$, with the $\Delta\frac{3}{2}^-$ possibly appearing heavier. The $\Delta\frac{1}{2}^+$ state is found to lie $\sim$ 100–200 MeV above these, although the signal becomes weak at smaller quark masses. This level ordering is consistent with that observed in the empirical mass spectrum.

The $N\frac{1}{2}^-$ and $\Delta\frac{1}{2}^-$ states will decay to $N\pi$ in S-wave even in the quenched approximation [104]. For all quark masses considered here, with the possible exception of the lightest quark, this decay channel is closed for the nucleon. While there may be some spectral strength in the decay mode, we are unable to separate it from the resonant spectral strength.

The $N\frac{3}{2}^+$ and $\Delta\frac{1}{2}^+$ states will decay to $N\pi$ in P wave, while $N\frac{3}{2}^-$ and $\Delta\frac{3}{2}^-$ states will decay to $N\pi$ in D-wave. Since the decay products of each of these states must then have equal and opposite momentum and energy given by

$$E^2 = M^2 + \left(\frac{2\pi}{aL}\right)^2 ,$$

these states are stable on our lattice.

8.4 Summary

Clear signals are obtained for both the spin-projected $N\frac{3}{2}^{\pm}$ and $N\frac{1}{2}^{\pm}$ states from a spin-$\frac{3}{2}$ interpolating field. In particular, the $\frac{1}{2}^{\pm}$ states are in good agreement with earlier simulations of the nucleon mass and its parity partner using the standard spin-$\frac{1}{2}$ interpolating field. We find the $N\frac{3}{2}^{-}$ state to lie at a similar energy level to the $N\frac{1}{2}^{-}$, consistent with experiment, but with a slightly heavier mass, consistent with valence quark models. We also find a mass difference of $\sim$ 300 MeV between the spin-$\frac{3}{2}$, isospin-$\frac{1}{2}$ parity partners, slightly larger than the experimentally observed difference of 200 MeV.

For isospin-$\frac{3}{2}$ baryons, good agreement is found with earlier calculations for the Δ ground state, and clear mass splittings between the ground state and its parity partner are observed after suitable spin and parity projections. We obtain a signal for the $\Delta\frac{1}{2}^{\pm}$ states and the level ordering is consistent with that observed in the empirical mass spectrum.

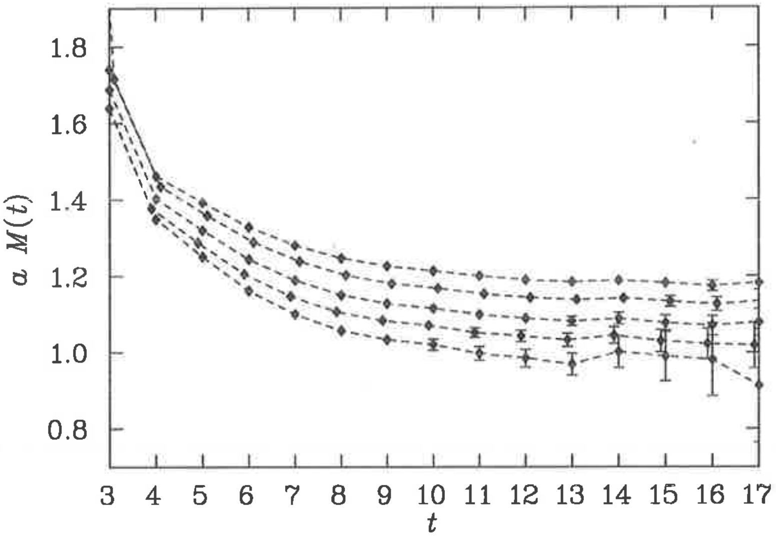

Figure 8.7: Effective mass plot for the $\Delta\frac{3}{2}^{+}$ state using the FLIC action with 4 sweeps of smearing at $\alpha = 0.7$ from 392 configurations. The five sets of points correspond to the κ values listed in Table 8.2, with κ increasing from top down.

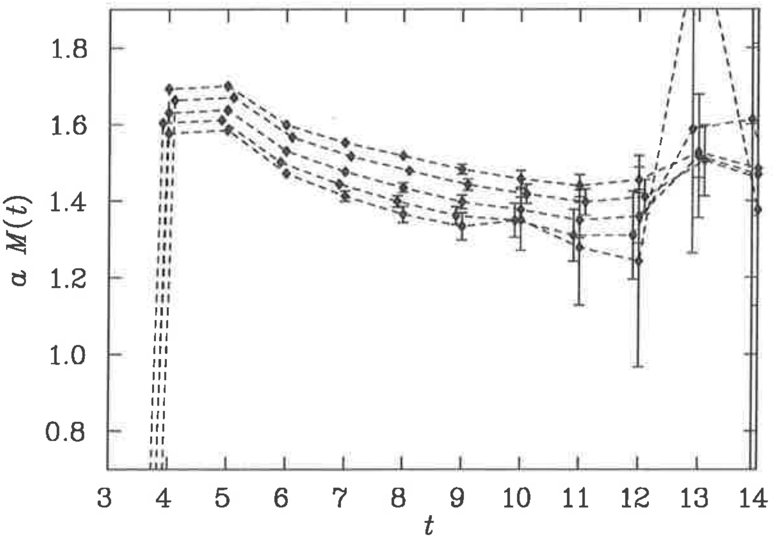

Figure 8.8: As in Fig. 8.7, but for the $\Delta\frac{3}{2}^{-}$ state.

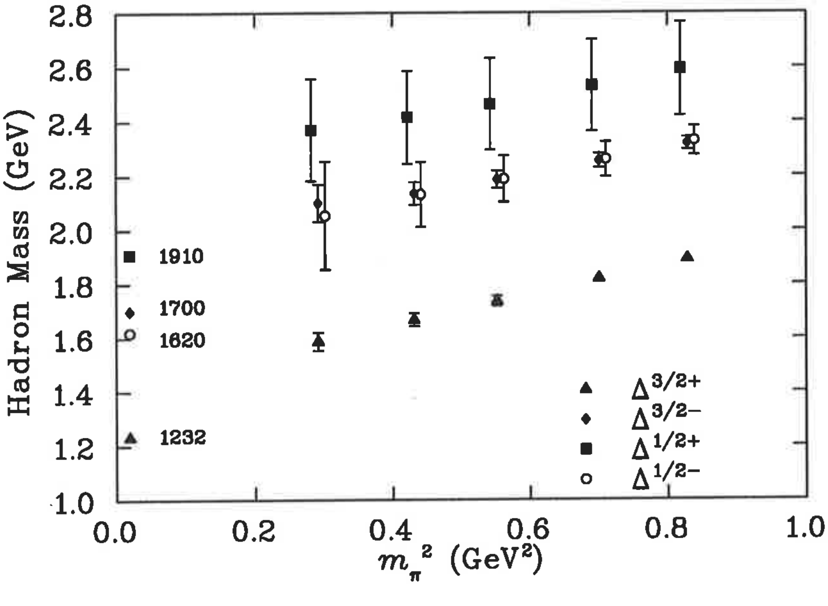

Figure 8.9: Masses of the spin-projected $\Delta\frac{3}{2}^{\pm}$ and $\Delta\frac{1}{2}^{\pm}$ resonances. The empirical values of the masses of the $\Delta^{3/2+}(1232)$, $\Delta\frac{3}{2}^{-}(1700)$, $\Delta\frac{1}{2}^{-}(1620)$ and $\Delta\frac{1}{2}^{+}(1910)$ are shown on the left-hand-side at the physical pion mass.

9

Conclusion

This thesis reports work I have done in conducting numerical simulations of Lattice QCD. The basic concepts of The Standard Model, QCD and Lattice QCD are introduced in Chapters 2 and 3.

In Chapter 4, the static quark potential has been calculated in quenched QCD using Symanzik-improved and unimproved Wilson gluon actions. We have kept the lattice spacing and the physical volume of these lattices equal so that we can meaningfully examine the effects of action improvement in the statice quark potential. The number of gauge field configurations (100 here) is also held fixed for each action. We have explicitly shown that, despite the relatively coarse lattice spacing, the unimproved and computationally less expensive Wilson action does just as well as the improved action in extracting the $q\bar{q}$ potential at large separations. If one wishes to keep non-perturbative physics such as non-trivial topological fluctuations on the lattice, then one needs $a < 0.15$ fm [58], and thus $r/a > 7$. In this case, the unimproved, standard Wilson gauge action is ideal for todays string breaking searches as computational resources can be redirected elsewhere. Another advantage for using single-plaquette based actions is that we recover the extremely useful method for calculating the overlap with the ground state, $C_1(r)$, and thus tuning the smearing parameters.

We also explored the use of unconventional paths in accessing off-axis values of r in the static quark potential. These paths can provide insight into the extent to which the ground state potential dominates the Wilson loop at large Euclidean times. Provided the paths are symmetrized, these new paths provide useful information on the ground state potential and nearby excited potentials. Combined with standard paths and variational techniques, these paths offer additional promise for the search for string breaking in lattice QCD.

Chapter 5 is also focused on the static quark potential (SQP). Here we have calculated the SQP on several lattices with different lattice spacings. We use the SQP to extract lattice spacings using both the string tension, σ, and the Sommer scale, r_0. These results are plotted as a function of β to provide a useful tool for predicting the value of β one should choose in order to acheive the desired lattice spacing using a mean-field improved, plaquette + rectangle gluon action.

In Chapter 6 we examine the hadron mass spectrum using a novel Fat-Link

Irrelevant Clover (FLIC) fermion action, in which only the irrelevant, higher-dimension operators involve smeared links. Fat links provide improved scaling behavior over mean-field improvement and is competitive with nonperturbative-improved [22] clover results [63] on plaquette-action gluon configurations. This shows that FLIC fermions provide a new form of nonperturbative $\mathcal{O}(a)$ improvement. The technique also allows the use of highly improved operators and eliminates the need to tune the coefficients of action improvement terms. The FLIC action provides excellent scaling and reduces the exceptional configuration problem. Quenched simulations at quark masses down to $m_\pi/m_\rho = 0.35$ have been successfully performed on a $20^3 \times 40$ lattice with a lattice spacing of 0.134 fm. Simulations at such light quark masses have already revealed the non-analytic behavior of quenched chiral perturbation theory in decuplet baryon masses. This non-analytic behaviour leads to an enhancement in the mass splittings between decuplet and octet baryons in the quenched approximation, although the ratios of these splittings agree well with both the experimental value in Eq. (2.10) and the quark model prediction in Eq. (2.9).

An enhancement of the $N - \Delta$ mass splitting in the quenched approximation has been predicted previously [80] and this is the first time that a lattice calculation of these baryons has been performed at quark masses light enough to confirm this prediction. We expect to see more evidence of chiral nonanalytic behavior in forthcoming simulations of the electromagnetic form factors of hadrons.

In Chapter 7, the first results for the excited baryon spectrum from lattice QCD using an $\mathcal{O}(a^2)$ improved gauge action and a FLIC quark action are presented. The simulations have been performed on a $16^3 \times 32$ lattice at $\beta = 4.60$, providing a lattice spacing of $a = 0.122(2)$ fm. The analysis is based on a set of 400 configurations in the nucleon sector and 200 configurations for the excited hyperon analysis.

Good agreement is obtained between the FLIC and other improved actions, such as the nonperturbatively improved clover [100,105] and domain wall fermion (DWF) [99] actions, for the nucleon and its chiral partner, with a mass splitting of ~ 400 MeV. Our results for the $N^*(\frac{1}{2}^-)$ improve on those using the D_{234} [98] and Wilson actions. Despite strong chiral symmetry breaking, the results with the Wilson action are still able to resolve the splitting between the chiral partners of the nucleon. Using the two standard nucleon interpolating fields, we also confirm earlier observations [97] of a mass splitting between the two nearby $\frac{1}{2}^-$ states. We find no evidence of overlap with the $\frac{1}{2}^+$ Roper resonance.

In the strange sector, we have investigated the overlap of various Λ interpolating fields with the low lying $\frac{1}{2}^\pm$ states. Once again a clear mass splitting of ~ 400 MeV between the octet Λ and its parity partner is seen, with some evidence of a mass splitting between the two states primarily associated with the octet Λ_1^* and Λ_2^* interpolating fields. The Λ^c interpolator does not make any assumptions about the SU(3) flavor symmetry properties of the Λ. The splitting between the common Λ_1^* and Λ_2^* interpolating fields is significantly reduced. Upon performing a full correlation matrix analysis, the two mass states reveal themselves. We find no evidence of strong overlap with the $\frac{1}{2}^+$ "Roper" excitation, $\Lambda^*(1600)$. The empirical mass suppression of the $\Lambda^*(1405)$ is not evident in these quenched QCD simulations, suggesting an important role for the meson cloud of the $\Lambda^*(1405)$ and/or a need for more exotic interpolating fields.

We have not attempted to extrapolate the lattice results to the physical region of light quarks, since the nonanalytic behavior of N^*'s near the chiral limit is not as well studied as that of the nucleon [80,87]. It is vital that future lattice N^* simulations push closer towards the chiral limit. On a promising note, our FLIC action is able to perform simulations at light quark masses corresponding to $m_\pi/m_\rho = 0.35$. It will be interesting to see if we can successfully obtain a signal for N^*'s at these light quark masses.

Our discussion of quenching effects is limited to a qualitative level until the formulation of quenched chiral perturbation theory for $\frac{1}{2}^-$ baryon resonances is established or dynamical fermion simulations are completed. Experience suggests that dynamical fermion results will be shifted down in mass relative to quenched results, with increased downward curvature near the chiral limit [80]. It will be fascinating to confront this physics with both numerical simulations and chiral nonanalytic approaches.

In order to further explore the origin of the Roper resonances or the $\Lambda^*(1405)$, more exotic interpolating fields involving higher Fock states, or nonlocal operators should be investigated. The present N^* mass analysis will be extended in future to include $N \to N^*$ transition form factors through the calculation of three-point correlation functions.

Finally in Chapter 8, we have presented the first results for the spectrum of spin-$\frac{3}{2}$ baryons in the isospin-$\frac{1}{2}$ and $\frac{3}{2}$ channels, using a FLIC quark action and an $\mathcal{O}(a^2)$-improved gauge action. Clear signals are obtained for both the spin-projected $N\frac{3}{2}^\pm$ and $N\frac{1}{2}^\pm$ states from a spin-$\frac{3}{2}$ interpolating field. In particular, the $\frac{1}{2}^\pm$ states are in good agreement with earlier simulations of the nucleon mass and its parity partner using the standard spin-$\frac{1}{2}$ interpolating field. We find the $N\frac{3}{2}^-$ state to lie at a similar energy level to the $N\frac{1}{2}^-$, consistent with experiment, but with a slightly heavier mass, consistent with valence quark models. We also find a mass difference of ~ 300 MeV between the spin-$\frac{3}{2}$, isospin-$\frac{1}{2}$ parity partners, slightly larger than the experimentally observed difference of 200 MeV.

For isospin-$\frac{3}{2}$ baryons, good agreement is found with earlier calculations for the Δ ground state, and clear mass splittings between the ground state and its parity partner are observed after suitable spin and parity projections. We obtain a signal for the $\Delta\frac{1}{2}^{\pm}$ states and the level ordering is consistent with that observed in the empirical mass spectrum.

It will also be important in future work to consider the excited states in each J^P channel, in particular the lowest "Roper-like" excitation of the $\Delta(1232)$ ground state. Although this will be more challenging, it may reveal further insights about the origin of the inter-quark forces and the nature of the confining potential.

A

Gamma Matrices

In the following, we use the Pauli matrices given by

$$\sigma^1 = \begin{pmatrix} 0 & 1 \\ 1 & 0 \end{pmatrix} \quad \sigma^2 = \begin{pmatrix} 0 & -i \\ i & 0 \end{pmatrix} \quad \sigma^3 = \begin{pmatrix} 1 & 0 \\ 0 & -1 \end{pmatrix} \tag{A.1}$$

A.1 Dirac Representation

In the Dirac, Majorana and Chiral representations the γ matrices satisfy

$$\begin{align} \{\gamma^\mu,\, \gamma^\nu\} &= \gamma^\mu\gamma^\nu + \gamma^\nu\gamma^\mu = 2g^{\mu\nu}\,, \quad \mu,\, \nu = 0,\, 1,\, 2,\, 3 \tag{A.2} \\ \gamma_5 = \gamma^5 &= i\gamma^0\gamma^1\gamma^2\gamma^3 = -\frac{i}{4!}\epsilon_{\mu\nu\rho\sigma}\gamma^\mu\gamma^\nu\gamma^\rho\gamma^\sigma \nonumber \\ \{\gamma_5,\, \gamma^\mu\} &= 0 \tag{A.3} \\ \gamma_5^2 = I \quad , &\quad \gamma_5 = \gamma_5^\dagger, \tag{A.4} \end{align}$$

with commutators

$$\begin{align} \sigma^{\mu\nu} &= \frac{i}{2}[\gamma^\mu,\, \gamma^\nu] \tag{A.5} \\ \gamma^\mu\gamma^\nu &= g^{\mu\nu} - i\sigma^{\mu\nu} \nonumber \\ [\gamma_5,\, \sigma^{\mu\nu}] &= 0 \tag{A.6} \\ \gamma_5\sigma^{\mu\nu} &= \frac{i}{2}\epsilon^{\mu\nu\rho\sigma}\sigma_{\rho\sigma} \nonumber \\ \gamma_5\gamma^0\gamma &= \Sigma \quad \text{where } \Sigma^i \equiv \frac{1}{2}\epsilon_{ijk}\sigma^{jk}, \tag{A.7} \end{align}$$

and hermitian conjugates

$$\begin{align} \gamma^0\gamma^\mu\gamma^0 &= \gamma^{\mu\dagger} \nonumber \\ \gamma^0\gamma_5\gamma^0 &= -\gamma_5^\dagger = -\gamma_5 \tag{A.8} \\ \gamma^0(\gamma_5\gamma^\mu)\gamma^0 &= (\gamma_5\gamma^\mu)^\dagger \nonumber \\ \gamma^0\sigma^{\mu\nu}\gamma^0 &= (\sigma^{\mu\nu})^\dagger. \nonumber \end{align}$$

The charge conjugation matrix has the following properties

$$\begin{aligned} C\gamma_\mu C^{-1} &= -\gamma_\mu^T \\ C\gamma_5 C^{-1} &= \gamma_5^T \\ C\sigma_{\mu\nu}C^{-1} &= -\sigma_{\mu\nu}^T \\ C(\gamma_5\gamma_\mu)C^{-1} &= (\gamma_5\gamma_\mu)^T \end{aligned} \tag{A.9}$$

(A.10)

The gamma matrices in the Dirac representation are given by

$$\begin{aligned} \gamma^0 &= \begin{pmatrix} I & 0 \\ 0 & -I \end{pmatrix} \\ \gamma^i &= \begin{pmatrix} 0 & \sigma^i \\ -\sigma^i & 0 \end{pmatrix} \\ \gamma_5 = \gamma^5 &= \begin{pmatrix} 0 & I \\ I & 0 \end{pmatrix} \\ \gamma^5\gamma^0 &= \begin{pmatrix} 0 & -I \\ I & 0 \end{pmatrix} \\ \gamma^5\gamma^i &= \begin{pmatrix} -\sigma^i & 0 \\ 0 & \sigma^i \end{pmatrix} \\ \gamma^5\gamma^0\gamma^i = \Sigma^i &= \begin{pmatrix} \sigma^i & 0 \\ 0 & \sigma^i \end{pmatrix} \\ \sigma^{0i} &= i\begin{pmatrix} 0 & \sigma^i \\ \sigma^i & 0 \end{pmatrix} \\ \sigma^{ij} = \epsilon_{ijk}\Sigma^k &= \epsilon_{ijk}\begin{pmatrix} \sigma^k & 0 \\ 0 & \sigma^k \end{pmatrix} \\ C = i\gamma^2\gamma^0 &= \begin{pmatrix} 0 & -i\sigma^2 \\ -i\sigma^2 & 0 \end{pmatrix} \end{aligned} \tag{A.11}$$

$$C^T = C^\dagger = -C \qquad CC^\dagger = C^\dagger C = I \qquad C^2 = -I \tag{A.12}$$

A.2 Sakurai Representation

In the Pauli representation given in Appendix B of Sakurai [113], the γ matricies satisfy

$$\{\gamma_\mu, \gamma_\nu\} = 2\delta_{\mu\nu} \tag{A.13}$$

$$\sigma_{\mu\nu} = \frac{1}{2i}[\gamma_\mu, \gamma_\nu] = -i\gamma_\mu\gamma_\nu \tag{A.14}$$

$$\gamma_5 = \gamma_1\gamma_2\gamma_3\gamma_4 = \frac{1}{4!}\epsilon_{\mu\nu\lambda\sigma}\gamma_\mu\gamma_\nu\gamma_\lambda\gamma_\sigma$$

$$\{\gamma_5, \gamma_\mu\} = 0 \tag{A.15}$$

$$\gamma_5^2 = I \quad , \quad \gamma_5 = \gamma_5^\dagger, \tag{A.16}$$

and are given by

$$\begin{aligned}
\gamma_4 &= \begin{pmatrix} I & 0 \\ 0 & -I \end{pmatrix} \\
\gamma_i &= \begin{pmatrix} 0 & -i\sigma_i \\ i\sigma_i & 0 \end{pmatrix} \\
\gamma_5 &= -\begin{pmatrix} 0 & I \\ I & 0 \end{pmatrix} \\
i\gamma_5\gamma_4 &= i\begin{pmatrix} 0 & I \\ -I & 0 \end{pmatrix} \\
i\gamma_5\gamma_i &= \begin{pmatrix} \sigma_k & 0 \\ 0 & -\sigma_k \end{pmatrix} \\
\sigma_{4i} &= \begin{pmatrix} 0 & \sigma_i \\ \sigma_i & 0 \end{pmatrix} \\
\sigma_{ij} = \epsilon_{ijk}\Sigma_k &= \epsilon_{ijk}\begin{pmatrix} \sigma_k & 0 \\ 0 & \sigma_k \end{pmatrix} \\
C = \gamma_2\gamma_0 &= \begin{pmatrix} 0 & -i\sigma_2 \\ -i\sigma_2 & 0 \end{pmatrix}
\end{aligned} \tag{A.17}$$

$$C^T = C^\dagger = -C \qquad CC^\dagger = C^\dagger C = I \qquad C^2 = -I \tag{A.18}$$

A.3 Lattice Discrete Symmetries

The transformation of the quark propagator has the following discrete symmetries under which lattice QCD is invariant,

- Parity, $\mathcal{P}$:
$$S_F(x, y, [U]) \rightarrow \gamma_0 S_F(x^P, y^P, [U^P])\gamma_0 \tag{A.19}$$
- Time Reversal, $\mathcal{T}$:
$$S_F(x, y, [U]) \rightarrow \gamma_0\gamma_5 S_F(x^T, y^T, [U^T])\gamma_5\gamma_0 \tag{A.20}$$
- Charge Conjugation, $\mathcal{C}$:
$$S_F(x, y, [U]) \rightarrow \gamma_0\gamma_2 S_F^T(x, y, [U^C])\gamma_2\gamma_0 \tag{A.21}$$
- H Symmetry, $\mathcal{H}$:
$$S_F(x, y, [U]) \rightarrow \gamma_5 S_F^\dagger(y, x, [U])\gamma_5 \tag{A.22}$$
- $\mathcal{CPH}$:
$$S_F(x, y, [U]) \rightarrow C\gamma_0 S_F^\dagger(x^P, y^P, [U^C])\gamma_0 C^{-1} \tag{A.23}$$

B

Improved Field Strength Tensor

The proceedure outlined here is presented in more detail by Bilson-Thompson *et al.* in Ref. [23]. We start by using the expansion in Eqs. (3.5) and (3.6) for the plaquette which leads to the standard lattice expression for $F_{\mu\nu}$

$$ga^2 F_{\mu\nu} = \frac{-i}{2}\left[W^{1\times1}_{\mu\nu} - W^{(1\times1)\dagger}_{\mu\nu} - \frac{1}{3}\mathrm{Tr}(W^{1\times1}_{\mu\nu} - W^{(1\times1)\dagger}_{\mu\nu})\right], \tag{B.1}$$

where $F_{\mu\nu}$ is made traceless by subtracting 1/3 of the trace from each diagonal element.

We now seek to construct a combination of clover terms which will remove $\mathcal{O}(a^2)$ and $\mathcal{O}(a^4)$ errors relative to the leading term, $a^2 F_{\mu\nu}$. The authors of Ref [23] find an expression for an improved field-strength tensor involving the following combination of clover terms

$$F^{\mathrm{Imp}}_{\mu\nu} = k_1 C^{(1,1)}_{\mu\nu} + k_2 C^{(2,2)}_{\mu\nu} + k_3 C^{(1,2)}_{\mu\nu} + k_4 C^{(1,3)}_{\mu\nu} + k_5 C^{(3,3)}_{\mu\nu} \tag{B.2}$$

where $C^{(m,n)}_{\mu\nu}$ corresponds to the $m \times n$ loops used to construct a clover term which is symmetrised in $m \leftrightarrow n$, and the k_i are the weightings of each loop. Bilson-Thompson *et al.* [23] find the improvement coefficients to be

$$\begin{aligned} k_1 &= 19/9 - 55k_5, \\ k_2 &= 1/36 - 16k_5, \\ k_3 &= 64k_5 - 32/45, \\ k_4 &= 1/15 - 6k_5, \end{aligned} \tag{B.3}$$

where the coefficient of the 3×3 loop, k_5, can be tuned to create one of the following

- 3-loop $\mathcal{O}(a^4)$-improved field-strength tensor – $k_5 = 1/90 \Rightarrow k_3 = k_4 = 0$,
- 4-loop improved field-strength tensor – $k_5 = 0,\ 19/495,$ or $1/576 \Rightarrow k_5 = 0, k_1 = 0, k_2 = 0$, respectively
- 5-loop improved field-strength tensor – $k_5 = 1/180$.

By observing the topological charge on a number of different gauge field configurations, Bilson-Thompson *et al.* find the most integer-like results are obtained from the 5-loop improved topological charge operator. They also find that the 3-loop operator also produces excellent results with the added advantage that it is much less computationally expensive than the 5-loop operator.

C

Correlation Matrix Analysis

In this section we outline the correlation matrix formalism for calculations of masses, coupling strengths and optimal interpolating fields. After demonstrating that the correlation functions are real, we proceed to show how a matrix of such correlation functions may be used to isolate states corresponding to different masses, and also to give information about the coupling of the operators to each of these states.

C.1 The $U + U^*$ method

A lattice QCD correlation function for the operator $\chi_i \overline{\chi}_j$, where χ_i is the i-th interpolating field for a particular baryon, can be written as

$$\mathcal{G}_{ij} \equiv \langle \Omega | T(\chi_i \overline{\chi}_j) | \Omega \rangle = \frac{\int \mathcal{D}U \mathcal{D}\bar{\psi} \mathcal{D}\psi e^{-S[U,\bar{\psi},\psi]} \chi_i \overline{\chi}_j}{\int \mathcal{D}U \mathcal{D}\bar{\psi} \mathcal{D}\psi e^{-S[U,\bar{\psi},\psi]}} \,, \tag{C.1}$$

where spinor indices and spatial coordinates are suppressed for ease of notation. The fermion and gauge actions can be separated such that $S[U, \bar{\psi}, \psi] = S_G[U] + \bar{\psi} M[U] \psi$. Integration over the Grassmann variables $\bar{\psi}$ and ψ then gives

$$\mathcal{G}_{ij} = \frac{\int \mathcal{D}U e^{-S_G[U]} \det(M[U]) H_{ij}[U]}{\int \mathcal{D}U e^{-S_G[U]} \det(M[U])} \,, \tag{C.2}$$

where the term H_{ij} stands for the sum of all full contractions of $\chi_i \overline{\chi}_j$. The pure gauge action S_G and the fermion matrix M satisfy

$$S_G[U] = S_G[U^*] \,, \tag{C.3}$$

and

$$\widetilde{C} M[U^*] \widetilde{C}^{-1} = M^*[U] \,, \tag{C.4}$$

respectively, where $\widetilde{C}$ is $C\gamma_5$.

Using the result of Eq. (C.4), one has

$$\begin{aligned} \det\left(M[U^*]\right) &= \det\left(T M^*[U] T^{-1}\right) \\ &= \det\left(M^*[U]\right) \\ &= \det\left(M[U]\right)^* \end{aligned} \tag{C.5}$$

and since $\det(M[U])$ is real,

$$\det\left(M[U^*]\right) = \det\left(M[U]\right) \tag{C.6}$$

Thus, U and U^* are configurations of equal weight in the measure $\int \mathcal{D}U \det(M[U]) \exp\left(-S_G[U]\right)$, in which case $\mathcal{G}_{ij}$ can be written as

$$\mathcal{G}_{ij} = \frac{1}{2}\left(\frac{\int \mathcal{D}U e^{-S_G[U]} \det(M[U])\left\{H_{ij}[U] + H_{ij}[U^*]\right\}}{\int \mathcal{D}U e^{-S_G[U]} \det(M[U])}\right) . \tag{C.7}$$

Let us define

$$G^{\pm}_{ij} \equiv \mathrm{tr}_{\mathrm{sp}}\{\Gamma_{\pm}\mathcal{G}_{ij}\} , \tag{C.8}$$

where $\mathrm{tr}_{\mathrm{sp}}$ denotes the spinor trace and $\Gamma_{\pm}$ is the parity-projection operator defined in Eq. (7.5). If $\mathrm{tr}_{\mathrm{sp}}\left\{\Gamma H_{ij}[U^*]\right\} = \mathrm{tr}_{\mathrm{sp}}\left\{\Gamma H^*_{ij}[U]\right\}$, then $G^{\pm}_{ij}$ is real. This can be shown by first noting that H_{ij} will be products of γ-matrices, fermion propagators, and link-field operators. In a gamma matrix representation which is Hermitian, such as the Sakurai representation, $\widetilde{C}\gamma_\mu\widetilde{C}^{-1} = \gamma^*_\mu$. Fermion propagators have the form M^{-1} and recalling that since $TM[U^*]T^{-1}{=}M^*[U]$, then we have $TM^{-1}[U^*]T^{-1}{=}(M^{-1}[U])^*$. For link-field operators $O[U]$ contained in H_{ij}, the condition $O[U^*] = O^*[U]$ is equivalent to the requirement that the coefficients of all link-products are real. As long as this requirement is enforced, we can then simply proceed by inserting TT^{-1} inside the trace to show that the (spinor-traced) correlation functions are real. If one chooses the Dirac representation, then $\widetilde{C}\gamma_k\widetilde{C}^{-1} = -\gamma^*_k$ and $\widetilde{C}\gamma_0\widetilde{C}^{-1} = \gamma^*_0$. Therefore, if H_{ij} contains an even number of spatial gamma matricies, $G^{\pm}_{ij}$ is purely real, otherwise $G^{\pm}_{ij}$ is purely imaginary.

In summary, the interpolating fields considered here are constructed using only real coefficients and have no spatial γ-matricies. Therefore, the correlation functions $G^{\pm}_{ij}$ are real. This symmetry is explicitly implemented by including both U and U^* in the ensemble averaging used to construct the lattice correlation functions, providing an improved unbiased estimator which is strictly real. This is easily implemented at the correlation function level by observing

$$M^{-1}(\{U^*_\mu\}) = [C\gamma_5\, M^{-1}(\{U_\mu\})\, (C\gamma_5)^{-1}]^*$$

for quark propagators.

C.2 Recovering masses and coupling coefficients

Let us again consider the momentum-space two-point function (Eq. (3.44)) for $t > 0$,

$$\mathcal{G}_{ij}(t,\vec{p}) = \sum_{\vec{x}} e^{-i\vec{p}\cdot\vec{x}} \langle\Omega|\chi_i(t,\vec{x})\overline{\chi}_j(0,\vec{0})|\Omega\rangle . \tag{C.9}$$

At the hadronic level,

$$\mathcal{G}_{ij}(t,\vec{p}) = \sum_{\vec{x}} e^{-i\vec{p}\cdot\vec{x}} \sum_{\vec{p}',s} \sum_{B} \langle\Omega|\chi_i(t,\vec{x})|B,p',s\rangle\langle B,p',s|\overline{\chi}_j(0,\vec{0})|\Omega\rangle \ ,$$

where the $|B,p',s\rangle$ are a complete set of states with momentum p' and spin s. These states form a basis with the conserved quantum numbers carried by the χ interpolating field such that in this subspace

$$\sum_{\vec{p}'}\sum_{B}\sum_{s} |B,p',s\rangle\langle B,p',s| = I \ . \tag{C.10}$$

We can make use of translational invariance to write

$$\begin{aligned}
\mathcal{G}_{ij}(t,\vec{p}) &= \sum_{\vec{x}} e^{-i\vec{p}\cdot\vec{x}} \sum_{\vec{p}'}\sum_{s}\sum_{B} \left\langle\Omega\left|e^{\hat{H}t}e^{-i\hat{\vec{P}}\cdot\vec{x}}\chi_i(0)e^{i\hat{\vec{P}}\cdot\vec{x}}e^{-\hat{H}t}\right|B,p',s\right\rangle \times \\
&\qquad \left\langle B,p',s\left|\overline{\chi}_j(0)\right|\Omega\right\rangle \\
&= \sum_{s}\sum_{B} e^{-E_B t}\langle\Omega|\chi_i(0)|B,p,s\rangle\langle B,p,s|\overline{\chi}_j(0)|\Omega\rangle \ .
\end{aligned} \tag{C.11}$$

Suppose that there are N such states, $|B_\alpha\rangle$. The parity-projected trace of this object is then

$$G^{\pm}_{ij}(t) = \mathrm{tr}_{\mathrm{sp}}\{\Gamma_{\pm}\mathcal{G}_{ij}\} = \sum_{\alpha=1}^{N} e^{-m_\alpha t}\lambda_i^\alpha\overline{\lambda}_j^\alpha \ , \tag{C.12}$$

where λ_i^α and $\overline{\lambda}_j^\alpha$ are coefficients denoting the couplings of the interpolating fields χ_i and $\overline{\chi}_j$, respectively, to the state $|B_\alpha\rangle$. If we use identical source and sink interpolating fields then it follows from the definition of the coupling strength that $\overline{\lambda}_j^\alpha = (\lambda_j^\alpha)^*$ and from Eq. (C.12) we see that $G^{\pm}_{ij}(t) = [G^{\pm}_{ji}(t)]^*$, i.e., $G^{\pm}$ is a Hermitian matrix. If, in addition, we use only real coefficients in the link products, then $G^{\pm}$ is a real symmetric matrix. For the correlation matrices that we construct we have real link coefficients but we use smeared sources and point sinks and so in our calculations G is a real but non-symmetric matrix. Since $G^{\pm}$ is a real matrix for the infinite number of possible choices of interpolating fields with real coefficients, then we can take λ_i^α and $\overline{\lambda}_j^\alpha$ to be real coefficents here without loss of generality.

Suppose now that we have M creation and annhilation operators where $M < N$. We can then form an $M \times M$ approximation of the full $N \times N$ matrix G. At this point we have two options for extracting masses. The first is the standard method for calculation of effective masses at large t as described in Section 6.4. The second option is to extract the masses through a correlation-matrix procedure [114].

Let us begin by considering the ideal case where we have N interpolating fields with the same quantum numbers, but which give rise to N linearly independent states when acting on the vacuum. In this case we constuct N ideal interpolating source and sink fields which perfectly isolate the N individual baryon states $|B_\alpha\rangle$, i.e.,

$$\overline{\phi}^\alpha = u_i^\alpha \, \overline{\chi}_i \, , \tag{C.13a}$$
$$\phi^\alpha = v_i^{*\alpha} \, \chi_i \, , \tag{C.13b}$$

such that

$$\langle B_\beta | \, \overline{\phi}^\alpha \, |\Omega\rangle = \delta_{\alpha\beta} \, \overline{z}^\alpha \, \overline{u}(\alpha, p, s) \, , \tag{C.14a}$$
$$\langle \Omega | \, \phi^\alpha \, |B_\beta\rangle = \delta_{\alpha\beta} \, z^\alpha \, u(\alpha, p, s) \, , \tag{C.14b}$$

where z^α and $\overline{z}^\alpha$ are the coupling strengths of ϕ^α and $\overline{\phi}^\alpha$ to the state $|B_\alpha\rangle$. The coefficients u_i^α and $v_i^{*\alpha}$ in Eqs. (C.13) may differ when the source and sink have different smearing prescriptions, again indicated by the differentiation between z^α and $\overline{z}^\alpha$. For notational convenience for the remainder of this discussion repeated indices i, j, k are to be understood as being summed over. At $\vec{p} = 0$, it follows that,

$$\begin{aligned} G_{ij}^{\pm}(t) \, u_j^\alpha &= \left(\sum_{\vec{x}} \mathrm{tr}_{\mathrm{sp}} \left\{ \Gamma_\pm \, \langle \Omega | \, \chi_i \overline{\chi}_j \, |\Omega\rangle \right\} \right) u_j^\alpha \\ &= \lambda_i^\alpha \overline{z}^\alpha e^{-m_\alpha t} . \end{aligned} \tag{C.15}$$

The only t-dependence in this expression comes from the exponential term, which leads to the recurrence relationship

$$G_{ij}^{\pm}(t) \, u_j^\alpha = e^{m_\alpha} G_{ik}^{\pm}(t+1) \, u_k^\alpha \, . \tag{C.16}$$

which can be rewritten as

$$[G^{\pm}(t+1)]_{ki}^{-1} G_{ij}^{\pm}(t) \, u_j^\alpha = e^{m_\alpha} \, u_k^\alpha \, . \tag{C.17}$$

This is recognized as an eigenvalue equation for the matrix $[G^{\pm}(t+1)]^{-1} G^{\pm}(t)$ with eigenvalues e^{m_α} and eigenvectors u^α. Hence the natural logarithms of the eigenvalues of $[G^{\pm}(t+1)]^{-1} G^{\pm}(t)$ are the masses of the N baryons in the tower of excited states corresponding to the selected parity and the quantum numbers of the χ fields. The eigenvectors are the coefficients of the χ fields providing the ideal linear combination for that state. Note that since here we use only real coefficients in our link products, then $[G^{\pm}(t+1)]^{-1} G^{\pm}(t)$ is a real matrix and so u^α and v^α will be real eigenvectors. It also then follows that z^α and $\overline{z}^\alpha$ will be real. These coefficients are examined in detail in the following section.

One can also construct the equivalent left-eigenvalue equation to recover the v vectors, providing the optimal linear combination of annihilation interpolators,

$$v_k^{*\alpha} G^{\pm}_{kj}(t) = e^{m_\alpha} v_i^{*\alpha} G^{\pm}_{ij}(t+1) \ . \tag{C.18}$$

Recalling Eq. (C.15), one finds:

$$\begin{aligned} G^{\pm}_{ij}(t)\ u_j^\alpha &= \overline{z}^\alpha \lambda_i^\alpha e^{-m_\alpha t} \ , && \text{(C.19)} \\ v_i^{*\alpha}\ G^{\pm}_{ij}(t) &= z^\alpha \overline{\lambda}_j^\alpha e^{-m_\alpha t} \ , && \text{(C.20)} \\ v_k^{*\alpha}\ G^{\pm}_{kj}(t) G^{\pm}_{il}(t)\ u_l^\alpha &= z^\alpha \overline{z}^\alpha \lambda_i^\alpha \overline{\lambda}_j^\alpha e^{-2m_\alpha t} \ . && \text{(C.21)} \end{aligned}$$

The definitions of Eqs. (C.14) imply

$$v_i^{*\alpha}\ G^{\pm}_{ij}(t)\ u_j^\alpha = z^\alpha \overline{z}^\alpha e^{-m_\alpha t}, \tag{C.22}$$

indicating the eigenvectors may be used to construct a correlation function in which a single state is isolated, and can be analysed using the methods of Section 6.4. We refer to this as the projected correlation function in the following. Combining Eqs. (C.21) and (C.22) leads us to the result,

$$\frac{v_k^{*\alpha}\ G_{kj}(t) G_{il}(t)\ u_l^\alpha}{v_k^{*\alpha} G_{kl}(t) u_l^\alpha} = \lambda_i^\alpha \overline{\lambda}_j^\alpha e^{-m_\alpha t} \ . \tag{C.23}$$

By extracting all N^2 such ratios, we can exactly recover all of the real couplings λ_i^α and $\overline{\lambda}_j^\alpha$ of χ_i and $\overline{\chi}_j$ respectively to the state $|B_\alpha\rangle$. Note that throughout this section no assumptions have been made about the symmetry properties of $G^{\pm}_{ij}$. This is essential due to our use of smeared sources and point sinks.

In practice we will only have a relatively small number, $M < N$, of interpolating fields in any given analysis. These M interpolators should be chosen to have good overlap with the lowest M excited states in the tower and we should attempt to study the ratios in Eq. (C.23) at early to intermediate Euclidean times, where the contribution of the $(N - M)$ higher mass states will be suppressed but where there is still sufficient signal to allow the lowest M states to be seen. This procedure will lead to an estimate for the masses of each of the lowest M states in the tower of excited states. Of these M predicted masses, the highest will in general have the largest systematic error while the lower masses will be most reliably determined. Repeating the analysis with varying M and different combinations of interpolating fields will give an objective measure of the reliability of the extraction of these masses.

In our case of a modest 2×2 correlation matrix ($M = 2$) we take a cautious approach to the selection of the eigenvalue analysis time. As already explained, we perform the eigenvalue analysis at an early to moderate Euclidean time where statistical noise is suppressed and yet contributions from at least the lowest two mass states is still present. One must exercise caution in performing the analysis at too early a time, as more than the desired $M = 2$ states may be contributing to the 2×2 matrix of correlation functions.

We begin by projecting a particular parity, and then investigate the effective mass plots of the elements of the correlation matrix. Using the covariance-matrix based χ^2/N_{DF}, we identify the time slice at which all correlation functions of the correlation matrix are dominated by a single state. In practice, this time slice is determined by the correlator providing the lowest-lying effective mass plot. The eigenvalue analysis is performed at one time slice earlier, thus ensuring the presence of multiple states in the elements of the correlation function matrix, minimising statistical uncertainties, and hopefully providing a clear signal for the analysis. In this approach minimal new information has been added, providing the best opportunity that the 2×2 correlation matrix is indeed dominated by 2 states. The left and right eigenvectors are determined and used to project correlation functions containing a single state from the correlation matrix as indicated in Eq. (C.22). These correlation functions are then subjected to the same covariance-matrix based χ^2/N_{DF} analysis to identify new acceptable fit windows for determining the masses of the resonances.

D

Publications By The Author

- J. B. Zhang, S. O. Bilson-Thompson, F. D. Bonnet, D. B. Leinweber, A. G. Williams and J. M. Zanotti, "Overlap Fermions, Improved Cooling And The Lattice Index Theorem," Nucl. Phys. Proc. Suppl. **109A**, 146 (2002).
- W. Melnitchouk, S. O. Bilson-Thompson, F. D. Bonnet, F. X. Lee, D. B. Leinweber, A. G. Williams, J. M. Zanotti and J. B. Zhang, "Excited baryons in lattice QCD," arXiv:hep-lat/0202022.
- F. D. Bonnet, D. B. Leinweber, A. G. Williams, J. M. Zanotti and J. B. Zhang, "Quark propagator in a covariant gauge," Nucl. Phys. Proc. Suppl. **109**, 158 (2002) [arXiv:hep-lat/0202011].
- W. Melnitchouk, S. O. Bilson-Thompson, F. D. Bonnet, F. X. Lee, D. B. Leinweber, A. G. Williams, J. M. Zanotti and J. B. Zhang, "Baryon resonances from a novel fat-link fermion action," Nucl. Phys. Proc. Suppl. **109**, 96 (2002) [arXiv:hep-lat/0201005].
- J. M. Zanotti *et al.*, "Novel fat-link fermion actions," Nucl. Phys. Proc. Suppl. **109**, 101 (2002) [arXiv:hep-lat/0201004].
- J. B. Zhang, S. O. Bilson-Thompson, F. D. Bonnet, D. B. Leinweber, A. G. Williams and J. M. Zanotti, "Numerical study of lattice index theorem using improved cooling and overlap fermions," Phys. Rev. D **65**, 074510 (2002) [arXiv:hep-lat/0111060].
- J. M. Zanotti *et al.* [CSSM Lattice Collaboration], "Hadron masses from novel fat-link fermion actions," Phys. Rev. D **65**, 074507 (2002) [arXiv:hep-lat/0110216].
- F. X. Lee, D. B. Leinweber, L. Zhou, J. M. Zanotti and S. Choe, "N* masses from an anisotropic lattice QCD action," Nucl. Phys. Proc. Suppl. **106**, 248 (2002) [arXiv:hep-lat/0110164].
- F. D. Bonnet, D. B. Leinweber, A. G. Williams and J. M. Zanotti, "Improved smoothing algorithms for lattice gauge theory," Phys. Rev. D **65**, 114510 (2002) [arXiv:hep-lat/0106023].

- F. D. Bonnet, P. O. Bowman, D. B. Leinweber, A. G. Williams and J. M. Zanotti, "Infinite volume and continuum limits of the Landau-gauge gluon propagator," Phys. Rev. D **64**, 034501 (2001) [arXiv:hep-lat/0101013].

Bibliography

[1] Eugene P. Wigner. On unitary representations of the inhomogeneous lorentz group. *Annals Math.*, 40:149–204, 1939.

[2] Chen-Ning Yang and R. L. Mills. Conservation of isotopic spin and isotopic gauge invariance. *Phys. Rev.*, 96:191–195, 1954.

[3] S. L. Glashow. Partial symmetries of weak interactions. *Nucl. Phys.*, 22:579–588, 1961.

[4] S. Weinberg. A model of leptons. *Phys. Rev. Lett.*, 19:1264–1266, 1967.

[5] A. Salam. in elementary particle theory. ed. N. Svartholm (Almquist and Wiksell, Stockholm, 1968).

[6] M. Gell-Mann and Y. Ne'eman. The eightfold way. (Benjamin, New York, 1964).

[7] Particle Data Group. Review of particle physics. *Eur. Phys. J.*, 15:1–878, 2000.

[8] F. E. Close. An introduction to quarks and partons. (Academic Press, London, 1979), 481p.

[9] I. C. Cloet, D. B. Leinweber, and A. W. Thomas. Simple quark model with chiral phenomenology. *Phys. Rev.*, C65:062201, 2002.

[10] T. Muta. Foundations of quantum chromodynamics. second edition. *World Sci. Lect. Notes Phys.*, 57:1–409, 1998.

[11] K.G. Wilson. New phenomena in subnuclear physics. edited by A. Zichichi (Plenum, New York, 1975), Part A, p. 69.

[12] G. Curci, P. Menotti, and G. Paffuti. Symanzik's improved lagrangian for lattice gauge theory. *Phys. Lett.*, B130:205, 1983.

[13] M. Luscher and P. Weisz. On-shell improved lattice gauge theories. *Commun. Math. Phys.*, 97:59, 1985.

[14] G. Peter Lepage and Paul B. Mackenzie. On the viability of lattice perturbation theory. *Phys. Rev.*, D48:2250–2264, 1993.

[15] Mark G. Alford, W. Dimm, G. P. Lepage, G. Hockney, and P. B. Mackenzie. Lattice qcd on small computers. *Phys. Lett.*, B361:87–94, 1995.

[16] K. Symanzik. Continuum limit and improved action in lattice theories. 1. principles and phi**4 theory. *Nucl. Phys.*, B226:187, 1983.

[17] H. J. Rothe. Lattice gauge theories: An introduction. *World Sci. Lect. Notes Phys.*, 59:1–512, 1997.

[18] Rajan Gupta. Introduction to lattice qcd. 1997.

[19] Herbert W. Hamber and Chi Min Wu. Some predictions for an improved fermion action on the lattice. *Phys. Lett.*, B133:351, 1983.

[20] Frank X. Lee and Derek B. Leinweber. Light hadron spectroscopy on coarse lattices with $\wr(a^2)$ mean field improved actions. *Phys. Rev.*, D59:074504, 1999.

[21] B. Sheikholeslami and R. Wohlert. Improved continuum limit lattice action for qcd with wilson fermions. *Nucl. Phys.*, B259:572, 1985.

[22] Martin Luscher, Stefan Sint, Rainer Sommer, and Peter Weisz. Chiral symmetry and o(a) improvement in lattice qcd. *Nucl. Phys.*, B478:365–400, 1996.

[23] Sundance O. Bilson-Thompson, Derek B. Leinweber, and Anthony G. Williams. Highly-improved lattice field-strength tensor. 2002.

[24] Mark G. Alford, T. R. Klassen, and G. P. Lepage. Improving lattice quark actions. *Nucl. Phys.*, B496:377–407, 1997.

[25] Gyan Bhanot. The metropolis algorithm. *Rept. Prog. Phys.*, 51:429, 1988.

[26] N. Cabibbo and E. Marinari. A new method for updating su(n) matrices in computer simulations of gauge theories. *Phys. Lett.*, B119:387–390, 1982.

[27] J. Kuti. Exotica and the confining flux. *Nucl. Phys. Proc. Suppl.*, 73:72–85, 1999.

[28] S. Aoki et al. The static quark potential in full qcd. *Nucl. Phys. Proc. Suppl.*, 73:216–218, 1999.

[29] M. Talevi. Light hadron spectroscopy with o(a) improved dynamical fermions. *Nucl. Phys. Proc. Suppl.*, 73:219–221, 1999.

[30] G. S. Bali et al. Glueballs and string breaking from full qcd. *Nucl. Phys. Proc. Suppl.*, 63:209–211, 1998.

[31] A. Duncan, E. Eichten, and H. Thacker. String breaking in four dimensional lattice qcd. *Phys. Rev.*, D63:111501, 2001.

[32] P. Pennanen and C. Michael. String breaking in zero-temperature lattice qcd. 2000.

[33] Howard D. Trottier. String breaking by dynamical fermions in lattice qcd: From three to four dimensions. *Phys. Rev.*, D60:034506, 1999.

[34] Howard D. Trottier and Kit Yan Wong. Static potential and local color fields in unquenched three-dimensional lattice qcd. 2002.

[35] Slavo Kratochvila and Philippe de Forcrand. String breaking with wilson loops? 2002.

[36] Grigorios I. Poulis and Howard D. Trottier. 'gluelump' spectrum and adjoint source potential in lattice qcd in three-dimensions. *Phys. Lett.*, B400:358–363, 1997.

[37] Stephan Gusken. Dynamical quark effects in qcd. *Nucl. Phys. Proc. Suppl.*, 63:16–21, 1998.

[38] I. T. Drummond. Strong coupling model for string breaking on the lattice. *Phys. Lett.*, B434:92–98, 1998.

[39] M. Falcioni, M. L. Paciello, G. Parisi, and B. Taglienti. Again on su(3) glueball mass. *Nucl. Phys.*, B251:624–632, 1985.

[40] M. Albanese et al. Glueball masses and string tension in lattice qcd. *Phys. Lett.*, B192:163, 1987.

[41] C. Legeland, B. Beinlich, M. Lutgemeier, A. Peikert, and T. Scheideler. The string tension in su(n) gauge theory from a careful analysis of smearing parameters. *Nucl. Phys. Proc. Suppl.*, 63:260–262, 1998.

[42] Carleton DeTar, Urs Heller, and Pierre Lacock. First signs for string breaking in two-flavor qcd. *Nucl. Phys. Proc. Suppl.*, 83:310–312, 2000.

[43] Claude W. Bernard et al. Zero temperature string breaking in lattice quantum chromodynamics. *Phys. Rev.*, D64:074509, 2001.

[44] F. Knechtli. String breaking and lines of constant physics in the su(2) higgs model. *Nucl. Phys. Proc. Suppl.*, 83:673–675, 2000.

[45] Francesco Knechtli and Rainer Sommer. String breaking in su(2) gauge theory with scalar matter fields. *Phys. Lett.*, B440:345–352, 1998.

[46] E. Laermann, C. DeTar, O. Kaczmarek, and F. Karsch. String breaking in lattice qcd. *Nucl. Phys. Proc. Suppl.*, 73:447–449, 1999.

[47] P. W. Stephenson. Breaking of the adjoint string in 2+1 dimensions. *Nucl. Phys.*, B550:427–448, 1999.

[48] Frederic D. R. Bonnet, Patrick Fitzhenry, Derek B. Leinweber, Mark R. Stanford, and Anthony G. Williams. Calibration of smearing and cooling algorithms in su(3)- color gauge theory. *Phys. Rev.*, D62:094509, 2000.

[49] Colin J. Morningstar and Mike J. Peardon. Efficient glueball simulations on anisotropic lattices. *Phys. Rev.*, D56:4043–4061, 1997.

[50] Konrad Osterwalder and Robert Schrader. Axioms for euclidean green's functions. *Commun. Math. Phys.*, 31:83–112, 1973.

[51] G. Parisi. Symanzik's improvement program. *Nucl. Phys.*, B254:58–70, 1985.

[52] C. R. Allton et al. Gauge invariant smearing and matrix correlators using wilson fermions at beta = 6.2. *Phys. Rev.*, D47:5128–5137, 1993.

[53] Bram Bolder et al. A high precision study of the q anti-q potential from wilson loops in the regime of string breaking. *Phys. Rev.*, D63:074504, 2001.

[54] N. Cabibbo and E. Marinari. A new method for updating su(n) matrices in computer simulations of gauge theories. *Phys. Lett.*, B119:387–390, 1982.

[55] Frederic D. R. Bonnet, Derek B. Leinweber, and Anthony G. Williams. General algorithm for improved lattice actions on parallel computing architectures. *J. Comput. Phys.*, 170:1–17, 2001.

[56] M. Luscher. Symmetry breaking aspects of the roughening transition in gauge theories. *Nucl. Phys.*, B180:317, 1981.

[57] R. G. Edwards, U. M. Heller, and T. R. Klassen. Accurate scale determinations for the wilson gauge action. *Nucl. Phys.*, B517:377–392, 1998.

[58] Frederic D. R. Bonnet, Derek B. Leinweber, Anthony G. Williams, and James M. Zanotti. Improved smoothing algorithms for lattice gauge theory. 2001.

[59] C. Michael. The running coupling from lattice gauge theory. *Phys. Lett.*, B283:103–106, 1992.

[60] R. Sommer. A new way to set the energy scale in lattice gauge theories and its applications to the static force and alpha-s in su(2) yang-mills theory. *Nucl. Phys.*, B411:839–854, 1994.

[61] Claude W. Bernard et al. The static quark potential in three flavor qcd. *Phys. Rev.*, D62:034503, 2000.

[62] Hikaru Kawai, Ryuichi Nakayama, and Koichi Seo. Comparison of the lattice lambda parameter with the continuum lambda parameter in massless qcd. *Nucl. Phys.*, B189:40, 1981.

[63] R. G. Edwards, Urs M. Heller, and T. R. Klassen. The effectiveness of non-perturbative o(a) improvement in lattice qcd. *Phys. Rev. Lett.*, 80:3448–3451, 1998.

[64] T. DeGrand. Simple observables from fat link fermion actions. *Phys. Rev.*, D60:094501, 1999.

[65] W. Bardeen, A. Duncan, E. Eichten, G. Hockney, and H. Thacker. Light quarks, zero modes, and exceptional configurations. *Phys. Rev.*, D57:1633–1641, 1998.

[66] M. C. Chu, J. M. Grandy, S. Huang, and J. W. Negele. Evidence for the role of instantons in hadron structure from lattice qcd. *Phys. Rev.*, D49:6039–6050, 1994.

[67] Thomas DeGrand, Anna Hasenfratz, and Tamas G. Kovacs. Optimizing the chiral properties of lattice fermion actions. 1998.

[68] Mark Stephenson, Carleton DeTar, Thomas DeGrand, and Anna Hasenfratz. Scaling and eigenmode tests of the improved fat clover action. *Phys. Rev.*, D63:034501, 2001.

[69] Claude W. Bernard and T. DeGrand. Perturbation theory for fat-link fermion actions. *Nucl. Phys. Proc. Suppl.*, 83:845–847, 2000.

[70] C. Bernard et al. Lattice calculation of heavy-light decay constants with two flavors of dynamical quarks. 2002.

[71] Herbert Neuberger. Bounds on the wilson dirac operator. *Phys. Rev.*, D61:085015, 2000.

[72] James M. Zanotti et al. Hadron masses from novel fat-link fermion actions. *Phys. Rev.*, D65:074507, 2002.

[73] J. M. Zanotti et al. Novel fat-link fermion actions. *Nucl. Phys. Proc. Suppl.*, 109:101–105, 2002.

[74] J. M. Zanotti et al. Light quark simulations and exceptional configurations with flic fermions. in preparation.

[75] Philippe de Forcrand, Margarita Garcia Perez, and Ion-Olimpiu Stamatescu. Topology of the su(2) vacuum: A lattice study using improved cooling. *Nucl. Phys.*, B499:409–449, 1997.

[76] S. Gusken. A study of smearing techniques for hadron correlation functions. *Nucl. Phys. Proc. Suppl.*, 17:361–364, 1990.

[77] A. Frommer, V. Hannemann, B. Nockel, T. Lippert, and K. Schilling. Accelerating wilson fermion matrix inversions by means of the stabilized biconjugate gradient algorithm. *Int. J. Mod. Phys.*, C5:1073–1088, 1994.

[78] Waseem Kamleh, David H. Adams, Derek B. Leinweber, and Anthony G. Williams. Accelerated overlap fermions. *Phys. Rev.*, D66:014501, 2002.

[79] Michele Della Morte, Roberto Frezzotti, and Jochen Heitger. A lattice approach to qcd in the chiral regime. 2001.

[80] R. D. Young, D. B. Leinweber, A. W. Thomas, and S. V. Wright. Chiral analysis of quenched baryon masses. 2002.

[81] Simon Capstick and W. Roberts. Quark models of baryon masses and decays. 2000.

[82] Nathan Isgur and Gabriel Karl. Hyperfine interactions in negative parity baryons. *Phys. Lett.*, B72:109, 1977.

[83] P. A. M. Guichon. A nonstatic bag model for the roper resonances. *Phys. Lett.*, B164:361, 1985.

[84] O. Krehl, C. Hanhart, S. Krewald, and J. Speth. What is the structure of the roper resonance? *Phys. Rev.*, C62:025207, 2000.

[85] Zhen-ping Li, Volker Burkert, and Zhu-jun Li. Electroproduction of the roper resonance as a hybrid state. *Phys. Rev.*, D46:70–74, 1992.

[86] R. H. Dalitz and J. McGinley. Theory of low-energy kaon - nucleon scattering. Low and Intermediate Energy Kaon-Nucleon Physics, ed. E. Ferarri and G. Violini (Reidel, Boston, 1980), p.381.

[87] Derek B. Leinweber, Anthony W. Thomas, Kazuo Tsushima, and Stewart V. Wright. Baryon masses from lattice qcd: Beyond the perturbative chiral regime. *Phys. Rev.*, D61:074502, 2000.

[88] L. Ya. Glozman and D. O. Riska. The spectrum of the nucleons and the strange hyperons and chiral dynamics. *Phys. Rept.*, 268:263–303, 1996.

[89] Nathan Isgur. Critique of a pion exchange model for interquark forces. *Phys. Rev.*, D62:054026, 2000.

[90] A. W. Thomas and G. Krein. Chiral corrections in hadron spectroscopy. *Phys. Lett.*, B456:5–8, 1999.

[91] Simon Capstick and Nathan Isgur. Baryons in a relativized quark model with chromodynamics. *Phys. Rev.*, D34:2809, 1986.

[92] C. L. Schat, J. L. Goity, and N. N. Scoccola. Masses of the 70- baryons in large n(c) qcd. *Phys. Rev. Lett.*, 88:102002, 2002.

[93] Derek B. Leinweber. Qcd sum rule analysis of spin orbit splitting in baryons. *Ann. Phys.*, 198:203, 1990.

[94] Derek B. Leinweber. Do quarks really form diquark clusters in the nucleon? *Phys. Rev.*, D47:5096–5103, 1993.

[95] Derek B. Leinweber. Nucleon properties from unconventional interpolating fields. *Phys. Rev.*, D51:6383–6393, 1995.

[96] Thomas A. DeGrand and Matthew W. Hecht. More about orbitally excited hadrons from lattice qcd. *Phys. Rev.*, D46:3937–3944, 1992.

[97] Frank X. Lee and Derek B. Leinweber. Negative-parity baryon spectroscopy. *Nucl. Phys. Proc. Suppl.*, 73:258–260, 1999.

[98] Frank X. Lee. N* mass spectrum from an anisotropic action. *Nucl. Phys. Proc. Suppl.*, 94:251–254, 2001.

[99] Shoichi Sasaki, Tom Blum, and Shigemi Ohta. A lattice study of the nucleon excited states with domain wall fermions. *Phys. Rev.*, D65:074503, 2002.

[100] D. G. Richards et al. Excited nucleon spectrum using a non-perturbatively improved clover fermion action. *Nucl. Phys. Proc. Suppl.*, 109:89–95, 2002.

[101] M. Gockeler et al. Negative-parity baryon masses using an o(a)-improved fermion action. *Phys. Lett.*, B532:63–70, 2002.

[102] Derek B. Leinweber, R. M. Woloshyn, and Terrence Draper. Electromagnetic structure of octet baryons. *Phys. Rev.*, D43:1659–1678, 1991.

[103] K. C. Bowler et al. Hadron mass calculations with susskind and wilson fermions in the fundamental adjoint plane. *Nucl. Phys.*, B240:213, 1984.

[104] James N. Labrenz and Stephen R. Sharpe. Quenched chiral perturbation theory for baryons. *Phys. Rev.*, D54:4595–4608, 1996.

[105] D. G. Richards. N* spectrum using an o(a)-improved fermion action. *Nucl. Phys. Proc. Suppl.*, 94:269–272, 2001.

[106] W. Melnitchouk et al. Excited baryons in lattice qcd. 2002.

[107] D. B. Leinweber, A. W. Thomas, K. Tsushima, and S. V. Wright. Chiral behaviour of the rho meson in lattice qcd. *Phys. Rev.*, D64:094502, 2001.

[108] V. D. Burkert. Electromagnetic excitation of baryon resonances and the clas n* program. *Few Body Syst. Suppl.*, 11:1–9, 1999.

[109] Derek B. Leinweber, Terrence Draper, and R. M. Woloshyn. Decuplet baryon structure from lattice qcd. *Phys. Rev.*, D46:3067–3085, 1992.

[110] F. X. Lee, D. B. Leinweber, L. Zhou, James M. Zanotti, and S. Choe. N* masses from an anisotropic lattice qcd action. *Nucl. Phys. Proc. Suppl.*, 106:248–250, 2002.

[111] Y. Chung, H. G. Dosch, M. Kremer, and D. Schall. Baryon sum rules and chiral symmetry breaking. *Nucl. Phys.*, B197:55, 1982.

[112] M. Benmerrouche, R. M. Davidson, and N. C. Mukhopadhyay. Problems of describing spin 3/2 baryon resonances in the effective lagrangian theory. *Phys. Rev.*, C39:2339–2348, 1989.

[113] J.J. Sakurai. Advanced quantum mechanics. (Addison-Wesley, Redwood City, CA, 1982).

[114] Craig McNeile and Chris Michael. Mixing of scalar glueballs and flavour-singlet scalar mesons. *Phys. Rev.*, D63:114503, 2001.